

UNCLASSIFIED

AD 273 803

*Reproduced
by the*

**ARMED SERVICES TECHNICAL INFORMATION AGENCY
ARLINGTON HALL STATION
ARLINGTON 12, VIRGINIA**



UNCLASSIFIED

NOTICE: When government or other drawings, specifications or other data are used for any purpose other than in connection with a definitely related government procurement operation, the U. S. Government thereby incurs no responsibility, nor any obligation whatsoever; and the fact that the Government may have formulated, furnished, or in any way supplied the said drawings, specifications, or other data is not to be regarded by implication or otherwise as in any manner licensing the holder or any other person or corporation, or conveying any rights or permission to manufacture, use or sell any patented invention that may in any way be related thereto.

RADC-TDR-61-303

CATALOGED BY ASTIA 273803
AS AD NO. 273 803

School of Electrical Engineering
CORNELL UNIVERSITY
Ithaca, New York

RESEARCH REPORT EE 514

THEORETICAL AND EXPERIMENTAL INVESTIGATION
OF LINEAR BEAM MICROWAVE TUBES

Final Reports, Parts I and II A

1 April 1957 to 31 August 1961

Approved by

G. Conrad Dalman
Lester F. Eastman
Paul R. McIsaac

Published under Contract No. AF30(602)-1696
Rome Air Development Center, Griffiss Air Force Base, N. Y.

School of Electrical Engineering
CORNELL UNIVERSITY
Ithaca, New York

RESEARCH REPORT EE 514

THEORETICAL AND EXPERIMENTAL INVESTIGATION
OF LINEAR-BEAM MICROWAVE TUBES

Final Report, Parts I and IIA

1 April 1957 to 31 August 1961

Approved by

G. Conrad Dalman
Lester F. Eastman
Paul R. McIsaac

Published under Contract No. AF30(602)-1696
Rome Air Development Center, Griffiss Air Force Base, New York

CONTENTS OF FINAL REPORT

	Page
FOREWORD	vii

PART I GENERAL

ABSTRACT	1
INTRODUCTION	4
DISCUSSION	6
A. Beam-Circuit Interaction Studies	6
B. Circuit Studies	17
C. Beam Analyzer Studies	21
D. Cathode Studies	22
CONCLUSIONS	28

PART II BEAM-CIRCUIT INTERACTION

THE VELOCITY DISTRIBUTION IN A VELOCITY-MODULATED
ELECTRON BEAM FROM A SHIELDED PIERCE GUN
A. S. Gilmour, Jr.

NONLINEAR SPACE-CHARGE-WAVE ANALYSIS P. R. McIsaac

ON THE NONLINEAR THEORY OF THE PLANE
KLYSTRON TUBE S. Olving

NONLINEAR SPACE-CHARGE-WAVE THEORY OF THE RADIALLY FINITE ELECTRON BEAM	S. Olving
HARMONIC ANALYSIS OF ELECTRON BEAMS IN KLYSTRONS	W. E. Blair
NONLINEAR ANALYSIS OF KLYSTRON BEAMS	J. E. Romaine
ON THE DYNAMICS OF MAGNETICALLY FOCUSED ELECTRON BEAMS	P. S. Bottorff
THE KINETIC A-C POWER FLOW IN NONHOMOGENEOUS RELATIVISTIC ELECTRON BEAMS	S. Olving
AN INTRODUCTORY RELATIVISTIC STUDY OF THE LLEWELLYN ELECTRONIC GAP	S. Olving
BALLISTIC ANALYSIS OF AN ELECTRON BEAM IN A KLYSTRON	I. Turkekul
LARGE-SIGNAL THEORY OF GRIDDED KLYSTRON GAP	W. M. Sackinger

PART III
CIRCUIT STUDIES

KLYSTRON CAVITIES FOR MINIMUM SPURIOUS OUTPUT POWER	L. A. MacKenzie
NOTE ON THE PRELIMINARY RESULTS OF SPURIOUS OUTPUT POWER MEASUREMENTS	A. Ray Howland, Jr.
PERTURBATION TECHNIQUE	W. E. Blair

PART IV
BEAM ANALYZER

A BEAM TESTER FOR STUDYING THE CHARACTERISTICS
OF D-C AND VELOCITY-MODULATED ELECTRON BEAMS
A. S. Gilmour, Jr.

PART V
CATHODE STUDIES

SOME EFFECTS OF ION BOMBARDMENT ON THE EMITTING
PROPERTIES OF OXIDE-COATED CATHODES H. Hollister

STUDIES OF CONTINUOUSLY OPERATED CATHODES N. Erdibil

LONG-PULSE DIODE STUDY H. Hollister

FOREWORD

1. The broad objective of the research project was to investigate theoretically and experimentally factors which determine the performance of linear beam microwave tubes and to find means of improving performance.

2. The contractor studied such factors as beam-circuit interaction, interaction circuits, beam behavior, c-w and wide-pulse cathode operation, X-ray generation, large-signal analysis, nonlinear space-charge effects, harmonic analysis, klystron gap effects, spurious output generation, mode probing techniques, and other phenomena related to microwave tube operation, the emphasis lying predominantly on the klystron.

3. The information should prove of interest to the microwave tube industry and ultimately benefit all users of beam devices. The results of the work not only provide more insight into large-signal phenomena, the causes of spurious outputs, and cathode limitations, but also indicate design criteria and experimental techniques which will aid the designer to achieve desirable characteristics as well as minimize those which prove objectionable. A possible method of controlling r-f enhanced X-ray generation should be particularly of interest in the design of klystrons for operation in the super power levels. A method of reducing the coupling of higher harmonics from the beam to the circuit could be a major step in reducing mutual interference problems that are proving so detrimental to system performance in dense electromagnetic environments. Interesting observations of cathode behavior under bombardment conditions are noted. These help explain the mechanism of cathode destruction under adverse conditions. Measurement and probing techniques using perturbation methods

are discussed in detail. The report "Nonlinear Space-Charge Wave Theory of the Radially Finite Electron Beam" is an analytical treatment of nonlinear behavior of space-charge waves taking into account the radial boundary conditions. Though the study was limited to nonovertaking conditions of individual beam electrons, the theory sheds further light on low-level phenomena contributing to the generation of higher-order harmonics, output phase-shift variations as a function of drive, and other important factors affecting the behavior of "O" type devices.

4. The contract supported a theoretical and experimental effort. This involved the fabrication of considerable laboratory apparatus associated with the tests; no hardware end items, however, were required to be delivered.

FINAL REPORT

PART I:
GENERAL

ABSTRACT

This final report consists of a collection and discussion of seventeen separate technical reports. They are concerned with basic studies on beam-circuit interaction, interaction circuits, electron beams, and cathode phenomena. The main purpose of these studies was to increase the understanding of such important phenomena as spurious-signal generation, X-rays caused by r-f induced high-speed electrons, cathode limitations, and related phenomena.

Experimental Studies of Beam-Circuit Interaction

Velocity wave measurements were made on an almost perfectly focused Brillouin beam modulated by a cavity gap. A decrease in the maxima of the wave were observed as a function of distance from the modulating gap for small drive signals. This effect became accentuated as the drive level was increased. It was found that the wave measurements were not greatly affected by an increase in the magnetic field above the Brillouin value. but below the Brillouin value, a locking of the plasma wavelength with the beam scallop wavelength was observed.

The interaction tester devised proved to be an excellent source of accurate experimental information on the wave properties of electron beams. It should prove invaluable in large-signal research and in studies of both conventional and unconventional interaction structures.

Theoretical Studies of Beam-Circuit Interaction

In the space-charge wave analysis different simplifying assumptions

were used to obtain solutions of the harmonic component amplitudes of the beam current as a function of drive level, space charge, and drift distance. A small-signal relativistic theory of gaps, important in an understanding of klystron operation, was also developed using this approach. In the ballistic analysis, the large-signal behavior of electrons in the first gap, in the drift region, and in the second gap was analyzed, both in closed form and graphic form. These results are important in providing an insight into large-signal phenomena and in predicting the behavior of beams of low perveance. In particular they indicate possible control of r-f enhanced X-ray generation by means of a velocity filter.

In the interaction experiments that were correlated with the theoretical work, it was shown that a confined-flow space-charge-wave theory, which includes the higher-ranking waves, accurately describes the behavior of a Brillouin focused beam for normalized drive levels up to 30 percent.

Circuit Studies

The circuit studies were concerned with the design of klystron cavities that would minimize the coupling of the higher harmonic currents in the beam to the cavity, so as to reduce the output of spurious harmonics by the tube. These studies give a procedure for designing a re-entrant cavity, which, while having high impedance at the fundamental frequency has low impedances at the higher harmonic frequencies. A symmetrical output section is required, however, but several practical output structures appear to be feasible. Relative measurements of the harmonic output power of an unsymmetrically loaded klystron are described.

Beam Analyzer Studies

A detailed description is given of a versatile precision beam tester constructed for automatic measurements of the properties of a magnetically focused beam. Described also are the results obtained on an almost perfectly focused Brillouin beam of unity perveance and 5 kv. This includes current density contours, scallop amplitude, and wavelength measurements, all as functions of magnetic focusing field and beam voltage. The measured cyclotron and scallop wavelength were found to agree with the theoretical values within two percent and seven percent, respectively. The same equipment could be used for the studies of the beam-circuit interaction and could also be readily adapted to study hollow beams.

Cathode Studies

A basic study was conducted in which an ion gun developed for the study was used to perturb the equilibrium of a cathode by bombarding it with various kinds of high-voltage ions. This is a basic research tool which should be invaluable in cathode research. Bombardment of the cathode with ions of oxygen, carbon monoxide, and argon shed new light on the operation of the cathode at high voltages. It was found that when a cathode was bombarded by oxygen ions, the resistance of the cathodes was affected as rapidly as the emission, indicating that the effect spreads throughout the oxide coating in a very short time.

Studies were also conducted on test diodes operating under conditions simulating high-power klystron operation. An analysis was made of the gases evolved during tube processing and under pulsed and continuous operation. The study included an analysis of the gases evolved during cathode arcing, the main constituent of the gas evolved being carbon monoxide.

INTRODUCTION

The broad objective of this research project was to investigate, both theoretically and experimentally, factors that are important in determining the performance capabilities of high-power linear-beam microwave tubes and to find means of improving their performance. The specific objectives were to include basic studies of beam-circuit interaction, interaction circuits, electron beams, and cathode phenomena. The main purpose of these objectives was to increase the understanding of such important phenomena as spurious signal generation, X-rays caused by r-f induced high-speed electrons, cathode limitations, and related phenomena.

The Final Report consists of a collection and discussion of seventeen separate technical reports, which have been issued as part of the contract requirements since its inception on April 1, 1957. For convenience, all of the reports have been included and form Parts II, III, IV, and V of this Final Report. A brief discussion and summary of the individual reports is included as part of the discussion section to facilitate an over-all view of the project.

An important part of the research program was devoted to studies of spurious output in klystrons. The high-power klystrons developed for radar and communications during the past several years have been operated at higher and higher power levels. The necessity for high efficiencies at such high power requires operation in the nonlinear region, which leads in turn to the presence of rather high harmonic power in the tube output. In order to analyze the problem of the spurious outputs at the harmonic frequencies completely, two separate studies were necessary. One study, both analytical and experimental, was to investigate the impedance of the klystron cavity near the lower

DISCUSSION

A. Beam-Circuit Interaction Studies (Part II)

The basic problem in linear beam microwave tubes is to convert the d-c energy contained in the electron beam into useful r-f energy. This is accomplished by arranging, within the tube, a suitable interaction between the electron beam and an electromagnetic field. Since all of the properties of the tube are determined by this interaction, detailed studies of beam-circuit interaction represent a major portion of the research.

There are many interaction theories, all of which make a large number of assumptions and approximations. Several of these theories have been developed further as part of the research project, and an evaluation is presented that attempts to place these results in their proper perspective. The difficulty in considering the multitude of theories is the proper assessment of the degree to which they can predict actual performance. It probably can be safely stated that, while much has been accomplished in the field, most of the theories developed are essentially only guides in predicting the actual operation of the device.

To help in this assessment an experimental research program was conducted paralleling the theoretical studies. Some preliminary measurements were made of the performance of completed tubes, but it was found that unexplainable effects often obscured the study or that suitable tubes were not available for testing. For this reason a precision demountable interaction analyzer utilizing an almost perfectly focused electron beam was constructed as a research tool. While the results to date have been limited to small-signal studies, they have readily shown that the space-charge-wave approach to medium-power klystrons is an excellent one. The experimental

harmonics. The other study, also both analytical and experimental, was concerned with the nonlinear beam dynamics giving rise to harmonic currents in the electron beam. Thus knowing the currents and the cavity admittance of a cavity at the harmonic frequencies, the harmonic output could be calculated. The results ultimately would be expressed in terms of the load impedance at the harmonic frequencies referred to the cavity gap. The beam dynamics analysis is discussed in Part II and the microwave cavity design is discussed in Part III.

Also included in Part III are some recently obtained measurements of the harmonic output of a high-power klystron and a description of the technique of measuring the klystron gap fields by perturbation of cavity resonance with a metal or dielectric bead.

The work on the ballistic analysis included in Part II was carried out to investigate the velocity spread in modulated beams, which is of considerable importance in r-f-enhanced X-ray generation. Also discussed are some general theories of large-signal dynamics of electron beams. The general theories are of the greatest importance, since they ultimately lead to an understanding of important phenomena, such as, efficiency characteristics, phase properties, bandwidth properties, drive characteristics, etc.

Finally electron beam analysis is discussed in Part IV, and some of the fundamental problems of high-voltage, continuously operated cathodes for high-power linear-beam tubes are discussed in Part V.

results have been so rewarding that these highly precise studies of the large-signal modulated beam are presently being continued. There is considerable promise that the interaction phenomena of a moderately high-power linear beam tube can be well understood. This should lead to an accurate evaluation of many of the proposed interaction theories and possibly will suggest refinements in the theory or new analytical approaches.

Part II contains the complete report on this work by A. S. Gilmour entitled, "The Velocity Distribution in a Velocity-modulated Electron Beam from a Shielded Pierce Gun," (Research Report EE 507). In order to carry out the velocity-modulation studies, a gridless-gap cavity was used to modulate the velocity of the electron beam described in the study of the beam analyzer reported in Part IV. At drive levels as high as $a = .30$ the velocity modulation on the beam produced by this cavity changed the beam diameter less than eight per cent. Consequently, a confined-flow theory including the effects of higher-ranking waves and the manner in which they are launched in the modulation region was developed and is presented. The predictions of this theory are compared with the velocity standing-wave data taken from the modulated electron beam. It is found that the decrease in the maxima of the velocity standing wave as a function of distance is accounted for very well by considering the higher-ranking waves. Moreover, the presence of these waves is the reason for the minima of the velocity standing wave not reaching the d-c beam level. At higher drive levels, the data presented show that the maxima of the velocity standing wave decrease much more rapidly than at low signal levels. It is suggested that at least a second-order theory be carried out to explain this behavior.

Data are also presented showing the behavior of the velocity standing-

wave pattern for magnetic field levels above and below the Brillouin flow value. These data show that the standing-wave pattern for the magnetic field above the Brillouin value is nearly the same as that at Brillouin flow. The major changes are a shortening of the plasma wavelength, which results from the decreased beam diameter, and a decrease in the velocity standing-wave maxima for high drive levels. The data show a considerable amount of interference between the d-c scalloping and the plasma oscillations for magnetic field levels below the Brillouin level. In fact, under certain conditions the plasma oscillation locks onto the d-c scalloping in a manner similar to that in which an oscillator locks onto the resonant frequency of a resonant circuit.

The beam-circuit interaction investigation has included a number of theoretical studies devoted to the nonlinear space-charge-wave analysis of electron beams. Among these is the report by P. McIsaac, "Nonlinear Space-Charge-Wave Analysis," (Research Report EE 513). This report considers a planar klystron (no transverse variations in the drift regions) with the electron motion confined to the axial direction by a strong magnetic field, takes into account the space charge, and is restricted to beam modulations below the electron overtaking point. An arbitrary number of gaps and drift regions are considered. The objective of the study was to analyze the nonlinear behavior of the electron beam in the gap and drift regions as well as the interchange of power in the gap regions with external circuits. By assuming a magnetic wall boundary for the electron beam in the drift region, the planar solutions were obtained for a beam of finite cross section. This allowed attention to be directed to the nonlinear behavior and the power interchange without the complexity of transverse variations, so that the

analysis could be pursued considerably further but with the sacrifice of applicability resulting from using a highly idealized model.

In this report, the general problem of multiple gap and drift regions was formulated with excitation fields having arbitrary time variation at each gap. An exact solution was obtained to this nonlinear problem using a particular set of independent co-ordinates, but unfortunately the solution is not suitable for numerical computation. The main portion of the report considered the approximate solutions for c-w excitation using the z , and t co-ordinates, which are suitable for computation. These solutions were obtained by analyzing a series of particular cases of interest for klystron theory.

The first case was that of an ideal (i. e., infinitesimal) gap followed by a drift region. A first-order solution was obtained which yielded the harmonic component amplitudes of the beam current of all orders as a function of drive level, space charge, and drift distance. The onset of saturation of the fundamental component and the rapid growth of the harmonic amplitudes at the electron overtaking point was revealed. A second-order solution, while not appreciably affecting the harmonic amplitude predicted by the first-order solution, yielded a phase shift and a d-c polarization component that were dependent on the drive.

The second case was a gap of finite length followed by a drift region. The gap transit angle was computed and, to the first order, the amplitudes of the various harmonic components of the electron beam current. The dependence of the harmonic growth on the gap length, as well as the drive level, space charge, and drift distance was examined. For short gaps, the beam loading was computed.

The third case was of two ideal (or short) gaps separated by a drift region, i. e. , an idealized two-cavity klystron. The power interchange and especially the power delivered to the output load was studied as a function of the parameters. The onset of saturation was noted, and some of the factors influencing the power output were examined.

S. Olving also considered the nonlinear space-charge-wave analysis of planar klystrons in the report "On the Nonlinear Theory of the Plane Klystron Tube," (Research Report EE 500) in Part II. This study, pursued independently of the study just described, uses as a model a confined-flow electron beam of infinite cross section, which crosses an ideal gap followed by a drift region. An exact solution was obtained for arbitrary (in time) velocity modulation of the beam at the ideal gap, and then an approximate solution, which is more useful for numerical computation. For sine-wave modulation, the results obtained are essentially similar to those obtained in the report by McIsaac. In addition, Olving considered d-c modulation of the electron beam, comparing the infinite beam with the finite beam in this regard, and also examined saw-tooth modulation of the beam. Saw-tooth modulation might make for enhanced efficiency, and an estimate of the improvement in the efficiency that might be attained was made.

The nonlinear space-charge-wave theory of an electron beam of finite cross section passing through a conducting drift tube is presented in Olving's "Nonlinear Space Charge Wave Theory of the Radially Finite Electron Beam," (Research Report EE 497). The electron beam was assumed to be confined by a strong axial magnetic field and its velocity modulated by an ideal input gap. Attention was restricted, as before, to modulation levels below the electron overtaking point. After obtaining the exact nonlinear partial differ-

ential equation for sinusoidal modulation, a method of successive approximations was used to obtain a solution. The first-order solution was the usual linear space-charge-wave solution and was used to obtain a second-order, nonlinear space-charge-wave solution, which yielded the fundamental and second-harmonic components. The resulting nonlinear space-charge waves revealed a nonperiodic variation with distance along the drift tube, and, in general, the second harmonic contained terms which grew linearly with distance. In addition, by considering the thin beam case, the particular space-charge reduction factors employed by Paschke (and apparently chosen somewhat arbitrarily) for his thin beam analysis are shown to be, indeed, correct.

Earlier studies on the nonlinear space-charge-wave theory for electron beams having finite cross section and confined flow were made by W. E. Blair and J. Romaine. In the report by Blair, "Harmonic Analysis of Electron Beams in Klystrons," (Research Report EE 458), accurate predictions of velocity modulation for gridded gaps under large-signal conditions are made. These predictions include the effects of the signal on the transit times of the electrons.

Using the thin-gap approximation of this velocity modulation theory, the report then derived, following the successive approximation approach of Paschke, the nonlinear space-charge-wave solutions in a confined-flow drift space. The fundamental and two harmonic current components were each computed as functions of drive and distance. The variations of these components with distance depended on several waves of different plasma wavelengths, and were in general very irregular. In the limit of a large beam diameter, compared with a space-charge wavelength, the variations were regular and were

like standing waves of constant peak amplitude in distance and having the same period as the fundamental plasma standing waves. In the limit of a thin beam compared with a space-charge wavelength, the variations were also more regular and were like standing waves whose peak amplitudes varied as the distance to the $(n-1)$ power for the n^{th} harmonic and that had a period that was $1/n$ as large as that of the fundamental-frequency plasma wavelength. At intermediate thicknesses of beams, the results showed a general trend of rising peak amplitudes for the first fundamental plasma wavelength, with higher harmonics rising faster, but being smaller in amplitude, and having relatively irregular periods.

In addition to this work on nonlinear space-charge waves having a simple plasma-frequency reduction factor, work was done using the different space-charge reduction factors for the fast and slow space-charge waves. This work showed that the difference in assumptions gave small effects which should be of only minor significance in actual nonlinear interactions.

In the report by J. Romaine, "Nonlinear Analysis of Klystron Beams," (Research Report EE 426), computer programs for first-cavity, small-signal interactions and for intermediate or final cavities and drift spaces at large signals in a confined-beam klystron were set up. Next an analytical approach was used. Even though this successive approximation approach to the solution of nonlinear space-charge waves was started as an aid to direction in machine computations, it proved to be valuable enough in its own right to be used to predict klystron behavior directly. In this approach a simple gap-coupling coefficient was used to give an effective modulation voltage and the resulting small-gap approximation to the velocity modulation harmonic series. Then with the approximation of the fundamental frequency being much larger than

the reduced plasma frequency, a first-order set of expressions for the fundamental frequency and harmonic currents was derived. The modulation approximations would make the results poor for large gaps and large drives. The frequency approximation would make the drift-tube results poor for large distances. The frequency approximation would also be poor for locating the minima of harmonic currents and for evaluating their peak values.

These limited results make it possible to predict the harmonic currents, in the first 90° plasma drift angle, up to $(\omega/\omega_{q1})(eC_1/2) = \gamma = .73$, where the Fourier series convergence stops. At this drive the fundamental was 60 percent of its ultimate saturation value. The ω_{q1} was the reduced-plasma frequency, e was the normalized modulation voltage, and C_1 was the gap-coupling coefficient. The results also predict that the fundamental current saturated at $\gamma = 1.63$ at the 90° plasma drift location and, in general, could predict the fundamental current behavior up to $\gamma = 2.8$. There was a peak in fundamental current density at a distance that gradually reduces with drive. It reduces to only 35° for $\gamma = 2.8$. The results agree well with ballistic theory at small drift distances and indications are that the fundamental current can best be computed from ballistic theory at drives larger than $\gamma = 2.8$.

A study of the nonlinear space-charge-wave analysis of electron beams focused by finite axial magnetic fields (and, in particular, using Brillouin focusing) by P. Bottorff is presented in "On the Dynamics of Magnetically Focused Electron Beams," (Research Report EE 505). The aim of this study was to obtain, by a method of successive approximations, the nonlinear solution for a Brillouin beam. A third-order solution was obtained, yielding information on the fundamental, second- and third-harmonic amplitudes of the electron beam current in the drift tube for sinusoidal modulation at a gridless

input gap. The analysis revealed the saturation of the fundamental component of current at high drive, and it was observed that electron overtaking occurred beyond the saturation drive level for this type of focusing. For particular beam parameters, the theory predicts the growth of the second-harmonic component with distance.

In addition to the six reports already described dealing with nonlinear space-charge-wave theory, two other reports concern somewhat related studies. The first, Olving's, "The Kinetic A-C Power Flow in Nonhomogeneous Relativistic Electron Beams," (Research Report EE 499), extends the theory of kinetic power flow in electron beams to beams with velocities in the relativistic range. Chu has shown that for nonrelativistic homogeneous electron beams the kinetic space-charge-wave power flow can be expressed accurately in terms of the linearized space-charge-wave solutions for small-signal analysis. This report extends this type of analysis to nonhomogeneous relativistic electron beams, developing the relevant conservation theorems. This extension is important because of the ever-increasing power-level requirements of microwave tubes and the consequent increase in beam voltage into the relativistic range.

The second related report is Olving's "An Introductory Relativistic Study of the Llewellyn Electronic Gap," (Research Report EE 498). The Llewellyn theory for the analysis of the behavior of electrons in klystron gaps has long been important in understanding klystron operation. Olving's report extends this theory to include relativistic effects in the linear range using the space-charge-wave approach. This study is a basic starting point for future investigations of high-frequency phenomena in diodes, multigrid electron tubes, and klystron gaps, when the electron velocities are in the relativistic range.

Parallel with the studies of space-charge-wave theories, a large-signal

extension of the classical ballistic theory was undertaken. This work is reported in I. Turkekul's, "Ballistic Analysis of an Electron Beam in a Klystron," (Research Report EE 508). Although the simple ballistic theory lacks validity at or after crossover because of space-charge forces and does not apply to electron beams of finite radius because of fringing of the space-charge fields, it has two advantages: (1) It is simple and provides an insight into the physical phenomena, thus serving as a guide for more complicated theories. (2) It is fairly accurate at large-signal levels for low-perveance beams.

The current tendency to demand higher power levels from klystrons increases the importance of ballistic theory. In an experiment reported in the literature, it has been shown that for large signals, the electron beam shows ballistic behavior; therefore, at large-signal levels, the debunching effect of the space-charge forces becomes less important. At the same time, in finite beams, the space-charge forces act to enhance bunching at large signals, by debunching inner and outer electrons differently.

The purpose of this ballistic study was to analyze the modulated electron beam, both in the first gap and in the drift space, and to obtain functional relationships among the various parameters in analytic form. To simplify the analysis, the following assumptions were made: (1) beam of infinite cross section, (2) negligible space charge, (3) gridded finite gaps, and, (4) non-relativistic velocities.

This study showed that the exact graphic analysis revealed the physical relationships occurring in the first gap and in the drift space, but the method is tedious and time-consuming and does not give the functional relationships among various parameters. The method of analytical approximation to the

graphic method, on the other hand, was demonstrated to be very satisfactory; the second-order solution method approximated the large-signal cases well and also gave analytical formulas which revealed information about the harmonics. The results showed that the large-signal velocity modulation was a nonlinear function of the depth of modulation and was inversely proportional to the d-c gap transit angle. The difference between the minimum velocity and the d-c velocity was greater than the corresponding difference between the maximum velocity and the d-c velocity; the current modulation, on the other hand, was also proportional to the depth of modulation, but first it increased and then decreased as the d-c gap transit angle increased continuously. Both velocity and current expressions contained harmonics at the exit of the first gap, but this effect was more pronounced in the current expression.

The maximum value of the fundamental current found was greater than the value of 1.16 predicted by Webster. The point in the drift space at which the maximum value of a harmonic occurred was inversely proportional to the depth of modulation. These results have been shown, at least qualitatively, in the work of others. An additional phase angle β_n was introduced into the current by the two independent components of each harmonic. The velocity became more nonlinear through drift action; the extreme values did not change considerably. This report dealt with the simplest case. Investigation of the second gap and inclusion of the effects of space-charge and gridless gaps for finite beams would be a logical continuation of this study.

The next important step is to obtain further precision measurements of the properties of modulated beams, particularly at large drive levels. These studies should suggest the proper model to assume and therefore indicate the proper direction of a new theoretical analysis. If successful, this

approach could be extended to super power and possibly investigations of crossed-field tubes.

A second ballistic study undertaken to investigate the large-signal behavior of a modulated electron beam in the output gap of a two-cavity klystron, is reported in "Large-Signal Klystron Gap Theory," (Research Report EE 483), by W. Sackinger. He developed the ballistic theory of an electron beam in a gridded gap modulated by a sinusoidal electric field and obtained an exact solution for the velocity and current at the exit plane in terms of the entrance phase. The theory was applied to an output gap with the velocity and current at the entrance plane given by Paschke's results of the nonlinear space-charge-wave analysis for planar klystrons. The velocity and current at the exit plane and the change in average kinetic energy of the electron beam in the output gap were computed for several drive levels. The velocity distribution at the exit plane showed two bunches of relatively high-velocity electrons per cycle. This tends to support the feasibility of a velocity filter to extract energy from the fast electrons and hence reduce X-rays.

B. Circuit Studies (Part III)

Within the past several years, engineers have become increasingly aware of the serious problem presented by the spurious outputs of high-power microwave systems. One worker has shown the severity of this problem as related to interference caused by radar systems in a paper citing experiments in which measurements were made on several radars to determine their power output spectrum. All of the radars showed "very substantial magnitudes" of power radiated at frequencies other than the signal frequency. The radars tested employed both magnetrons and klystrons as the microwave power source.

There are two broad approaches to this problem of spurious-outputs. The first is to suppress the unwanted output by some means external to the high-power microwave tubes, and the second is to improve the basic design of these tubes to prevent the generation of spurious signals. The first method can be used to improve existing tubes while the second is desirable for design of future tubes. This phase of the linear-beam microwave tube program is concerned with the application of the second method to high-power klystrons.

With respect to spurious outputs, there are two general areas of concern in a high-power klystron. First, the requirements of reasonable gain, high efficiency, and high output power will certainly result in nonlinearities in the electron beams in the downstream section of a klystron. This in turn implies that harmonics will be present in this beam. These beam harmonics represent a potential source of spurious output power. Second, there is the requirement of coupling the r-f energy in the beam to an external transmission line. The conventional coupling circuit, the "output cavity," has pass bands at higher frequencies as well as at the fundamental. These higher pass bands facilitate the transfer of harmonic power from the beam to the external transmission line.

The present-day technique of klystron design usually gives little attention to higher-order pass bands or resonances of cavity structures. Consequently, the approach here was to investigate the feasibility of defining optimum cavities so as to minimize the transfer of harmonic power from the klystron beam to the surrounding area. Thus, the ultimate goal was to suppress the spurious harmonic outputs of a high-power klystron by controlling the output cavity design over a broad frequency band.

Preliminary experiments measuring the harmonic content of a high-power

klystron helped define the problem of spurious outputs. Two methods of measuring the harmonic variations of the beam were originally considered: the first, making multimode power measurements in the wave guide connected to the output cavity; the second, placing a small sampling loop in the output cavity of the klystron. Considering the preliminary nature of these measurements, the second method was chosen for two reasons: (1) It gives information about all the harmonics present in the output cavity of the tube; therefore, the sampling loop provides a method of determining which harmonics the tube is capable of producing independent of the load placed on it, whereas the first method provides only information about those harmonics which are coupled out of the tube into the wave guide for the specific load presented to the tube. Consequently, the sampling loop provides more complete and basic information about the tube itself than the multimode technique does. (2) The sampling loop could easily be built and placed in the output cavity, whereas the multimode power-measuring apparatus, including the multimode load, would have been very complex and difficult to construct. Some of the results of these measurements are included as a note.

A theoretical analysis of klystron cavity resonant modes, also included in Part III, shows what possibilities there are for the synthesis of a symmetrical cavity to reduce the responses to the lower harmonics of the klystron beam. This cavity is of the doubly re-entrant, gridless-gap type, which is necessary for high-power klystrons. The analysis showed that, in effect, appropriate cavity dimensions could be chosen for a given operation frequency to displace other cavity resonances from harmonic frequencies up to the fourth harmonic. There were, in particular, optimum shapes of cavities which could be scaled in size for frequency. The selection and specification of the optimum shapes and the final scaling for frequency are described in L. MacKenzie's report.

The unsymmetrical klystron cavity, as used in modern high-power klystrons, was not considered in this analysis, because its mode structure is more complex than the symmetrical cavity, with the result that an optimum shape would be far more difficult to determine.

To complete this study of the klystron cavity, an accurate method for determining the interaction fields of the cavity's gridless gap must be used. The perturbation of this field by beads was discussed theoretically in L. MacKenzie's report, "Klystron Cavities for Minimum Spurious Output Power," (Research Report EE 418), and the actual technique used is covered in the study "Perturbation Technique," (Research Report EE 429), by W. E. Blair.

This completes the phase of study on spurious outputs under this contract. However, at present, effort is continuing in this area. In particular, theoretical and experimental work will be directed towards methods for coupling the klystron output cavity symmetrically to the output-cavity transmission line. Such a scheme, together with a symmetrical output cavity, will apply a symmetrical load to the klystron beam. This should make it possible to control, analytically, the higher-order resonances of the output cavity by the methods indicated in the report by MacKenzie (Research Report EE 418). This symmetrical output system would be novel in the design of high-power klystrons, which at present use either heavy coupling loops or large irises to couple the output cavity unsymmetrically to the wave guide. Finally, an actual test on a commercial klystron will be performed by replacing the original output cavity with a newly designed symmetrical output cavity and coupling system to the output wave guide. At this point more refined measurements than those indicated in the note by Howland will be required on the harmonic power output of this klystron. Such measurements will probably be

performed directly in the output wave guide so as to compare the performance of the new cavity with the original.

C. Beam Analyzer Studies (Part IV)

Although many workers have made measurements on velocity-modulated beams, no one has critically examined the state of the beam carefully before it was modulated. A knowledge of the state of the unperturbed beam to be velocity-modulated is important because most theories that describe the r-f behavior of a beam are based on an ideal beam, i. e., one that is laminar, free from scalloping or other variations in the axial direction, with a charge density that is constant in the radial and angular directions. Since one of the purposes of this research program has been to compare the predictions of existing theories to the actual beam behavior, it was necessary to produce a beam that approximated the ideal beam as closely as possible before attempting an experimental r-f beam study.

A. S. Gilmour's, "A Beam Tester for Studying the Characteristics of D-C and Velocity-modulated Electron Beams," (Research Report EE 495), contains the complete report on the beam tester that was constructed to analyze electron beams, as well as the results of d-c measurements that were taken on a magnetically focused electron beam from a shielded Pierce gun. Some of the important features of the tester were: (1) a valve between the electron gun and the drift region, which made it possible to keep the cathode at pressures below 1×10^{-7} mm Hg at all times, including periods when the drift tube was exposed to air and when changes were being made in the beam-scanning mechanism, etc.; (2) an aperture which could be positioned so as to make current measurements at any point in an electron beam; (3) a double vacuum

system that permitted aperture adjustment rods to be moved into and out of the drift-tube region without causing appreciable changes in pressure; and (4) an automatic scanning and recording device, which eliminated the necessity for taking point-by-point measurements in the beam.

The effect of the magnetic field of the filament of the gun, and of other stray magnetic fields, on the beam shape is shown by cross sections taken by an automatic recorder. Plots are given of the cyclotron wavelength, scallop wavelength, and beam diameter as functions of the magnetic focusing field and the beam voltage. The cyclotron wavelength was found to agree with the theoretical value to within two per cent. The experimental scallop wavelengths were about seven per cent below the theoretical values. The reason for this discrepancy was not determined, although the effects of the magnetic field in the gun region and of the space-charge forces caused by positive ions and by reflected electrons were investigated. The equilibrium beam diameter containing 93 per cent of the beam was found to agree with the theoretical values to within three per cent. The 95 per cent diameter was greater than the theoretical value by about six per cent and the 90 per cent diameter was less by about six per cent.

D. Cathode Studies (Part V)

An important limitation on the ultimate power capabilities of present-day high-power microwave tubes is the maximum current that can be drawn from the cathode. Often these tubes are operated under pulsed conditions so that much higher currents can be drawn than by using direct current and the problem of increasing the energy per pulse becomes that of increasing either the peak current or the length of the pulse. The maximum value of this cur-

rent is limited by: (1) the maximum emission of which the cathode is capable, and (2) the sparking phenomenon, both of which depend on the condition of the cathode. In the laboratory, maximum emission currents up to 100 amp/cm² have been obtained, but in practice an emission of 6 amp/cm² is considered very good. For continuously operated tubes approximately 2 amp/cm² seems to be the highest practical cathode current density.

The problem of obtaining higher emission seems to be that of obtaining a well-activated cathode initially and maintaining it by minimizing the poisoning agents present in the tube. This requires improved cathode materials and improved processing of the tube. As part of the linear beam research project, studies of the effects of the gases on cathode performance were conducted, since the presence of gas appears to be the basic factor in determining the safe operating level and the life of the cathode. In an early study, a mass spectrometer examination was made of the gases given off by a high-power diode during cathode breakdown, temperature and high-voltage processing, and sparking under pulsed operation. It was found that during the breakdown of the cathode, the main gases given off were carbon monoxide and carbon dioxide. During the high-voltage processing of the tube, the main gases present were carbon monoxide and atomic hydrogen and a small amount of water vapor and molecular hydrogen. Studies were also made of the types of gases that evolved from the tube during the sparking. These were found to be mostly carbon monoxide with a small amount of molecular hydrogen. The origin of this carbon monoxide was apparently the result of cathode breakdown.

Details of this study are described in the report by H. Hollister, "Long-Pulse Diode Study," (Research Report EE 430), which is included in

Part V. These studies showed that four gases played an important part in the processing of the tube: atomic hydrogen, molecular hydrogen, water vapor, and carbon monoxide. From the fact that two of these gases, atomic hydrogen and water vapor were not given off at all by gas bursts, it was concluded that they must originate at the only other part of the tube that could be affected by processing the beam collector. From the fact that although a great deal of carbon dioxide was given off by cathode breakdown, but not by processing, it is concluded that this gas when adsorbed on the walls was then converted to carbon monoxide before being driven off, possibly by the reaction $\text{CO}_2 + 2\text{H} \rightarrow \text{CO} + \text{H}_2\text{O}$. In addition to this origin, the carbon monoxide observed was probably also being given off by the cathode and anode during processing. It is believed that the molecular hydrogen observed must come from either the cathode or the anode or both sources.

It was found that the pressure rise in the tube during sparking was due almost entirely to carbon monoxide, and its fragmentation products, and a small amount of molecular hydrogen. A tentative conclusion reached was that the areas of high resistance in the cathode that cause sparking are due to some condition with which carbon monoxide is intimately involved. The amount of carbon monoxide given off by each burst varied from a minimum of 0.001 microgram to a maximum of more than 0.1 microgram, depending on the intensity of the gas burst. The fact that the main gas involved in the gas bursts was also the main gas given off by cathode breakdown and thus adsorbed on the walls of the tube points to back poisoning as an important factor.

While studies of this type are of considerable importance, since the operating conditions were almost identical to those found in actual practice, it is difficult to separate out the relative influences of the various gases on the

operating properties of the cathode. For this reason, a fundamental study of cathode behavior was undertaken. The results of this research are discussed in "Some Effects of Ion Bombardment of the Emitting Properties of Oxide-Coated Cathodes," by H. Hollister (Research Report EE 482). It was felt that to study the processes determining the equilibrium in an oxide cathode, it would be best to perturb this equilibrium in a controllable manner and observe the resulting change in the electronic properties of the cathode. Perturbing techniques that have been widely used in the past are admission of gases to the cathode, admission of reducing agents to the cathode from the base metal, and electrolysis of the cathode coating. A little-used technique is the deposition of chemical agents on the cathode surface by means of ion bombardment.

The ion bombardment technique was refined and an apparatus was developed to study the effect of bombardment by various kinds of ions on the emitting properties of oxide-coated cathodes. A description is given of the development of an ion gun capable of delivering an ion current of up to $3 \mu \text{ amp/cm}^2$ on a target maintained at a pressure of $1(10)^{-7}$ mm Hg. and the results of an investigation of the general effects of ion bombardment by oxygen, carbon monoxide, and argon are given. In these studies only a small amount of differential pumping was employed, so that during the oxygen bombardment studies the cathodes were severely poisoned and the emission density was only of the order of 50 ma/cm^2 at 830°C . The results showed that ion bombardment by oxygen further decreased the emission in all cases, oxygen arriving at the surface by ion bombardment being about one to five times as effective in poisoning the cathode as oxygen from the gas phase. The studies with carbon monoxide and argon were carried out with ion bombardment on active cathodes, having emissions of $1-4 \text{ a/cm}^2$ at 830°C , since the gases themselves had little effect on

the emission. It was found that ion bombardment by carbon monoxide increased the emission of oxide cathodes under all conditions. The effects with argon were much smaller than those for the other gases. With all three gases the emission returned to its original level after ion bombardment.

In order to explore the use of ionic deposition as a tool in studying the effect of chemical agents of the gas phase on the emission of oxide-coated cathodes, a detailed study was made of the effects of ion bombardment by oxygen and carbon monoxide as functions of the voltage of the pulse used to measure the emission, ion beam density, ion energy, d-c current through the cathode, and the temperature of the cathode. In the study using oxygen it was found: (1) that the resistance of the cathodes was affected as rapidly as the emission, indicating that the effect spreads throughout the cathode coating in a very short time, (2) that the recovery from ion bombardment poisoning is significantly retarded by drawing d-c current, which is interpreted as direct evidence against the presence of mobile acceptors and indicates that mobile donors play an important part in the recovery; and (3) that the percentage of decrease in emission caused by a given ion current was nearly constant over the temperature range from 600°C to 900°C. In the study with carbon monoxide it was found that the effect of ion bombardment by carbon monoxide can apparently be explained on the basis of creation of donors at the surface of the cathode and that the activation energy of the rate-controlling process at temperatures above 800°C was about 4 ev. It is felt that the results of this study indicate that ion bombardment can be a powerful tool in the study of the oxide cathode and should be exploited further.

Parallel with the more fundamental studies described in Hollister's, "Long-Pulse Diode Study" (Research Report EE 430), studies of a practical

nature were conducted on dispenser type cathodes. The results of these studies are described in Research Report EE 469, "Studies of Continuously Operated Cathodes," by N. Erdibel. In this study the gas evolution in a thorium-tungsten cathode of an L-cathode during processing and operating periods were investigated and the effects of carbon monoxide, carbon dioxide, hydrogen, and oxygen on the emission activity of the cathodes were studied. The temperature-independent components of the work function for these cathodes were found from emission measurements determined by the measurement technique using the shot-noise reduction factor.

CONCLUSIONS

The results of the research program on linear-beam tubes have shown that close linking of basic experimental studies of interaction with theoretical studies are a very fruitful approach to a better understanding of linear beam tube performance.

Experimental Studies of Beam-Circuit Interaction

In a study of the velocity distribution in a velocity-modulated electron beam it is shown that a confined-flow theory that accounts for higher-order space-charge waves accurately describes the wave phenomena on a Brillouin beam in a large drift tube. It is also shown that when the magnetic focusing field is above the Brillouin value, the space-charge waves are very similar to those occurring at the Brillouin focusing field. When the focusing field is below the Brillouin value, there is a considerable amount of interference of the d-c beam scallops on the shape of the space-charge standing-wave pattern. In fact, under certain conditions the plasma oscillation locks onto the radial oscillation (d-c scalloping) of the beam.

Theoretical Studies of Beam-Circuit Interaction

From the various studies of the nonlinear space-charge waves in the beam-circuit interaction investigation, a number of conclusions can be drawn: One general conclusion is that these theoretical analyses have proceeded sufficiently for qualitative estimates (and to some extent, quantitative estimates) to be made of such experimentally observable parameters as the harmonic amplitudes of the current and velocity of the electron beam, power

output, beam loading, and phase delay. It is highly desirable, therefore, that careful experiments aimed at measuring these parameters be performed and be compared with the theoretical predictions so that the relative merits of the analyses may be assessed and further attention directed toward the more promising ones. A number of more specific conclusions can be drawn from the various studies of nonlinear space-charge waves.

From the nonlinear space-charge analysis, one can conclude that an exact solution can be obtained for the multiple-gap, confined-flow, planar klystron, for arbitrary excitation signals below electron overtaking. This solution is not suitable for numerical computations, however, but is valuable as a starting point for obtaining approximate solutions that are useful for numerical computations. For an ideal input gap (i. e. , of infinitesimal gap length) a first-order approximate solution yields a good estimate of the amplitudes of the electron beam current of all orders and shows the onset of saturation effects. The second-order solution for the ideal input gap does not appreciably influence the harmonic amplitudes of the beam current, but does introduce an excitation-dependent phase delay in the drift region as well as a d-c polarization.

For the input gap that is not ideal, the d-c transit angle is relatively unaffected by the drive level. The fundamental component of the current density is a function of the input gap length. The harmonic amplitudes depend even more sensitively on the input gap length, and increasing the gap length decreases their amplitudes. Beam loading, at least for short input gaps, is found to be relatively insensitive to drive level.

The first-order theory for a two-gap klystron with ideal gaps predicts that the power output will vary in the same manner as the electron beam

current; saturation of the fundamental beam-current component causes the power output saturation. In all cases the phase delay is a second-order effect as a function of drive level. Below electron overtaking the output gap (or below electron reflection at a very short gap) the power output should increase as the load conductance is decreased.

A study of the nonlinear theory of the plane klystron tube gives similar results for an ideal input gap followed by a drift region. In addition, it is concluded that the space-charge reduction factor for an infinite klystron beam (with no transverse variations) must be unity for d-c excitation. The reduction factor for a finite, but large, beam with radial variations, however, is zero for d-c excitation. Also, the use of the fundamental plus second-harmonic excitation as a first-order approximation to a saw-tooth r-f input modulation should produce a marked increase in the efficiency of a klystron.

In the second-order solution obtained for the nonlinear space-charge waves on a finite, confined-flow electron beam in a conducting drift tube, it was concluded that in general the second-harmonic component of the beam current has terms that grow with distance along the drift tube and that a rigorous justification is possible for the use of the space-charge reduction factors introduced by Paschke in his nonlinear analysis of the thin klystron beam.

In the third-order solution to the nonlinear space-charge waves on a finite Brillouin beam in a conducting drift tube, saturation of the fundamental component of the electron beam current is predicted before electron overtaking occurs, and amplitudes of the second and third harmonics are apparently lower than those predicted by a confined-flow theory. Under certain conditions, the second-harmonic amplitude grows with distance along the drift tube. It is also concluded that the boundary conditions at the beam edge need more study to improve the validity of the analysis.

A study of the kinetic a-c power flow in nonhomogeneous relativistic electron beams shows that the statements of kinetic power flow and small-signal power conservation theories previously developed for nonrelativistic electron beams can also be extended to relativistic electron beams. Llewellyn's theory of confined-flow electrons between parallel-plane electrodes for the linearized, nonrelativistic case has been extended to the relativistic case by using a space-charge-wave approach. This study can serve as a basis for future studies of relativistic electron inertia effects in high-frequency diodes, multigrad electron devices, and klystron gaps.

Circuit Studies

A symmetrical high-power klystron cavity can be designed to minimize the coupling to the klystron beam harmonics. This is accomplished by adjusting the shape of a cavity to shift the higher resonances from the vicinity of the lower beam harmonics while the fundamental resonance remains fixed. In addition, it is possible to perform this optimization without affecting the coupling of the fundamental from the beam to the cavity. In utilizing this technique, an important problem remains to be solved - a symmetrical coupling system from the output cavity to the external wave guide must be found to retain the symmetry of the cavity.

The technique of suppressing the spurious outputs of a high-power klystron by optimizing the output cavity has an important advantage over a technique that involves an external filter arrangement. The power-handling capability of a filter arrangement which passes the fundamental and attenuates the harmonics tends to be limited, particularly with respect to disposing of the harmonic power. On the other hand, the technique considered here has no

such limit, in principal, because the harmonic power is at most coupled only very weakly into the output transmission line.

The technique of suppressing spurious outputs of a high-power klystron by optimizing the output cavity has the additional advantage that the electrical length between the penultimate and ultimate cavities of modern high-power klystrons is so short that the possibility of feedback through the drift tube is enhanced. The optimization of the output cavity with respect to spurious outputs will tend to eliminate this possible feedback at the beam harmonics. Furthermore, an extension of these same techniques to the penultimate cavity could tend to eliminate this possible feedback over a wide frequency range about the fundamental.

Beam Analyzer Studies

By using a carefully constructed beam analyzer and a properly designed gun, one can produce a magnetically focused electron beam whose behavior is very close to that predicted by theory. This beam, which can be made nearly free from scalloping (less than 2%) and from electrons with large translaminar velocities, closely approximates the ideal beam normally considered to be present when theories describing velocity modulation are formulated.

Cathode Studies

The new ionic deposition technique of controlled perturbation of a cathode from its equilibrium condition appears to be an excellent approach to understanding of the behavior of high-voltage long-pulse operated cathodes. Ion bombardment of an oxide cathode by oxygen decreases the emission. Ion bombardment by carbon monoxide, on the other hand, increases the electron emission, while argon has little effect. In the studies with oxygen, oxygen ions

were one to five times as effective a poisoning agent as oxygen in the gas phase.

The oxygen-ion bombardment studies have shown that at normal cathode temperatures, the bulk properties of the oxide coating change about as rapidly as the surface properties. The results also support the hypothesis that mobile donors play an important role in the equilibrium processes in oxide cathodes.

After the cathode was broken down, atomic hydrogen, molecular hydrogen, water vapor, and carbon monoxide were liberated in the high-voltage processing of the tube. The pressure rise occurring in tubes which sparked was found to be almost entirely carbon monoxide.

Studies of diodes with thorium-tungsten and L-cathodes indicate that high oxygen background pressures lead to poisoning of the cathode while high carbon-monoxide background pressures lead to activation.

FINAL REPORT

PART IIA:

BEAM-CIRCUIT INTERACTION

**THE VELOCITY DISTRIBUTION IN A VELOCITY-MODULATED
ELECTRON BEAM FROM A SHIELDED PIERCE GUN**

A. S. Gilmour, Jr.

School of Electrical Engineering
CORNELL UNIVERSITY
Ithaca, New York

RESEARCH REPORT EE 507

THE VELOCITY DISTRIBUTION IN A VELOCITY-MODULATED
ELECTRON BEAM FROM A SHIELDED PIERCE GUN

A. S. Gilmour, Jr.

LINEAR BEAM MICROWAVE TUBES

Technical Report No. 15

25 August 1961

Published under Contract No. AF30(602)-1696
Rome Air Development Center, Griffiss Air Force Base, New York

ACKNOWLEDGMENTS

The author wishes to express his gratitude to Professor G. C. Dalman for his constant guidance and many helpful suggestions; Professors P. R. McIsaac and L. F. Eastman for their advice on a course of study, and the Rome Air Development Center of the Air Research and Development Command, USAF (RF Transmitter and High-Power Tube Branch) for its support of the investigation.

CONTENTS

	Page
LIST OF SYMBOLS	vii
I. INTRODUCTION	1
II. CONFINED FLOW ANALYSIS	3
A. GENERAL	3
B. FIRST-ORDER THEORY	6
1. Determination of Propagation Constant	7
2. Initial Conditions	20
III. EXPERIMENTAL RESULTS AND THEIR COMPARISON WITH THEORY	29
A. TECHNIQUE FOR MAKING VELOCITY MEASUREMENTS	29
B. BRILLOUIN BEAM RESULTS	34
C. SCALLOPING BEAM RESULTS	43
IV. CONCLUSIONS AND RECOMMENDATIONS	49
APPENDIX: DESCRIPTION OF INPUT CAVITY	51
REFERENCES	55

LIST OF SYMBOLS

(Symbols in Appendices not Included)

Roman

- a** = Ratio of peak value of electric field in modulating cavity drift tube to V_1/d
- A** = Magnetic vector potential
- $A_{n\pm}$** =
$$\frac{H_{1n\pm}}{\left[(T_{n\pm} r_b)^2 + H_{1n\pm}^2 \right] J_0(T_{n\pm} r_b)}$$
- bctnh** = Bessel hyperbolic cotangent
- b_n** = Intercept on F_n axis of tangent to F_n versus γr_b curve
- c** = Speed of light
- d** = Modulating cavity gap separation
- e_{c1n}** = Coefficient of $J_0(T_n r)$ in radial expansion for E_{c1}
- E_c** = Electric field applied by the circuit
- E_{c1}** = Coefficient of the first term (and only term) in the power series in **a** for E_c .
- E_s** = Electric field arising from the beam
- E_{sn}** = Coefficient of the n^{th} term in the power series in **a** for E_s
- E_{s11}** = Component of E_{s1} that varies only with r , the radial co-ordinate

F	=	Plasma reduction factor
F_n	=	Plasma reduction factor for n^{th} rank wave
F'_n	=	$m_n \beta_e r_b + b_n$
H_{1n}	=	$\tau_n r_b \text{ bctnh } \tau_n r_b \left(\frac{r_c}{r_b} - 1 \right)$
I_0, I_1	=	Modified Bessel functions of the first kind
j	=	$\sqrt{-1}$
J_0, J_1	=	Bessel functions of the first kind
k	=	ω/c
K_0, K_1	=	Modified Bessel functions of the second kind
m_n	=	Slope of F_n versus γr_b curve
M	=	Gap-coupling coefficient
$M_{n\pm}$	=	Gap-coupling coefficients for n^{th} rank fast and slow waves
P_{1n}	=	Coefficient of $J_0(T_n r)$ in radial expansion for P_1
\dot{P}_{1n}	=	Coefficient of $J_0(T_n r)$ in radial expansion for \dot{P}_1
\underline{P}	=	Position of the modulated beam relative to the position of the d-c beam
\underline{P}_n	=	Coefficient of the n^{th} term in the power series in a for \underline{P}
$\dot{\underline{P}}$	=	Variational component of the velocity of the beam

- \dot{P}_n = Coefficient of the n^{th} term in the power series in a for \dot{P}
- P_{11} = Component of P_1 that varies only with r , the radial co-ordinate
- \dot{P}_{11} = Component of \dot{P}_1 that varies only with r , the radial co-ordinate
- r = Radial co-ordinate
- r_b = Beam radius
- r_c = Drift tube radius
- t = Time
- T = Radial propagation constant in beam
- T_n = Radial propagation constant for n^{th} rank wave in beam
- \underline{u}_0 = D-c beam velocity
- V = D-c beam voltage
- V_1 = Peak voltage across modulating cavity gap with beam present
- z = Axial co-ordinate

Greek

- α = Ratio of gap voltage with beam present to d-c beam voltage (depth of modulation)
- β_c = Factor used to give rate of variation of E_{c1} with z in

$$E_{c1} = -\frac{aV_1}{2da} (1 - \cos \beta_c z)$$

- $\beta_e = \omega/u_o$
 $\beta_p = \omega_p/u_o$
 $\beta_{q\pm} = \omega_{q\pm}/u_o$
 $\gamma =$ Axial propagation constant
 $\gamma_{n\pm} =$ Axial propagation constants for n^{th} rank fast and slow waves
 $\delta_n = \beta_e (m_n \beta_p r_b)^2 + m_n \beta_p^2 r_b b_n$
 $\epsilon_o =$ Permittivity of free space
 $\eta =$ Electron charge-to-mass ratio
 $\theta_{n\pm} = \frac{\beta_e \pm \beta_{qn\pm}}{\beta_c} 2\pi$
 $\lambda_c =$ Cyclotron wavelength
 $\lambda_p =$ Plasma wavelength
 $\lambda_q =$ Reduced plasma wavelength
 $\lambda_s =$ Scallop wavelength
 $\rho =$ Beam charge density
 $\rho_n =$ Coefficient of the n^{th} term in the power series in a for ρ
 $\rho_o =$ D-c beam charge density
 $\rho_{11} =$ Component of ρ , that varies only with r , the radial co-ordinate

- τ = Radial propagation constant outside beam
 τ_n = Radial propagation constant outside beam for n^{th} rank wave
 ϕ_{1n} = Coefficient of $J_0(T_n r)$ in radial expansion for Φ_{11}
 Φ = Electric scalar potential
 Φ_n = Coefficient of the n^{th} term in the power series in a for ϕ
 Φ_{11} = Component of Φ_1 that varies only with r , the radial co-ordinate
 ω = Frequency of input signal to modulating cavity
 ω_p = Plasma frequency, $\left(\frac{\eta P_0}{\epsilon_0}\right)^{1/2}$
 $\omega_{q\pm}$ = Reduced plasma frequencies for fast and slow waves

ABSTRACT

To carry out the velocity-modulation studies described in this report, a gridless-gap cavity was used to modulate the velocity of the electron beam described in an earlier study. At drive levels as high as $a = .30$ the velocity modulation on the beam produced by this cavity changed the beam diameter less than 8 per cent. Consequently, a confined-flow theory including the effects of higher-ranking waves and the manner in which they are launched in the modulation region was developed and is presented. The predictions of this theory are compared with the velocity standing-wave data taken from the modulated electron beam. It is found that the decrease in the maxima of the velocity standing wave as a function of distance is accounted for very well by the consideration of the higher-ranking waves. Moreover, these waves are the reason for the minima of the velocity standing wave not reaching the d-c beam level. At higher drive levels, the data presented show that the maxima of the velocity standing wave decrease much more rapidly than at low-signal levels. It is suggested that at least a second-order theory be carried out to explain this behavior.

Data are also presented showing the behavior of the velocity standing-wave pattern for magnetic field levels above and below the Brillouin flow value. These data show that the standing-wave pattern for the magnetic field above the Brillouin value is nearly the same as that at Brillouin flow, except for a shortening of the plasma wavelength, which results from the decreased beam diameter, and a decrease in the velocity standing-wave maxima for high drive levels. The data show considerable interference

between the d-c scalloping and the plasma oscillations for magnetic field levels below the Brillouin level. In fact, under certain conditions the plasma oscillation locks onto the d-c scalloping in a manner similar to that in which an oscillator locks onto the resonant frequency of a resonant circuit.

I. INTRODUCTION

In recent years, many experimental and theoretical studies have been made of the current distribution in velocity-modulated electron beams. The major drawback of the experimental investigations^{1, 2, 3} has been that no careful examination was made of the state of the direct-current beam before modulation. A knowledge of the state of the unperturbed beam is important, because most theories that describe the r-f behavior of a beam are based on an ideal beam; i. e., one that is laminar, free from scalloping or other variations in the axial direction, and having a charge density that is constant in the radial and angular direction, and having a charge density that is constant in the radial and angular directions. Since the major purpose of this study was to compare theoretical predictions with the actual beam behavior, it was necessary to produce a beam that approximated the ideal beam as closely as possible. Moreover, it was desirable to produce a beam similar to those used in commercial linear-beam tubes, so that any results obtained would have a direct bearing on the design and operation of commercial tubes. The d-c electron beam and the beam tester that was constructed to analyze the beam were described in Research Report EE 495.

In deciding upon the approach to be used in developing a theory to describe the velocity modulation on a Brillouin beam some preliminary d-c current measurements on the velocity-modulated beam were used as a guide. These measurements showed that, under Brillouin flow conditions (less than 2 per cent scalloping on the beam), very little change in the beam shape resulted from the velocity modulation. It was assumed, therefore, that

confined flow (no transverse motion of the beam present) existed, and a small-signal theory was developed on this basis. The resulting theory is similar to that of Ramo⁷ up to the point where the radial propagation constants in the beam are found. From that point on, an infinite series of pairs of waves traveling just above and below the beam velocity (fast and slow waves) are considered.

After finding the initial amplitudes of the waves by considering the gap-coupling coefficients for fast and slow waves, the shape of the velocity standing wave on the beam is found by adding up the infinite series of fast and slow waves.

Section III A describes the technique that was used to record the velocity data automatically from the velocity-modulated beam in the beam tester. By using this technique, velocity standing-wave data were obtained for a Brillouin beam. These data are presented in Section III B and are compared with the theoretical predictions. The theory and experiment agree reasonably well on the percentage of decrease of the amplitude of the velocity standing wave with distance, and they are in excellent agreement on the magnitudes of the velocity standing-wave minima.

In section III B data showing the effect of scalloping on the beam are presented. An interesting phenomenon in which the reduced plasma oscillation locks onto the d-c beam scalloping is described.

II. CONFINED FLOW ANALYSIS

A. GENERAL

In the following derivation of the velocities of a modulated Brillouin beam in a large drift tube, two important assumptions are made. The first is that the scalloping on the beam caused by the velocity modulation is small enough so that it can be neglected and a confined flow approach used. This assumption was shown to be valid by some preliminary beam-current measurements made with the beam tester, which showed that at drive levels as high as $a = .30$, the ripple on the beam was less than 8 per cent. The gap-coupling coefficient a is the ratio of the peak voltage across the modulating cavity gap V_1 to the d-c beam voltage V . The value of V_1 is of course that existing when the beam is being modulated by the cavity so that the effects of the current induced into the cavity by the beam are being accounted for. The second assumption is that each quantity associated with the beam can be expanded in a power series in a . For example, the position of the modulated beam relative to the position of the d-c beam is written as

$$\underline{P} = \sum_{n=1}^{\infty} \underline{P}_n a^n, \quad (1)$$

where the bars indicate vector quantities.

The reason for making this type of expansion is that it makes it possible to separate the beam nonlinearities arising in the force equation,

$$\frac{d}{dt} (\underline{u}_0 + \dot{\underline{P}}) = -\eta (\underline{E}_s + \underline{E}_c), \quad (2)$$

where \underline{E}_s is the electric field arising from the beam and \underline{E}_c from the

external circuit, and those arising in the continuity equation,

$$\underline{\nabla} \cdot \rho(\underline{u}_0 + \dot{\underline{P}}) = -\frac{\partial \rho}{\partial t} \quad , \quad (3)$$

where ρ is the charge density of the beam. The quantity u_0 is, of course, the d-c beam velocity and $\dot{\underline{P}}$ is the variational component of the beam velocity. In this work, no attempt will be made to separate the different velocities that a beam has at a particular position if overtaking has occurred; therefore the theory is not valid for beams in which some groups of electrons have actually passed others. Also, only the first-order terms (coefficients of a^1) will be derived, although the following treatment shows how these terms may be used to obtain higher-order terms.

From Equation (1) and the Eulerian expansion of the total time derivative, Equation (2) may be written as

$$\frac{\partial \dot{\underline{P}}}{\partial t} + (u_0 + \dot{\underline{P}}) \frac{\partial \dot{\underline{P}}}{\partial z} = -\eta(\underline{E}_s + \underline{E}_c) \quad ,$$

or

$$\sum_{n=1}^{\infty} \frac{\partial \dot{P}_n}{\partial t} a^n + \left(u_0 + \sum_{n=1}^{\infty} \dot{P}_n a^n \right) \sum_{n=1}^{\infty} \frac{\partial \dot{P}_n}{\partial z} a^n = -\eta \left(\sum_{n=1}^{\infty} \underline{E}_{sn} a^n + \underline{aE}_{c1} \right) \quad , \quad (4)$$

where it has been assumed that the velocity of the undisturbed beam, u_0 , is constant throughout the beam. This is true for Brillouin beams (see Appendix B) as well as for the idealized beam whose charge is neutralized by positive ions and which is confined by an infinite magnetic field with all of the flux passing through the cathode. The electric field produced by the circuit surrounding the beam, E_c , is directly pro-

portional to a since the medium (vacuum) in which the beam is traveling is linear.

In Equation (4), the coefficients of like powers of a may be equated and the result is, for $n = 1$,

$$\frac{\partial \dot{P}_1}{\partial t} + u_0 \frac{\partial \dot{P}_1}{\partial z} = -\eta (\underline{E_{s1}} + \underline{E_{c1}}) ; \quad (5)$$

for $n = 2$,

$$\frac{\partial \dot{P}_2}{\partial t} + u_0 \frac{\partial \dot{P}_2}{\partial z} = -\dot{P}_1 \frac{\partial \dot{P}_1}{\partial z} - \eta \underline{E_{s2}} , \quad (6)$$

and so on. It will turn out that the term $\underline{E_{s2}}$ is made up of products of first-order terms so that the second-order velocity term, \dot{P}_2 can be found if the first-order solution is known. In a similar manner, third- and higher-order terms can be found.

By using Equation (1) one can write Equation (3) as

$$\underline{\nabla} \cdot \left(\sum_{n=0}^{\infty} \rho_n a^n \right) \left(\underline{u}_0 + \sum_{n=1}^{\infty} \dot{P}_n a^n \right) = - \sum_{n=1}^{\infty} \frac{\partial \rho_n}{\partial t} a^n . \quad (7)$$

The first-order part of Equation (7) is

$$\underline{\nabla} \cdot (\rho_0 \underline{\dot{P}}_1 + \underline{u}_0 \rho_1) + \frac{\partial \rho_1}{\partial t} = 0 , \quad (8)$$

the second-order part is

$$\underline{\nabla} \cdot (\rho_0 \underline{\dot{P}}_2 + \underline{u}_0 \rho_2) + \frac{\partial \rho_2}{\partial t} = - \underline{\nabla} \cdot (\rho_1 \underline{\dot{P}}_1) , \quad (9)$$

and so forth, and again, the second- and higher-order terms may be found after the first-order terms are obtained.

Besides Equations (2) and (3), Maxwell's equations are needed for the prediction of the velocities on the beam. Although these equations may be written in many ways (in terms of solenoidal and irrotational vectors, in terms of Hertzian vectors, or in terms of potentials) it is most convenient to write them in terms of potentials. When this is done, the electric and magnetic fields are expressed by

$$\underline{E} = -\underline{\nabla}\phi - \frac{\partial \underline{A}}{\partial t} \quad , \quad \underline{B} = \underline{\nabla} \times \underline{A} \quad , \quad (10)$$

where \underline{E} is the electric and \underline{B} the magnetic field vector; ϕ is the electric scalar potential, and \underline{A} is the magnetic vector potential. With Equation (10), Maxwell's equations reduce to the well-known wave equations⁸

$$\nabla^2 \phi - \frac{1}{c^2} \frac{\partial^2 \phi}{\partial t^2} = \frac{\rho}{\epsilon_0} \quad , \quad (11a)$$

and

$$\nabla^2 \underline{A} - \frac{1}{c^2} \frac{\partial^2 \underline{A}}{\partial t^2} = \mu \rho (\underline{u}_0 + \dot{\underline{P}}) \quad , \quad (11b)$$

where it is implied that

$$\underline{\nabla} \cdot \underline{A} = -\frac{1}{c} \frac{\partial \phi}{\partial t} \quad . \quad (12)$$

A. FIRST-ORDER THEORY

An ideal approach to the problem of finding an expression for the velocity of the electron beam would be to solve Maxwell's equations and

the equations of motion for the beam, in the region where it is modulated by the fields of the cavity first. After this is done, these same equations would be solved in the drift tube region, where no circuit field is applied, and the resulting solutions would be matched to the solutions in the gap region to obtain initial conditions. The approach that is used here differs from the above in that solutions to Maxwell's equations and the equations of motion are obtained in the drift-tube region first. The propagation constants determined are assumed to be the same as the ones existing in the gap-modulation region, so they are used to help obtain an approximate solution in this region. The final step is to match the solutions in the gap-modulation region to those in the drift tube region at the exit from the gap. Throughout the theoretical work, it is assumed that the drift tube is small enough so that the normal wave-guide modes are cut off.

In the first-order theory, which follows, the work of Ramo⁷ is followed closely because it is concise, and because, for nonrelativistic beams, is exact for the first-order solution. Since this is a confined-flow theory, it is necessary to consider only waves propagating in the z direction with axial symmetry.

1. Determination of Propagation Constant

In the drift-tube region, where the applied circuit field E_c is zero, all quantities vary as $e^{j(\omega t - \gamma z)}$ and may therefore be written as,

$$\begin{aligned}
 P_1 &= P_{11} e^{j(\omega t - \gamma z)} , \\
 \dot{P}_1 &= \dot{P}_{11} e^{j(\omega t - \gamma z)} , \\
 \rho_1 &= \rho_{11} e^{j(\omega t - \gamma z)} , \\
 \Phi_1 &= \Phi_{11} e^{j(\omega t - \gamma z)} ,
 \end{aligned}
 \tag{13}$$

where P_{11} , \dot{P}_{11} , ρ_{11} , and Φ_{11} are functions only of r , the radial position. With cylindrical co-ordinates, the equation for the electric scalar potential, Equation (11a), becomes

$$\frac{\partial^2 \Phi_{11}}{\partial r^2} + \frac{1}{r} \frac{\partial \Phi_{11}}{\partial r} - (\gamma^2 - k^2) \Phi_{11} = \frac{P_{11}}{\epsilon_0} \quad , \quad (14)$$

where $k^2 = \omega^2/c^2$. The propagation constant γ may be found if ρ_{11} can be expressed in terms of Φ_{11} . From Equation (8), the continuity equation, the following relation between ρ_{11} and \dot{P}_{11} is easily obtained:

$$\rho_{11} = \frac{1}{u_0} \frac{\gamma \rho_0}{\beta_e - \gamma} \dot{P}_{11} \quad , \quad (15)$$

where $\beta_e = \frac{\omega}{u_0}$. From Equation (5), the force equation, it is found that the electric field caused by the beam is

$$E_{s11} = -j \frac{u_0}{\eta} (\beta_e - \gamma) \dot{P}_{11} \quad . \quad (16)$$

By combining Equations (10) and (12), however, one finds that

$$E_{s11} = j \left(\gamma - \frac{k^2}{\gamma} \right) \Phi_{11} \quad ; \quad (17)$$

so that, with a little manipulation, Equation (15) may be written as

$$\rho_{11} = -\epsilon_0 \beta_p^2 \frac{\gamma^2 - k^2}{(\beta_e - \gamma)^2} \Phi_{11} \quad , \quad (18)$$

where

$$\beta_p^2 = \frac{\omega_p^2}{u_0^2} = \frac{\eta \rho_0}{\epsilon_0 u_0^2} \quad ,$$

and ω_p is the plasma frequency. Combining Equations (14) and (18) gives the following equation for the electric scalar potential:

$$\frac{\partial^2 \Phi_{11}}{\partial r^2} + \frac{1}{r} \frac{\partial \Phi_{11}}{\partial r} + \left[\frac{\beta_p^2}{(\beta_e - \gamma)^2} - 1 \right] (\gamma^2 - k^2) \Phi_{11} = 0 \quad (19)$$

The solution to this equation is of the form,

$$\Phi_{11} = B J_0(Tr) \quad r \leq r_b \quad (20)$$

where r_b is the beam radius, B is an arbitrary constant, and

$$T^2 = \left[\frac{\beta_p^2}{(\beta_e - \gamma)^2} - 1 \right] (\gamma^2 - k^2) \quad (21)$$

No Bessel functions of the second kind are included in Equation (20) because the potential Φ_{11} must be finite at $r = 0$. It is assumed that T^2 is positive and that the J_0 function is the solution to Equation (19) since, when the beam fills the drift tube, the potential given by Equation (20) must go to zero at the drift tube wall. The other possible solution, which is I_0 and which results when T^2 is negative, does not have zeros and would not go to zero at the drift tube wall.

In the region between the beam and the drift tube wall, the charge density is zero; therefore, from Equation (14), the electric scalar potential is

$$\Phi_{11} = C [I_0(\tau r) + DK_0(\tau r)] \quad r_b \leq r \leq r_c \quad (22)$$

where $\tau^2 = \gamma^2 - k^2$, r_c is the drift tube radius, C and D are arbitrary constants, and I_0 and K_0 are modified Bessel functions. These functions

are used because γ^2 (which is expected to be near β_e^2) is larger than k^2 and so τ^2 is positive. At r_c , the tangential electric field is zero, Φ_{11} is therefore zero, and

$$D = -\frac{I_0(\tau r_c)}{K_0(\tau r_c)} \quad (23)$$

At the edge of the beam, the tangential electric field is continuous and consequently by Equations (10) and (12) the potential is continuous. This leads to the relation,

$$\frac{C}{B} = \frac{J_0(\tau r_b)}{I_0(\tau r_b) + DK_c(\tau r_b)} \quad (24)$$

A second equation for the ratio C/B may be determined by realizing that the tangential magnetic field is continuous at the edge of the beam. From Equation (11b), it is seen that only the z component of \underline{A} exists. From Equation (10) therefore, only the azimuthal component of \underline{B} exists, and the continuity of this quantity requires that $\partial A/\partial r$ be continuous. By examining the gradient of Equation (12), one can see that $\partial \Phi/\partial r$ must be continuous; therefore,

$$\frac{C}{B} = \frac{T J_1(\tau r_b)}{\tau [I_1(\tau r_b) - DK_1(\tau r_b)]} \quad (25)$$

Combining Equations (23), (24) and (25) gives the following transcendental equation relating T and τ :

$$\tau r_b \frac{J_1(\tau r_b)}{J_0(\tau r_b)} = \tau r_b \operatorname{bcn}h \tau r_b \left(\frac{r_c}{r_b} - 1 \right) \quad (26)$$

where $\operatorname{bcn}h$ is the Bessel hyperbolic cotangent and is given by Equation (A-14) in Research Report EE 495.

The method of solving Equation (26) is to plot the right- and the left-hand sides as functions of a common parameter x , for various values of r_c/r_b as is done in Figure 1. Then, given a value of τr_b and of r_c/r_b , the value of the right- and left-hand sides is known; consequently the values of Tr_b can be obtained. There is, of course, an infinite number of solutions, the first three of which are plotted in Figures 2a, b, and c. The smallest solution is labeled T_0 and is called the zero-rank radial propagation constant after Ramo.⁷ Higher-rank propagation constants are numbered successively from T_0 . One reason for labeling these constants in this manner can be seen from Figures 2a, b, and c. The function $J_0(Tr)$, which gives the radial variations of the beam parameters, has no zeros within the beam when T is T_0 , has one zero within the beam when T is T_1 and so on. As a result of this, and of Equation (22), which gives the shape of the electric scalar potential in the drift tube, the potential waves must have the shapes shown in Figure 3.

Beside yielding curves for τr_b versus Tr_b , Equation (26) provides important information about the orthogonality of the functions $J_0(T_0 r_b)$, $J_0(T_1 r_b)$..., since it may be written as

$$H_{1n} J_0(T_n r_b) + H_{2n} (T_n r_b) J_0'(T_n r_b) = 0 \quad , \quad n = 1, 2, \dots, \quad (27)$$

where H_{1n} is the right-hand side of Equation (26) and H_{2n} is unity. In Agnew's book⁹ on differential equations, theorem 7.8947 states: "Let $\alpha > -1$. If H_1 and H_2 are real constants, not both 0 and if the numbers $\lambda_1 b, \lambda_2 b, \dots$ are distinct positive zeros of the function,

$$H_1 J_\alpha(z) + H_2 z J_\alpha'(z) \quad , \quad 7.89471$$

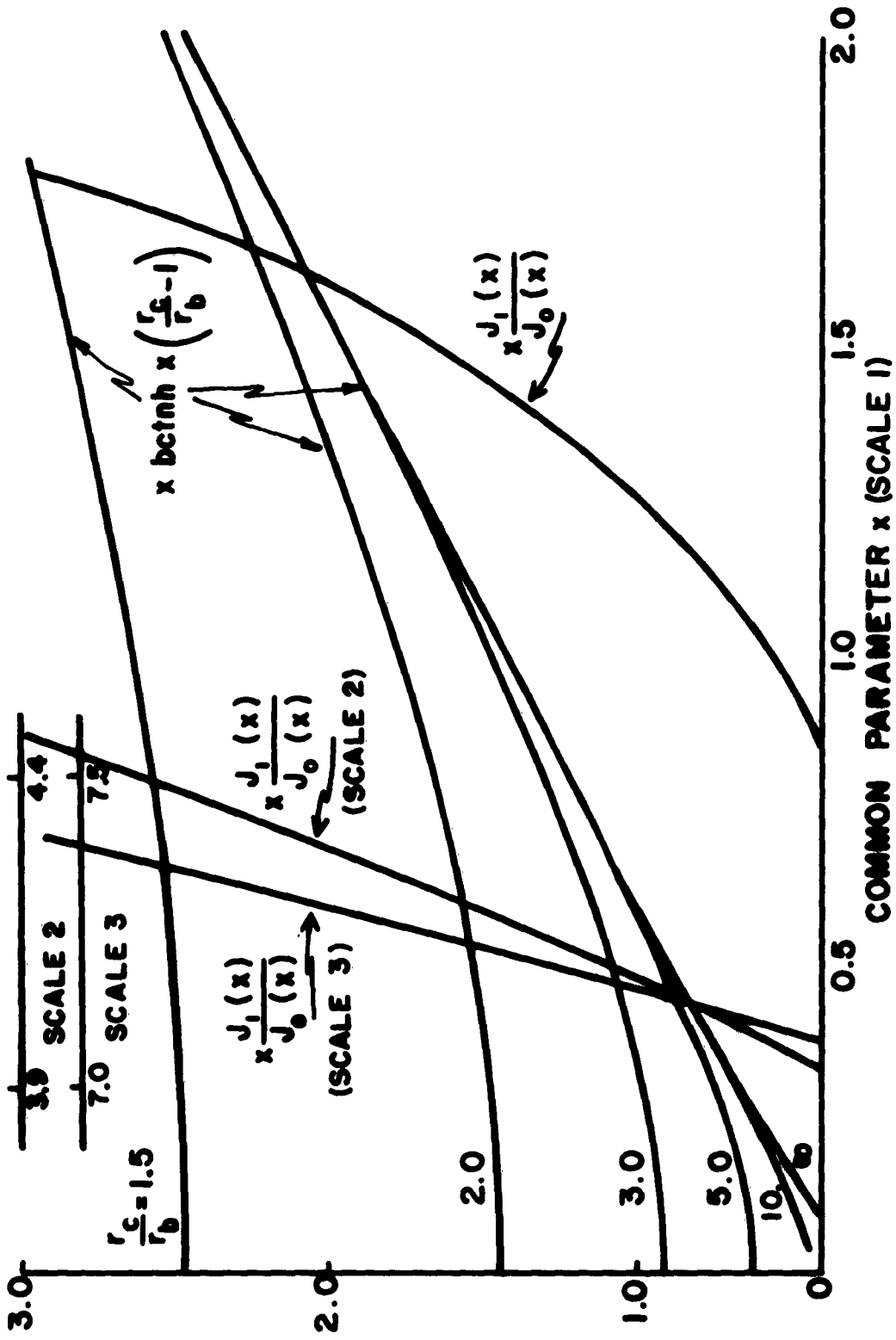


Figure 1. Curves for Determining τr_b as a Function of Tr_b .

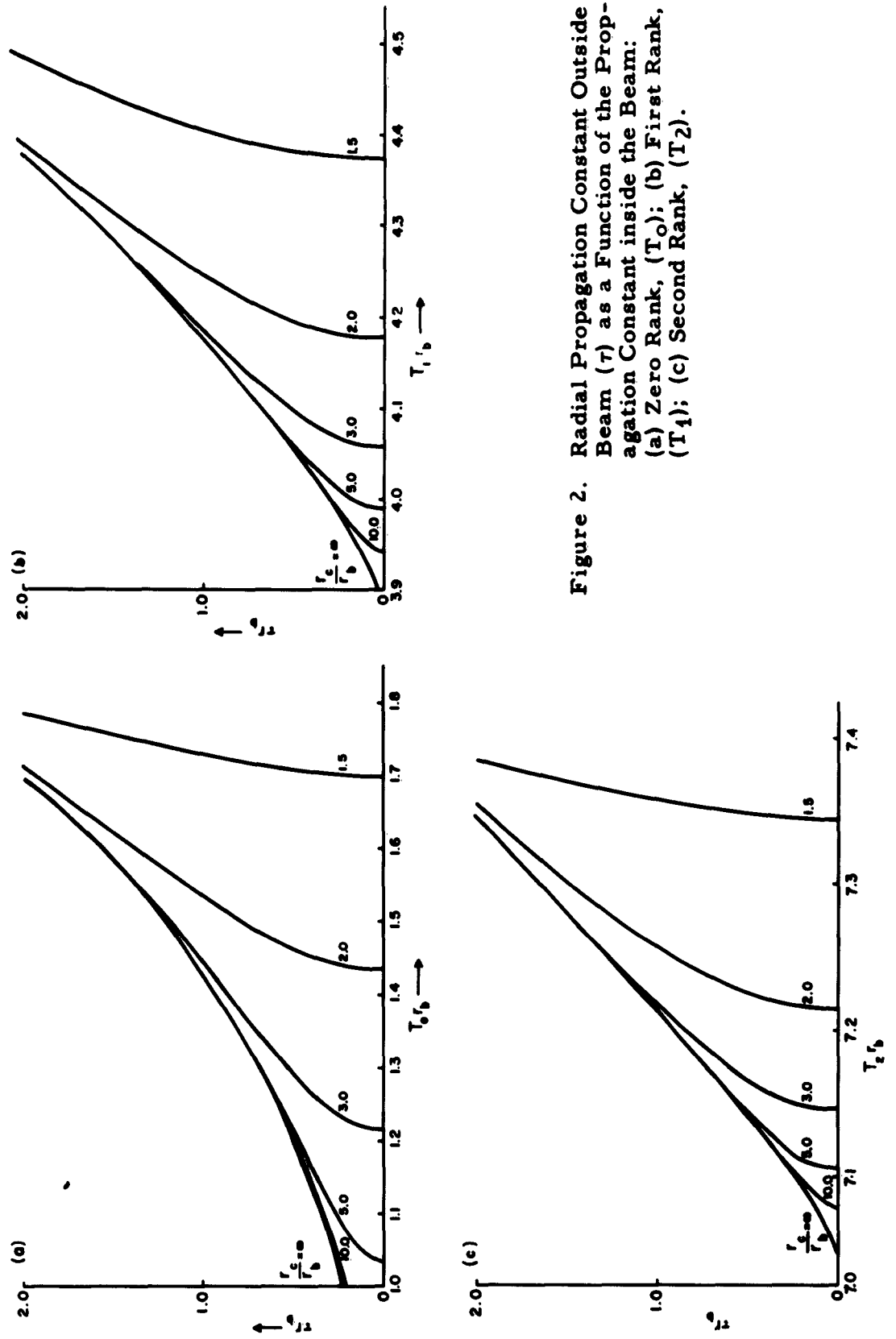


Figure 2. Radial Propagation Constant Outside Beam (γ_r) as a Function of the Propagation Constant inside the Beam: (a) Zero Rank, (T_0); (b) First Rank, (T_1); (c) Second Rank, (T_2).

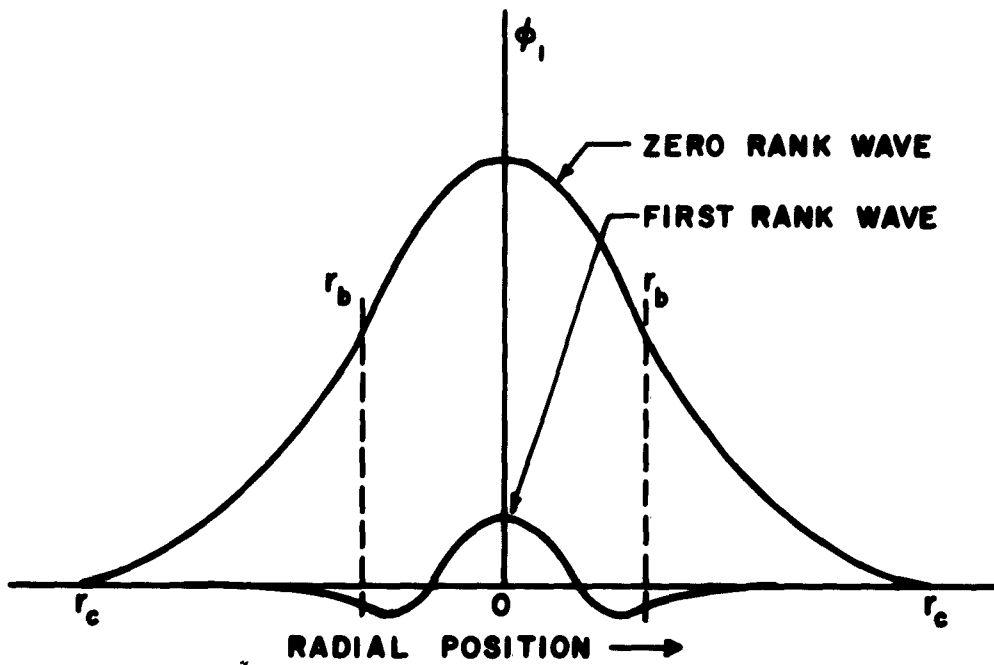


Figure 3. General Shapes of Zero- and First-Rank Electric Scalar Potential Waves.

then

$$\int_0^b x J_a(\lambda_j x) J_a(\lambda_k x) dx = 0 \quad 7.89472$$

when $j \neq k$.'' Equation (27) satisfies the requirements of this theorem so

$$\int_0^{r_b} r J_0(T_j r) J_0(T_k r) dr = 0 \quad ,$$

when $j \neq k$; that is, the functions $J_0(T_j r)$ and $J_0(T_k r)$ are orthogonal

with weight function r on the interval $0 \leq r \leq r_b$. As a result, the potential distribution in the beam can be expressed as a Fourier series of J_0 Bessel functions; that is, Φ_{11} may be written as

$$\Phi_{11} = \sum_{n=0}^{\infty} \phi_{1n} J_0(T_n r) \quad \text{for } r \leq r_b .$$

By using the orthogonality condition, one can express the coefficients ϕ_{1n} as

$$\phi_{1n} = \frac{\int_0^{r_b} r \Phi_{11} J_0(T_n r) dr}{\int_0^{r_b} r J_0^2(T_n r) dr} \quad \text{for } r \leq r_b ,$$

or as

$$\phi_{1n} = \frac{2T_n^2 \int_0^{r_b} r \Phi_{11} J_0(T_n r) dr}{\left[(T_n r_b)^2 + H_{1n}^2 \right] J_0^2(T_n r_b)} \quad \text{for } r \leq r_b . \quad (28)$$

By assuming that $k^2 \ll \gamma^2$ and by writing $\gamma = \beta_e + F\beta_p$, where F is called the plasma reduction factor and is a measure of the decrease in the plasma frequency caused by the bulging of the electric field lines in and near a finite beam, one can write Equation (21) as follows:

$$F = \pm \sqrt{\frac{1}{1 + \left(\frac{T}{\gamma}\right)^2}} . \quad (29)$$

Now, using curves similar to those shown in Figures 2 a, b, and c gives

the well-known curves^{10, 11} shown in Figure 4a, as well as the curves shown in Figure 4b for $|F_n|$ as a function of γr_b , where the subscript n refers to the rank of the reduction factor. In a small region about any given value of γr_b , any of the curves in Figures 4a and b may be considered to be linear; therefore $|F_n|$ may be written as

$$|F_n| = m_n \gamma r_b + b_n \quad ,$$

where the values of m_n and b_n may be found by letting $\gamma r_b = \beta_e r_b$. Finally, to find the propagation constant associated with the n^{th} wave, the linear approximation for F may be placed in $\gamma = \beta_e$,

$$\gamma_n = \beta_e \pm \beta_p (m_n \gamma r_b + b_n) \quad ,$$

or

$$\gamma_n = \frac{\beta_e \pm \beta_p b_n}{1 \mp m_n \beta_p r_b} \quad . \quad (30)$$

Since the product $m_n \beta_p r_b$ is usually small compared to unity (for the beam tester, $m_n \cong .5$ and $\beta_p r_b \cong .2$), Equation (30) may be rewritten as

$$\gamma_{n+} = \beta_e + \delta_n + F'_n \beta_p = \beta_e + \beta_{qn+} \quad , \quad (31)$$

$$\gamma_{n-} = \beta_e + \delta_n - F'_n \beta_p = \beta_e - \beta_{qn-} \quad ,$$

where

$$\delta_n = \beta_e (m_n \beta_p r_b)^2 + m_n \beta_p^2 r_b b_n \quad ,$$

and

$$F'_n = m_n \beta_e r_b + b_n \quad .$$

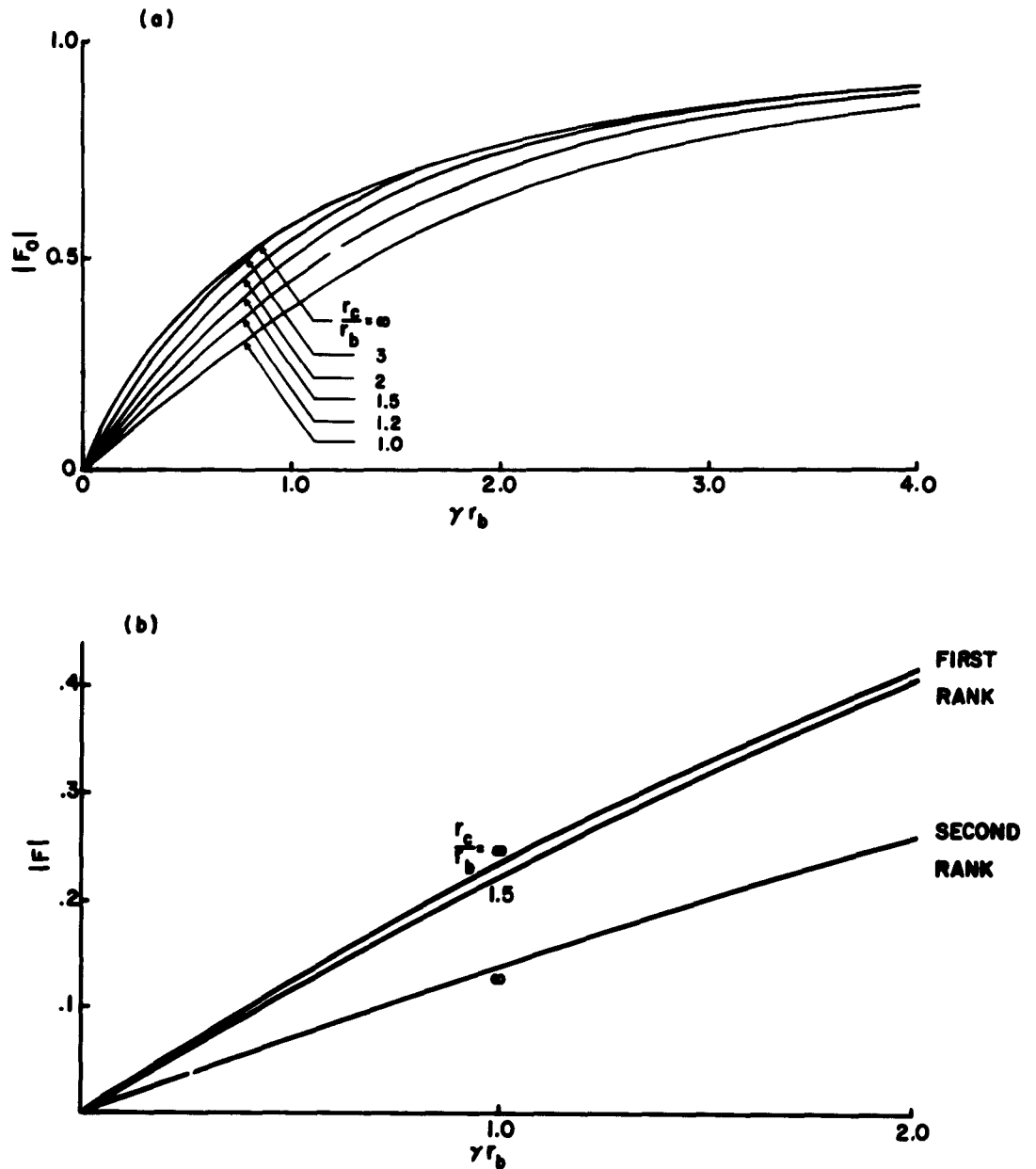


Figure 4. (a) Zero-Rank Plasma-Frequency Reduction Factor as Function of γr_b and r_c/r_b ; (b) First- and Second-Rank Plasma-Frequency Reduction Factors as Functions of γr_b and r_c/r_b .

The propagation constants γ_{n+} and γ_{n-} correspond to n^{th} rank fast and slow space-charge waves respectively, that is, waves traveling slightly faster and slightly slower than the d-c beam. The terms β_{qn+} and β_{qn-} are called the reduced-plasma propagation constants. It is noted that the wave velocities are not symmetrical relative to the beam velocity. This effect was first pointed out by Hahn¹² and later by Wang and McIsaac.¹³ In Equation (13), it was assumed that P_1 varies as $e^{-j\gamma z}$, so that by making a radial expansion for P_1 the expression for n^{th} wave, p_{1n} may be written as

$$p_{1n} = c_{n-} e^{-j(\beta_e - \beta_{qn-})z} + c_{n+} e^{-j(\beta_e + \beta_{qn+})z},$$

where

$$P_1 = \sum_{n=0}^{\infty} p_{1n} J_0(T_n r)$$

therefore

$$\dot{p}_{1n} = ju_0 \left[c_{n-} \beta_{qn-} e^{-j(\beta_e - \beta_{qn-})z} - c_{n+} \beta_{qn+} e^{-j(\beta_e + \beta_{qn+})z} \right], \quad (32)$$

and c_{n-} and c_{n+} may differ in magnitude when the fast and slow space-charge waves are launched at the modulating cavity with different amplitudes. If the fast and slow position waves are launched with equal amplitudes and of opposite sign then

$$\dot{p}_{1n} = ju_0 |c_n| \left[(F'_n \beta_p - \delta_n) e^{-j(\beta_e - \beta_{qn-})z} + (F'_n \beta_p + \delta_n) e^{-j(\beta_e + \beta_{qn+})z} \right], \quad (33)$$

and the magnitudes of the two differ by $2\delta_n$.

Figure 5 shows how the zero, first- and second-rank velocity space-charge waves, described by Equation (33), appear when $\beta_e r_b \cong 1.0$.

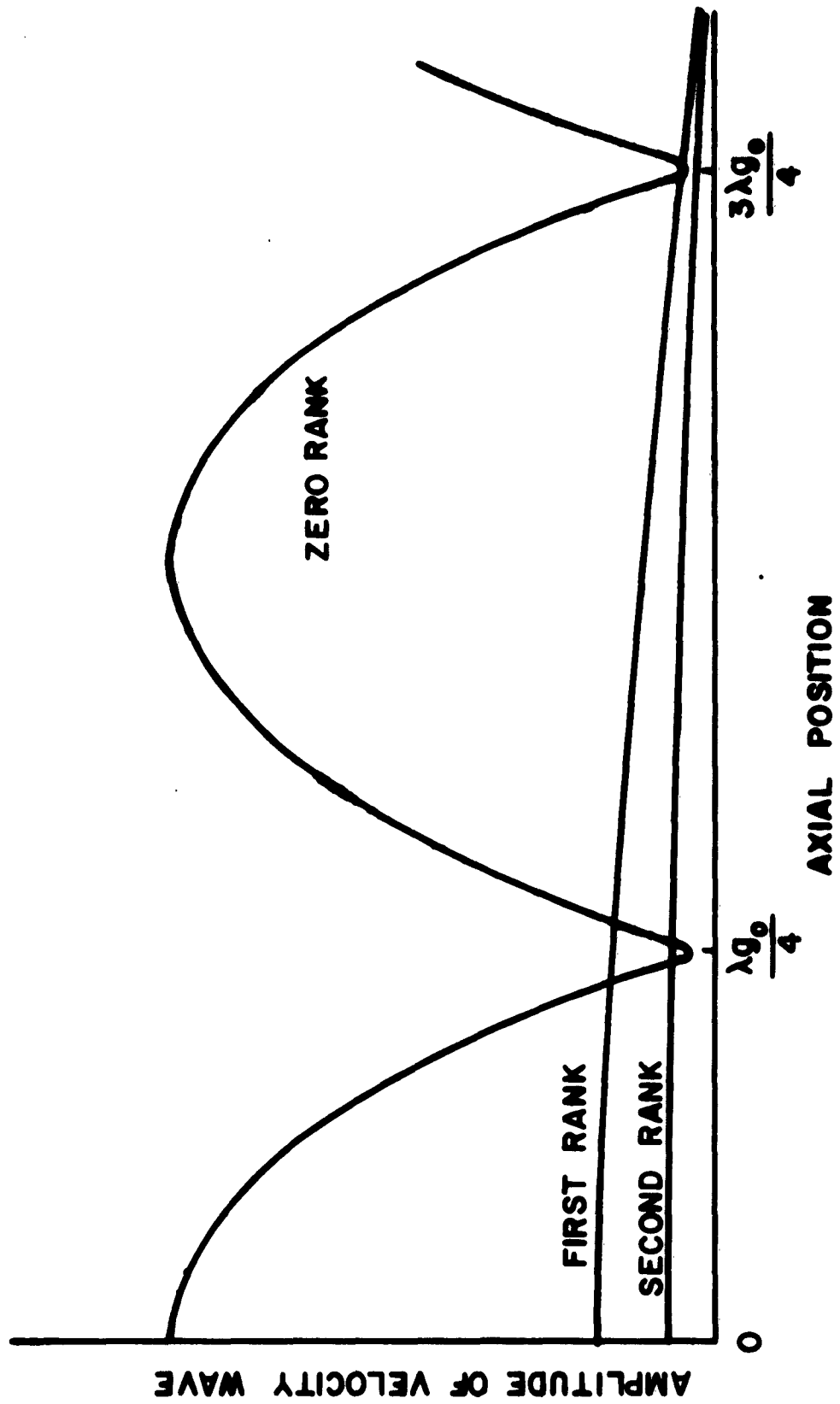


Figure 5. Velocity Standing Waves for $\beta_e r_b \approx 1.0$.

2 Initial Conditions

In order to determine the amplitudes of the space waves on the beam, it is necessary to investigate the interaction of the modulating-cavity fields with the waves. The equation to be solved in the interaction region is Equation (5), which is

$$\frac{\partial \dot{P}_1}{\partial t} + u_0 \frac{\partial \dot{P}_1}{\partial z} = -\eta(\underline{E}_{s1} + \underline{E}_{c1}) \quad , \quad (5)$$

and in order to solve this, \underline{E}_{s1} must be expressed in terms of \underline{P}_1 or $\dot{\underline{P}}_1$. This may be done by considering Gauss' law and the continuity equation; that is

$$\underline{\nabla} \cdot \underline{E}_{s1} = -\frac{\rho_1}{\epsilon_0} \quad , \quad (34)$$

and

$$\underline{\nabla} \cdot (\rho_0 \dot{\underline{P}}_1 + \underline{u}_0 \rho_1) = -\frac{\partial \rho_1}{\partial t} \quad ; \quad (35)$$

but $\dot{\underline{P}}_1$ and \underline{u}_0 are directed in the z direction so Equation (35) becomes

$$\rho_0 \frac{\partial}{\partial z} \dot{P}_1 = -\left(\frac{\partial}{\partial t} + u_0 \frac{\partial}{\partial z}\right) \rho_1 \quad . \quad (36)$$

The right-hand side of Equation (36) is simply $-\dot{\rho}_1$, so Equation (36) may be integrated to obtain

$$\rho_0 \frac{\partial}{\partial z} P_1 = -\rho_1 \quad , \quad (37)$$

where the constant of integration is zero because at $t = 0$, $\rho_1 = 0$ and $P_1 = 0$, therefore by Equation (34),

$$\underline{\nabla} \cdot \underline{E}_{s1} = \frac{\rho_0}{\epsilon_0} \frac{\partial}{\partial z} P_1 \quad . \quad (38)$$

Since

$$\dot{P}_1 = \frac{\partial}{\partial t} P_1 + u_0 \frac{\partial}{\partial z} P_1$$

and since P_1 and \dot{P}_1 are assumed to have only z-directed components (confined flow), Equation (5) may be written as

$$\frac{\partial^2}{\partial t^2} P_1 + 2u_0 \frac{\partial^2}{\partial t \partial z} P_1 + u_0^2 \frac{\partial^2}{\partial z^2} P_1 = -\eta(E_{s1} + E_{c1}) \quad (39)$$

Since all quantities vary as $e^{j\omega t}$, Equation (39) may be written as

$$\frac{\partial^2}{\partial z^2} P_1 + 2j\beta_e \frac{\partial}{\partial z} P_1 - \beta_e^2 P_1 = -\frac{\eta}{u_0} (E_{s1} + E_{c1}) \quad (40)$$

In the case of the infinite beam, Equation (38) reduces to

$$E_{s1} = \frac{\rho_0}{\epsilon_0} P_1 \quad (41)$$

because the beam has no radial variations. As a result, Equation (40) may be written as

$$\frac{\partial^2}{\partial z^2} P_1 + 2j\beta_e \frac{\partial}{\partial z} P_1 - (\beta_e^2 - \beta_p^2) P_1 = -\frac{\eta}{u_0} E_{c1} \quad (42)$$

When the beam is not infinite, the plasma frequency is smaller than ω_p and is ω_{q+} for the fast wave, and ω_{q-} for the slow wave. Since ω_q is not the same for the higher-rank waves as for the zero-rank wave, and since the electric field E_{c1} must be expressed as the sum of higher-rank

waves as follows, then

$$E_{c1} = \sum_{n=0}^{\infty} e_{c1n} J_0(T_n r) \quad (43)$$

Equation (42) may be written for the n^{th} wave as

$$\frac{\partial^2}{\partial z^2} p_{1n} + j(2\beta_e + \beta_{qn+} - \beta_{qn-}) \frac{\partial}{\partial z} p_{1n} - (\beta_e + \beta_{qn+})(\beta_e - \beta_{qn-}) p_{1n} = -\frac{\eta}{u_0} e_{c1n} \quad (44)$$

where

$$P_1 = \sum_{n=0}^{\infty} p_{1n} J_0(T_n r) \quad (45)$$

The solution to Equation (44) is well known¹⁴ and is

$$p_{1n} = e^{-j(\beta_e - \beta_{qn-})z} \int_0^z \left[e^{-j(\beta_{qn-} + \beta_{qn+})s} \int_0^s e^{j(\beta_e + \beta_{qn+})t} \left(-\frac{\eta}{u_0} e_{c1n} \right) dt \right] ds \quad (46)$$

It is shown in the Appendix (by the results from electrolytic tank measurements) that, for the particular geometry of the cavity used on the beam tester, the electric field E_c is very nearly independent of radius for $r \leq r_b$ and that the axial variation is approximated well by

$$E_{c1} = -\frac{\beta_c V_1}{2\pi a} (1 - \cos \beta_c z) \quad , \quad 0 \leq \beta_c z \leq 2\pi \quad (47)$$

where V_1 is the peak voltage across the cavity gap. The Fourier co-

efficiency e_{c1n} may be determined in terms of E_{c1} by using Equation (28), that is

$$e_{c1n} = \frac{2T_n^2 E_{c1} \int_0^{r_b} r J_0(T_n r) dr}{\left[(T_n r_b)^2 + H_{1n}^2 \right] J_0^2(T_n r_b)} \quad \text{for } r \leq r_b \quad (48)$$

With the aid of Equations (47) and (26), this may be written as

$$e_{c1n} = \frac{-\beta_c V_1 H_{1n}}{\pi a \left[(T_n r_b)^2 + H_{1n}^2 \right] J_0(T_n r_b)} (1 - \cos \beta_c z) ; \quad (49)$$

therefore Equation (46) becomes

$$P_{1n} = \frac{\beta_c A_n}{4\pi} e^{-j(\beta_e - \beta_{qn-})z} \int_0^z \left[e^{-j(\beta_{qn-} + \beta_{qn+})s} \int_0^s e^{j(\beta_e + \beta_{qn+})t} (1 - \cos \beta_c t) dt \right] ds , \quad (50)$$

for $0 \leq \beta_c z \leq 2\pi$, where

$$A_n = \frac{2H_{1n}}{\left[(T_n r_b)^2 + H_{1n}^2 \right] J_0(T_n r_b)} \quad (51)$$

At $\beta_c z = 2\pi$, the circuit electric field has decreased to zero and P_{1n} must be

$$P_{1n} = c_{n-} e^{-j(\beta_e - \beta_{qn-})z} + c_{n+} e^{-j(\beta_e + \beta_{qn+})z} \quad (52)$$

The constants c_{n-} and c_{n+} are therefore evaluated at $z = 2\pi/\beta_c$ where

p_{1n} and $\partial/\partial z p_{1n}$ are continuous. If the values of p_{1n} and $\partial/\partial z p_{1n}$ from Equation (50) at $z = 2\pi/\beta_c$ are called c_{1n} and c_{2n} respectively, then at $z = 2\pi/\beta_c$, Equation (52) becomes

$$c_{1n} = c_{n-} e^{-j(\beta_e - \beta_{qn-}) \frac{2\pi}{\beta_c}} + c_{n+} e^{-j(\beta_e + \beta_{qn+}) \frac{2\pi}{\beta_c}},$$

and $\partial/\partial z$ of Equation (52) becomes

$$c_{2n} = -j(\beta_e - \beta_{qn-}) c_{n-} e^{-j(\beta_e - \beta_{qn-}) \frac{2\pi}{\beta_c}} - j(\beta_e + \beta_{qn+}) c_{n+} e^{-j(\beta_e + \beta_{qn+}) \frac{2\pi}{\beta_c}},$$

from which

$$c_{n-} = \frac{c_{2n} + j(\beta_e + \beta_{qn+}) c_{1n}}{j(\beta_{qn-} + \beta_{qn+})} e^{j(\beta_e - \beta_{qn-}) \frac{2\pi}{\beta_c}}, \quad (53)$$

and

$$c_{n+} = \frac{c_{2n} + j(\beta_e - \beta_{qn-}) c_{1n}}{j(\beta_{qn-} + \beta_{qn+})} e^{j(\beta_e + \beta_{qn+}) \frac{2\pi}{\beta_c}}. \quad (54)$$

With the use of Equation (50) these two equations can be written as

$$c_{n-} = \frac{\beta_c A_{n-}}{4\pi j(\beta_{qn-} + \beta_{qn+})} \int_0^{\frac{2\pi}{\beta_c}} e^{j(\beta_e - \beta_{qn-})z} (1 - \cos \beta_c z) dz, \quad (55)$$

and

$$c_{n+} = - \frac{\beta_c A_{n+}}{4\pi j(\beta_{qn-} + \beta_{qn+})} \int_0^{\frac{2\pi}{\beta_c}} e^{j(\beta_e + \beta_{qn+})z} (1 - \cos \beta_c z) dz, \quad (56)$$

where it has been noted that the values of A_n for the fast and slow waves are not the same because the values of T_n differ. Integrations of the right-hand sides of Equations (55) and (56) yield

$$c_{n-} = \frac{A_{n-}}{2j(\beta_{qn-} + \beta_{qn+})} M_{n-} e^{j \frac{\theta_{n-}}{2}} \quad (57)$$

and

$$c_{n+} = - \frac{A_{n+}}{2j(\beta_{qn-} + \beta_{qn+})} M_{n+} e^{j \frac{\theta_{n+}}{2}} \quad (58)$$

The M_{n-} and M_{n+} terms are the gap-coupling coefficients for the n^{th} rank slow and fast space-charge waves and are given by

$$M_{n-} = \frac{(2\pi)^2}{(2\pi)^2 - \theta_{n-}^2} \frac{\sin \frac{\theta_{n-}}{2}}{\frac{\theta_{n-}}{2}}, \quad (59)$$

$$M_{n+} = \frac{(2\pi)^2}{(2\pi)^2 - \theta_{n+}^2} \frac{\sin \frac{\theta_{n+}}{2}}{\frac{\theta_{n+}}{2}}, \quad (60)$$

where

$$\theta_{n-} = \frac{\beta_e - \beta_{qn-}}{\beta_c} 2\pi, \quad (61)$$

and

$$\theta_{n+} = \frac{\beta_e + \beta_{qn+}}{\beta_c} 2\pi \quad (62)$$

A plot of M as a function of θ is given in Figure 6. A plot of $\frac{\sin \frac{\theta}{3.28}}{\frac{\theta}{3.28}}$ is also given to show that for values of θ less than 2π radians, the actual field configuration, i. e., $1 - \cos \beta_c z$, can be approximated by a rectangular field pattern.

It is interesting to notice that, since $\theta_{n\pm} = (\beta_e \pm \beta_{qn\pm}) 2\pi/\beta_c$, the gap-coupling coefficient of the fast space-charge wave is smaller than that for the slow space-charge wave. For example, if $\beta_e/\beta_c = 1$, and if $\beta_{q1\pm}/\beta_c = 0.1$, then M_{1-} is .573 and M_{1+} is .425; therefore M_{1-} is 35 per cent higher than M_{1+} .

By using Equations (57) and (58) for the constants c_{n-} and c_{n+} , Equation (52) becomes

$$P_{1n} = \frac{1}{2j(\beta_{qn-} + \beta_{qn+})} \left[A_{n-} M_{n-} e^{-j(\beta_e - \beta_{qn-})z} - A_{n+} M_{n+} e^{-j(\beta_e + \beta_{qn+})z} \right] \quad (63)$$

where the $z = 0$ position has been shifted to the center of the gap. The $(\beta_{qn-} + \beta_{qn+})$ term in the denominator of Equation (63) is very small for large n ; however, then $\beta_{qn-} \cong \beta_{qn+}$ and so p_{1n} becomes

$$P_{1n} = \frac{A_n M_n}{2} \frac{\sin \beta_{qn} z}{\beta_{qn}} e^{-j\beta_e z} \quad (64)$$

and $\sin \beta_{qn} z / \beta_{qn} \rightarrow 1$ as $\beta_{qn} \rightarrow 0$. Since $\dot{p}_{1n} = j u_o (\beta_e - \gamma) p_{1n}$, the

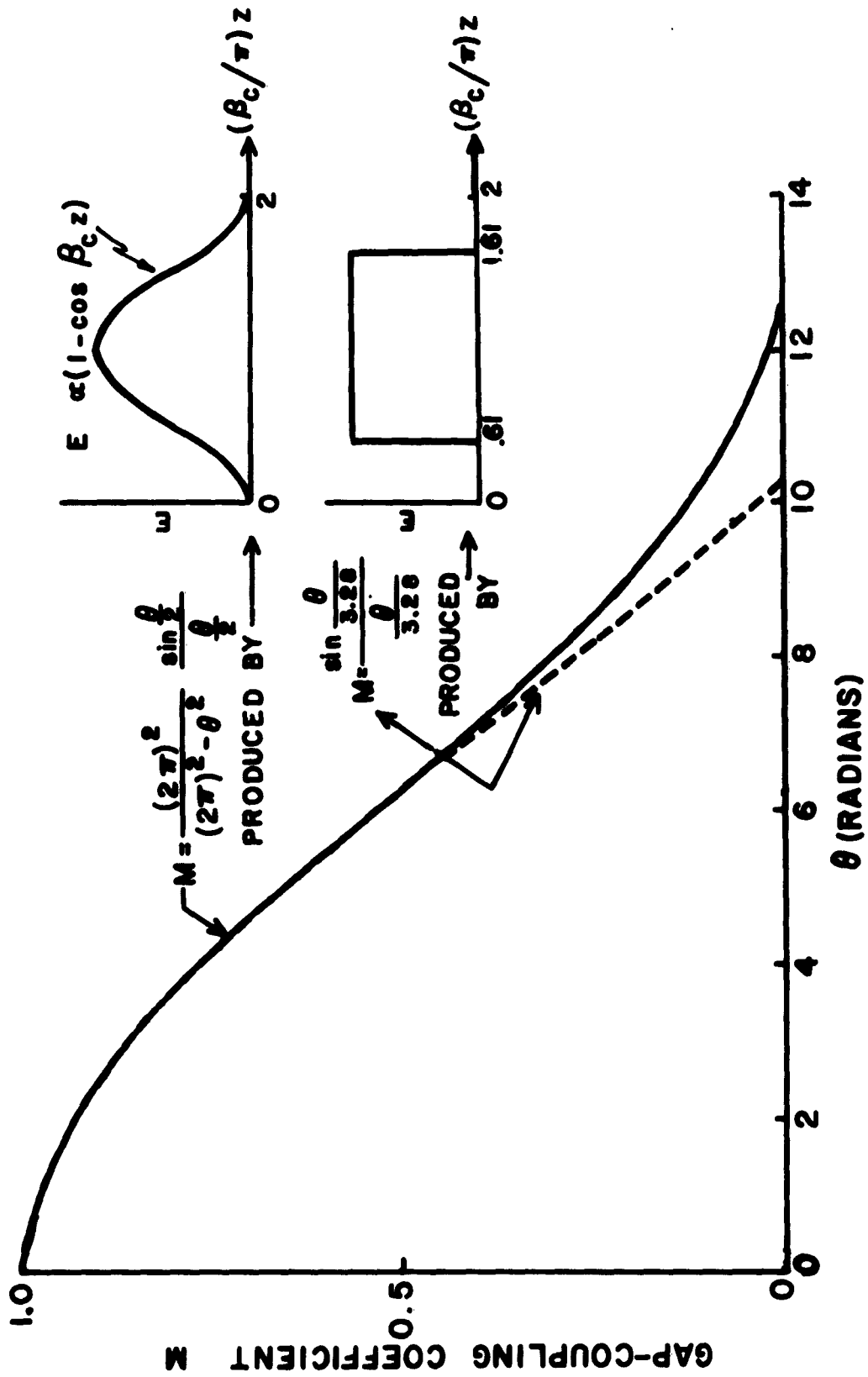


Figure 6. Gap-Coupling Coefficient M as Function of θ for Field Varying as $(1 - \cos \beta_c z)$ and for Same Field Averaged over $z = .61 \pi/\beta_c$ to $1.61 \pi/\beta_c$.

equation for the n^{th} rank velocity wave may be derived from Equation (63) and is

$$\dot{P}_{1n} = \frac{u_0}{2(\beta_{qn-} + \beta_{qn+})} \left[(F'_n \beta_p - \delta_n) A_{n-} M_{n-} e^{-j(\beta_e + \delta_n - F'_n \beta_p)z} + (F'_n \beta_p + \delta_n) A_{n+} M_{n+} e^{-j(\beta_e + \delta_n + F'_n \beta_p)z} \right], \quad (65)$$

where the linearized propagation constants given in Equation (30) have been used. It will be noticed that the condition described by Equation (33), that is where the amplitude of the two space-charge waves differed by $2\delta_n$, is modified because the product $(F'_n \beta_p - \delta_n) A_{n-} M_{n-}$ may be larger than, equal to, or smaller than $(F'_n \beta_p + \delta_n) A_{n+} M_{n+}$, depending on the magnitudes of δ_n , $A_{n+} M_{n+}$ and $A_{n-} M_{n-}$. Therefore when the amplitudes are equal, the zero rank velocity wave is not as shown in Figure 5 because the null of the wave actually goes to zero. Finally, since

$$\dot{P}_1 = e^{j\omega t} \sum_{n=0}^{\infty} \dot{P}_{1n} J_0(T_n r),$$

the first-order velocity \dot{P}_1 becomes

$$\dot{P}_1 = \frac{u_0}{2} e^{j\omega t} \sum_{n=0}^{\infty} \frac{1}{(\beta_{qn-} + \beta_{qn+})} \left[\beta_{qn-} M_{n-} A_{n-} J_0(T_n r) e^{jF'_n \beta_p z} + \beta_{qn+} M_{n+} A_{n+} J_0(T_{n+} r) e^{-jF'_n \beta_p z} \right] e^{-j(\beta_e + \delta_n)z}. \quad (66)$$

III. EXPERIMENTAL RESULTS AND THEIR COMPARISON WITH THEORY

A. TECHNIQUE FOR MAKING VELOCITY MEASUREMENTS

The method used to measure the peak velocity of the electron beam was that of applying a negative potential to the Faraday cage (see Research Report EE 4)5 for description of Faraday cage and associated positioning apparatus), which was just large enough to repel the electrons approaching the cage from the aperture in the movable beam collector. Since the current to the cage dropped rapidly from a constant value to zero as the cage potential was varied from the beam voltage plus a few volts to the beam voltage minus a few volts (see Figure 7), small changes in the beam velocity could be easily detected by observing the curve of the cage current versus voltage. The reason the curve of current versus voltage did not have a sharper cut-off than shown in Figure 7 is because the "beam voltage" was a 16.7- μ sec duration pulse (rise time = .2 μ sec, fall time = .3 μ sec) applied to the cathode of the beam tester, and the pulse droop was about 50 volts.

It was anticipated that a large number of velocity measurements would be required to determine the peak velocity distribution in the beam as functions of the amplitude of the velocity modulation and of the amount of scalloping on the beam. It was decided therefore that the velocity data should be recorded automatically in the same manner as the d-c current was recorded (see Research Report EE 495). The circuit devised to make velocity recording possible is shown in Figure 8. This circuit is essentially a voltage divider in which a fraction of the current approaching the cage was used to build up a bias voltage across the 10,000 M Ω resistor in series with the input resistance of the electrometer. This bias voltage

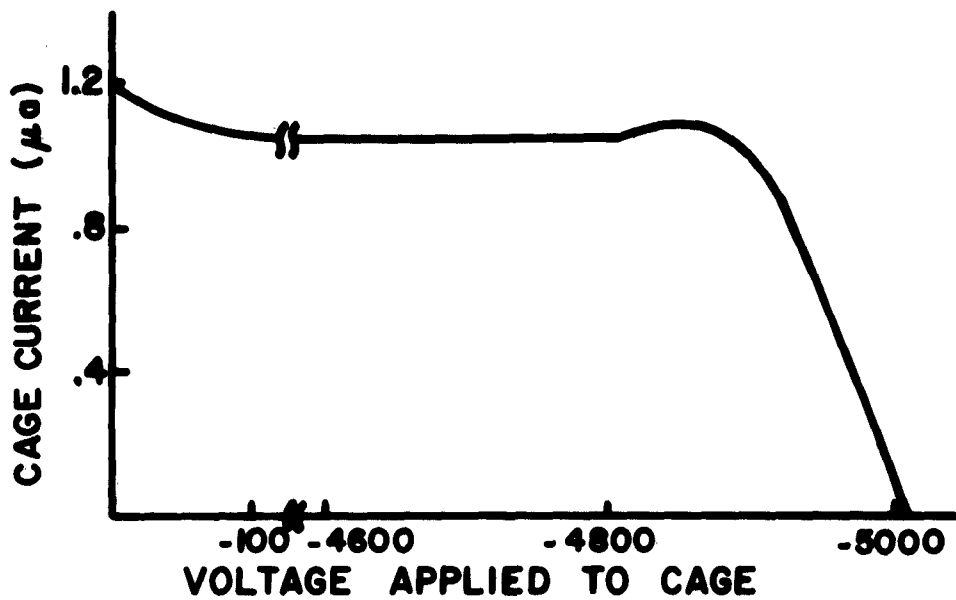


Figure 7. Current-Voltage Characteristic for Faraday Cage.

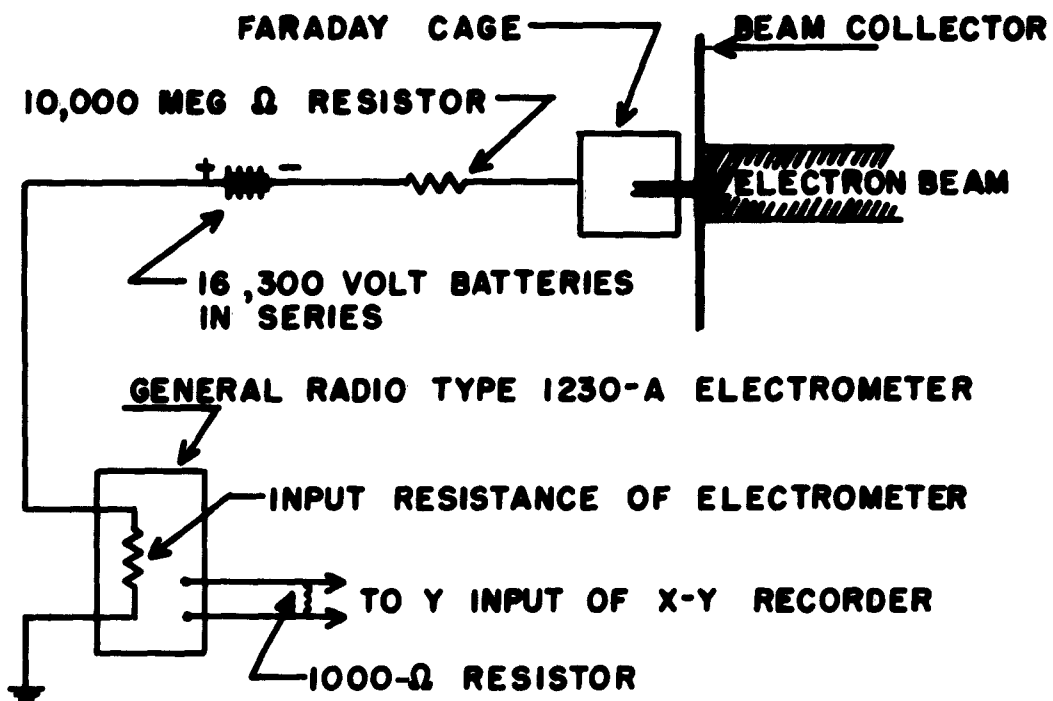


Figure 8. Circuit Used to Provide Peak Beam-Velocity Indication to X-Y Recorder.

in turn repelled the remaining part of the current approaching the cage and returned it to the beam collector. Sixteen 300-volt batteries were used to provide a cage bias just below the d-c beam voltage of 5000 volts. Therefore the voltage required across the 10,000-M Ω resistor was the difference between 4800 volts and the voltage equivalent of the peak velocity on the beam. At a beam voltage of 5000 volts, the bias current required was .02 μ a, which represented only two per cent of the total current of 1 μ a passing through the aperture under Brillouin flow conditions. As can be seen in Figure 7, the cage potential at a cage current of .02 μ a was essentially the peak voltage in the beam. When velocity modulation was applied to the beam, the peak velocity of the beam increased, therefore the current necessary to bias the cage increased. In addition, the voltage-current characteristic became more sloping, so that with 500 volts of modulation on the beam, the bias current was .07 μ a and the error in measuring the peak voltage was about -5 per cent. This error could have been reduced by using a resistor larger than 10 kM Ω ; however, then the time constants involved would have been too large to permit good data to be taken.

The input resistance switch of the electrometer was normally set on the 10⁸-ohm position so that the voltage into the electrometer was .01 of the voltage across the 10 kM Ω resistor. The output current from the electrometer was passed through a 1000- Ω resistor to provide a voltage input to the X-Y recorder.

Figures 9a and b show typical d-c current and velocity contours taken at the same axial position on the beam under Brillouin flow conditions. The horizontal and vertical axes indicate the horizontal and

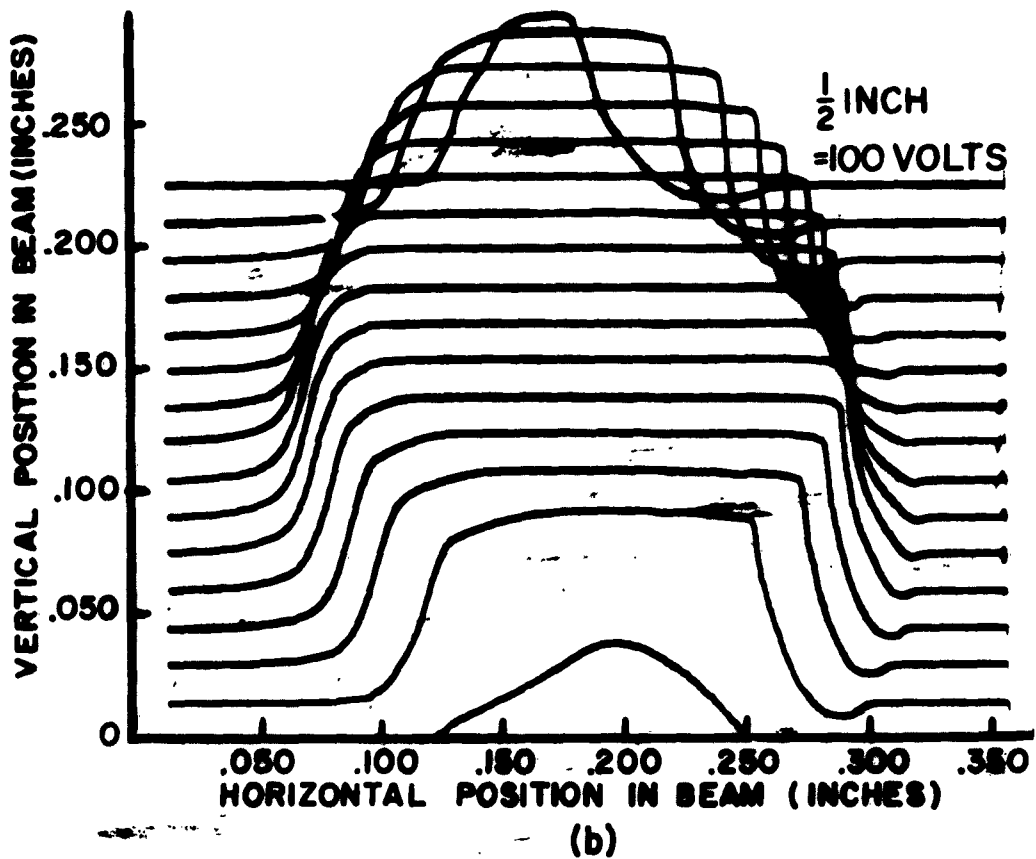
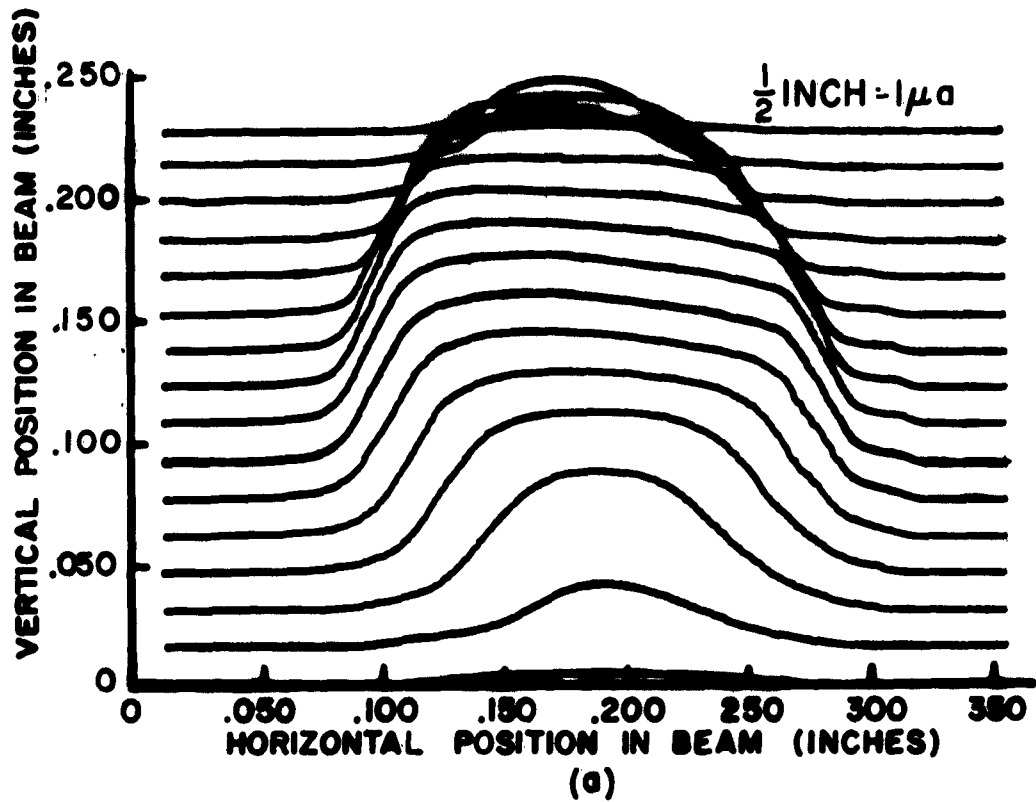


Figure 9. Contours Taken at the Same Axial Position on Beam under Brillouin Flow Conditions of (a) D-C Current (b) Velocity.

vertical positions in the beam, and the deflection at any point above a horizontal line is proportional to the amount of current or to the incremental velocity above 4800 volts on the beam. Notice that, even though the current contour is not quite symmetrical and is not flat in the center region, the velocity contour is perfectly flat and uniform over the central part of the beam, indicating a constant velocity across the beam, which is to be expected.

The small negative deflections on the right-hand side of the velocity contour are thought to have been caused by secondary emission from the Faraday cage. The part of the beam causing the negative deflections is the "tail" described in Research Report EE 495 which is thought to have been made up of reflected electrons traveling at a velocity slightly below the beam velocity (in fact at a velocity the voltage equivalent of which was very close to the cage bias battery potential). Because of the axial magnetic field in the beam region and the repelling potential on the cage, these electrons did not enter the cage, but instead struck the outer face of the cage between the cage and the back of the beam-collecting plate. As a result, it is probable that ratio of secondary to primary electrons was greater than unity, and that the total electron-current flow was from the cage to the beam-collecting plate. This reversed current, in turn, produced the positive potential across the $10\text{ k}\Omega$ resistor, which is indicated by the negative deflections on the velocity contour.

The reason that the velocity contour is not the same on the left side as it is on the right stems from the fact that data was taken while the Faraday cage was moving from right to left (the shape of the contour was found to reverse when data was taken from left to right). As the cage

moved into the beam, it first encountered the reflected electrons just mentioned and its potential became slightly positive. The cage next began to collect the main part of the beam, which was made up of primary electrons traveling at the cathode potential, and the cage potential therefore became negative. As the cage moved out of the beam, it remained above the bias battery potential because of the slow discharging of the R-C circuit made up of the cage-to-ground capacitance and the 10 k Ω resistor. The slow-moving reflected electrons therefore were not permitted to reach the cage, and no negative deflection resulted on the velocity contour.

B. BRILLOUIN BEAM RESULTS

This section gives the results of the measurements of the peak electron velocities in a velocity modulated Brillouin beam (less than two per cent scalloping) and compares them with the predictions of the confined-flow theory given in Section II B. Data, similar to that shown in Figure 10, were obtained by recording the d-c and the peak r-f beam velocities at various axial positions in the beam as the Faraday cage was moved horizontally through the beam at the beam's vertical center position. This data was taken at drive levels ranging from $a = .015$ to $a = .30$. In all cases, it was found that the variations in the peak velocity as a function of the radial position in the beam were small. In particular, under small-signal conditions (Figure 10 is a good example), the peak r-f velocity as a function of radius was found to be nearly constant.

As a result, the velocity of the entire beam was very nearly that shown by the curves in Figure 11. These were obtained by moving the

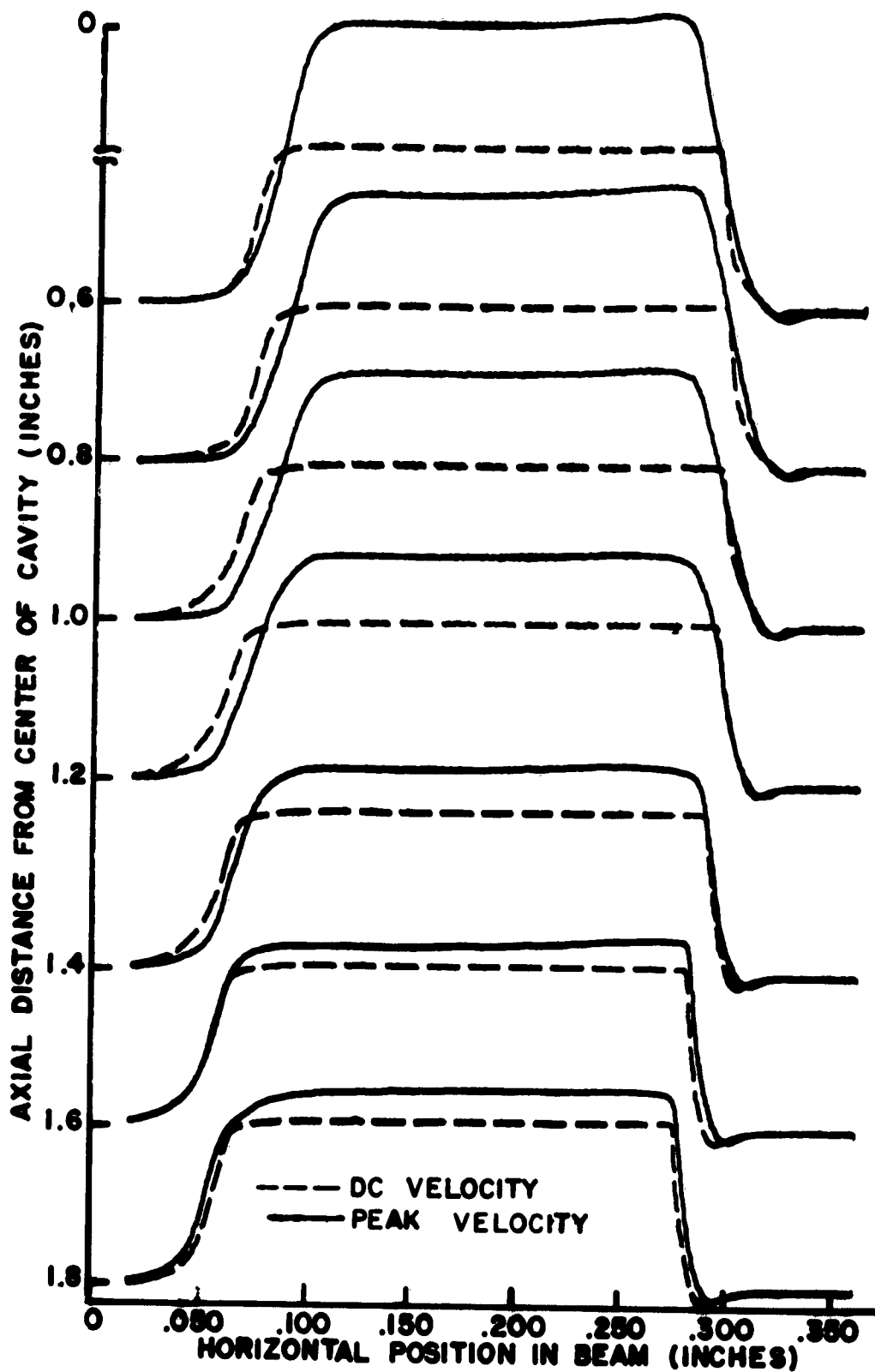


Figure 10. D-C and Peak Beam Velocities as a Function of the Axial and the Radial Positions in Beam.

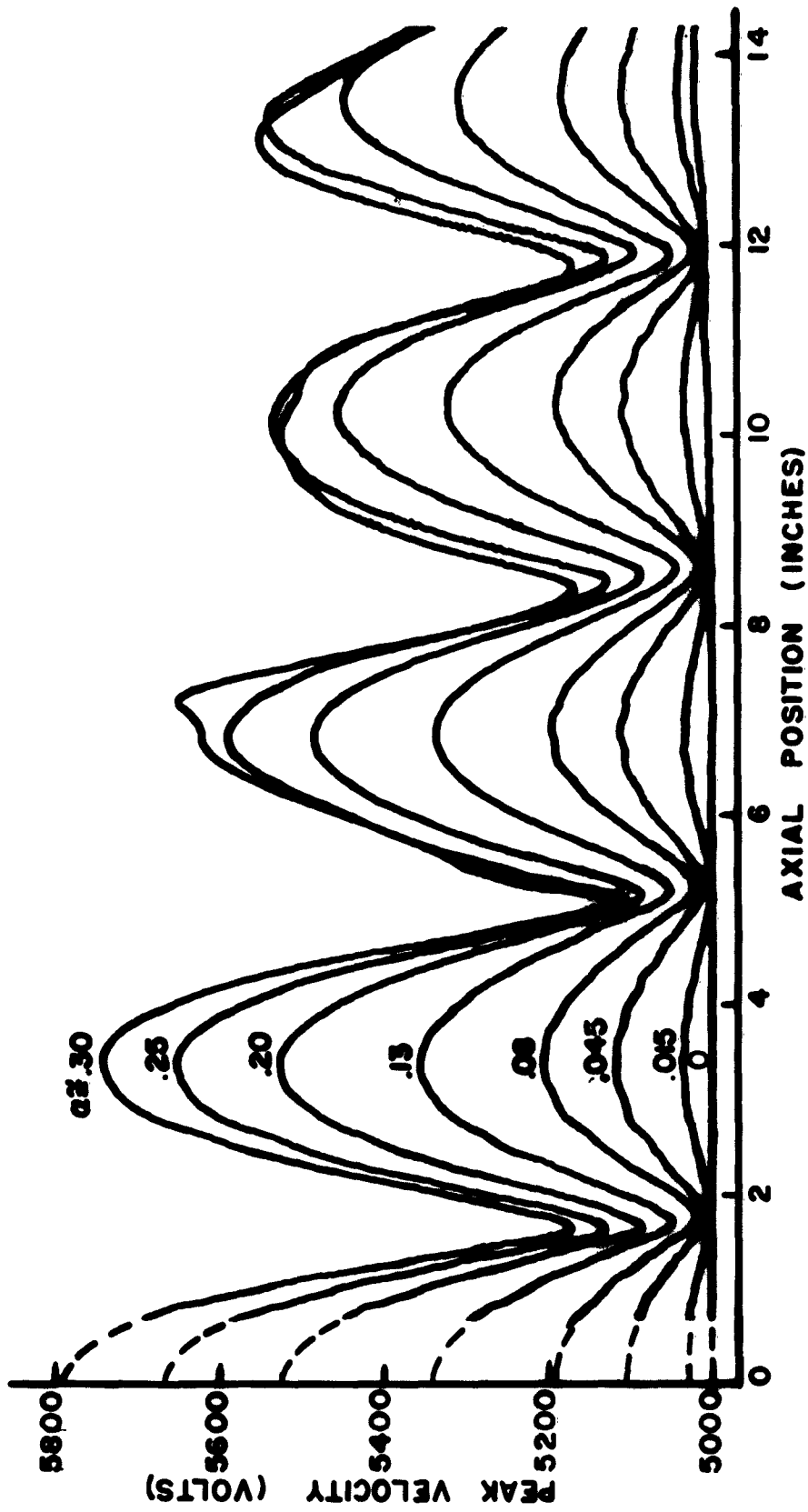


Figure 11. Peak Beam Velocity as Function of Axial Position and R-F Drive Level for Brillouin Flow Conditions.

cage to the center of the beam and by plotting the peak velocity as a function of axial position. The important points to notice about the standing waves shown in Figure 11 are (1) that at small-signal levels, the second velocity maxima is greater than the first, and succeeding maxima decrease as a function of distance, (2) that the nulls do not reach the d-c beam level, and (3) that at large-signal levels the amplitude decreases rapidly, and the shape of the standing-wave pattern deviates considerably from a series of half sinusoids. The first two of these items may be explained with the aid of Equation (66) if it is assumed that, even though the drift tube diameter is large enough for wave-guide modes to exist, these modes have phase velocities high enough that they do not interact with the beam. At the center of the beam, $J_0(T_{n\pm} r) = 1$, so Equation (66) may be written as

$$\dot{P}_1 = \frac{u_0}{2} \sum_{n=0}^{\infty} \frac{1}{(\beta_{qn-} + \beta_{qn+})} \left[\beta_{qn-} M_{n-} A_{n-} e^{jF'_n \beta_p z} + \beta_{qn+} M_{n+} A_{n+} e^{-jF'_n \beta_p z} \right] e^{j[\omega t - (\beta_e + \delta_n) z]} \quad (67)$$

The various constants for the zero-, first- and second-rank waves in the above equation may be evaluated with the aid of Figures 1 through 6, the geometry of the beam tester and the beam parameters. The amplitudes of the velocity waves are predicted to vary with distance as is shown in Figure 12. Since $\beta_{qn-} M_{n-} A_{n-}$ nearly equals $\beta_{qn+} M_{n+} A_{n+}$, only cosine waves are shown. The phases of the various waves vary as is shown in Figure 13, so that the sum of the zero-, first- and second-rank velocity waves is as shown by the dashed curve in Figure 14. In order to find out

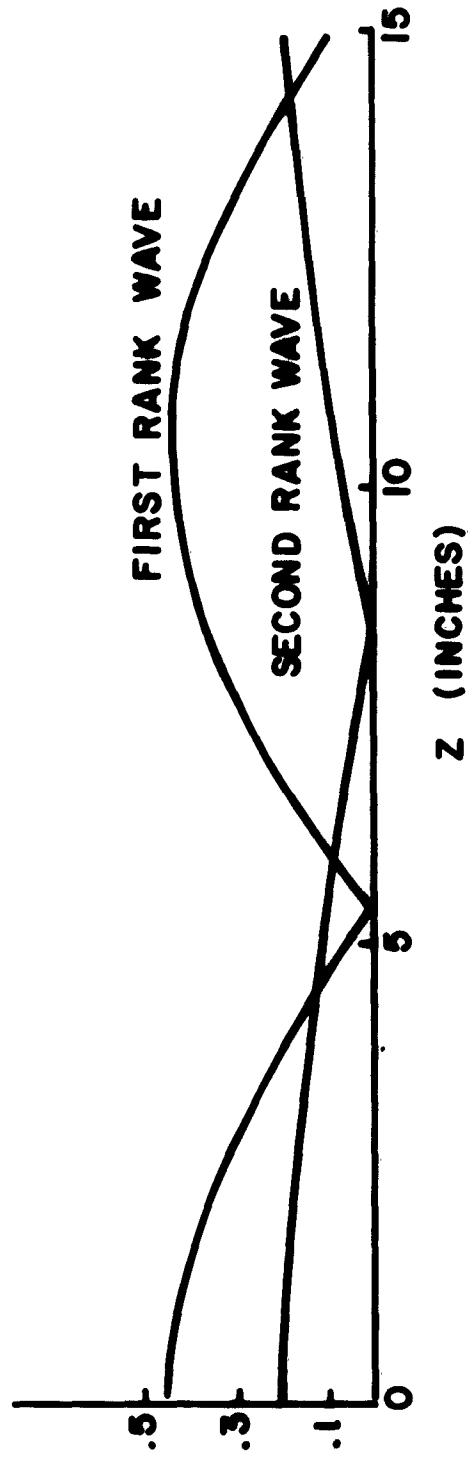
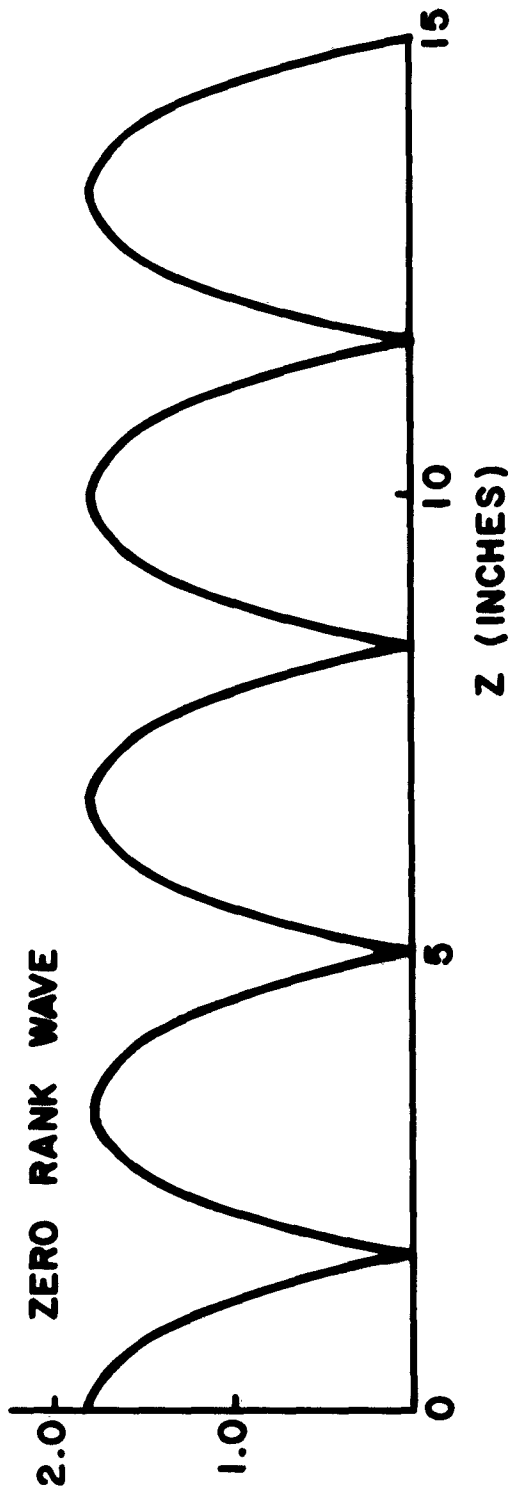


Figure 12. Amplitudes of Zero-, First- and Second-Rank Velocity Waves as Predicted by Equation (67) for Beam Tester.

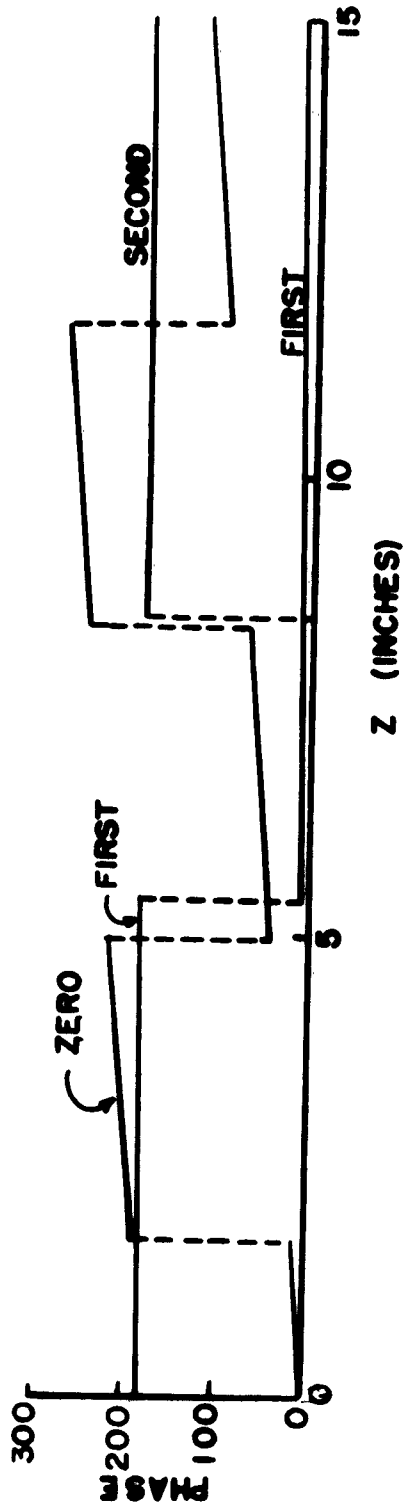


Figure 13. Phase Shift Relative to $\omega t - \beta_e z$ for the Zero-, First-, and Second-Rank Velocity Waves.

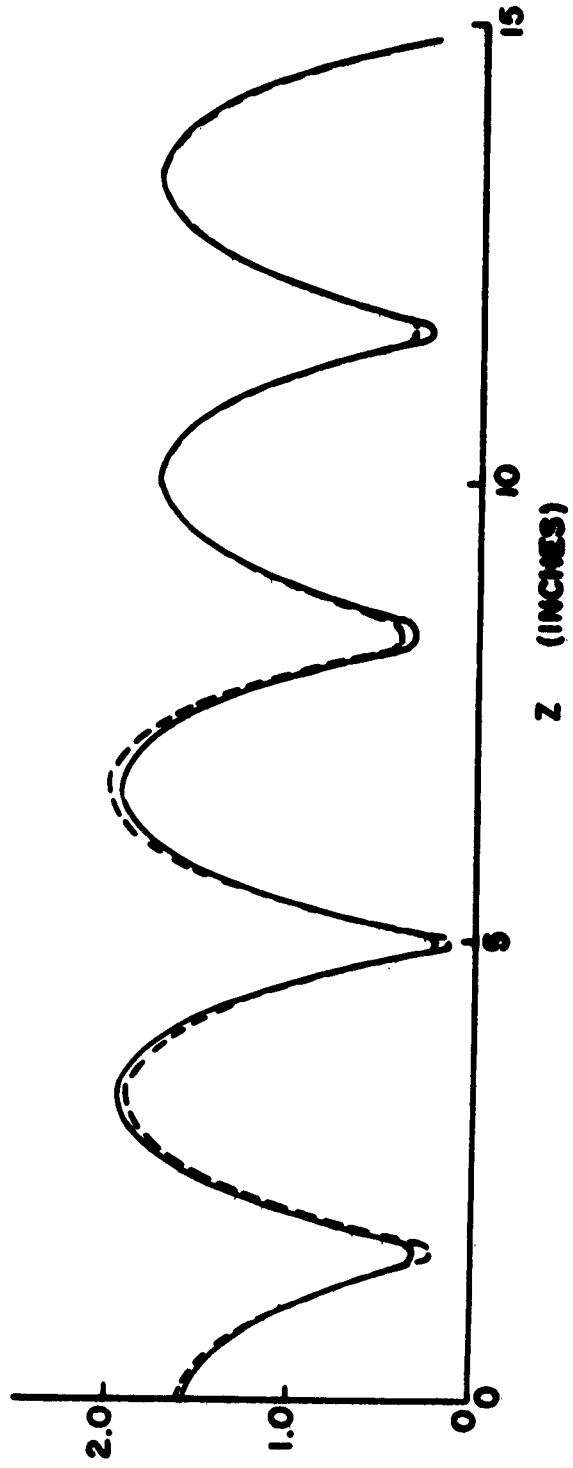


Figure 14. Sum of Zero-, First-, and Second-Rank Velocity Waves.

what the total velocity wave should look like, an estimate should be made of the effect of the waves of rank three and above.

Since the reduced plasma propagation constants are nearly equal for the higher-rank waves, the equation for the n^{th} velocity wave may be written as

$$\dot{P}_{1n} = \frac{u_o}{4} MA_n \left[e^{jF'_n \beta_p z} + e^{-jF'_n \beta_p z} \right] e^{j(\omega t - \beta_e z)} \quad (68)$$

where the gap-coupling coefficient M is the same for all the higher waves.

Thus it is seen that the amplitudes of the higher waves are governed by A_n which was given by Equation (51) as

$$A_n = \frac{2H_{1n}}{\left[(T_n r_b)^2 + H_{1n}^2 \right] J_0(T_n r_b)} \quad (51)$$

From Figure 1, it can be seen that the value of $T_n r_b$ for $n \geq 2$ is very nearly the n^{th} zero of

$$(T_n r_b) \frac{J_1(T_n r_b)}{J_0(T_n r_b)}$$

which is of course the n^{th} zero of $J_1(T_n r_b)$. (The zero at $T_n r_b = 0$ is the $n = 0$ zero). Jahnke and Emde¹⁵ give the n^{th} zero of $J_1(x)$ as being approximately equal to $\pi(n + \frac{1}{4})$; therefore A_n may be written as

$$A_n = \frac{2H_{1n}}{\left[\pi^2 \left(n + \frac{1}{4}\right)^2 + H_{1n}^2 \right] J_0\left[\pi \left(n + \frac{1}{4}\right)\right]} \quad (69)$$

The asymptotic relation for $J_0(x)$ for large values of x is

$$J_0(x) = \left(\frac{2}{\pi x}\right)^{\frac{1}{2}} \cos\left(x - \frac{\pi}{4}\right) \quad ;$$

therefore

$$J_0 \left[\pi \left(n + \frac{1}{4} \right) \right] = \frac{(-1)^n}{\pi} \left(\frac{2}{n + \frac{1}{4}} \right)^{\frac{1}{2}} \quad (70)$$

and A_n may be written as

$$A_n = \frac{\sqrt{2} H_{1n}}{\pi} \left[\frac{(-1)^n}{\left(n + \frac{1}{4} \right)^{3/2}} \right] \quad (71)$$

where $H_{1n}^2 \ll \pi^2 \left(n + \frac{1}{4} \right)^2$ has been used. If it is assumed the F_n' are small enough that the higher-ranking waves all vary in about same manner as a function of distance, then these waves can be added together to form a correction factor to the wave shown in Figure 14. This correction factor will decrease with distance, and even though the exact variation with distance will not be known, an estimate can be made of what the total velocity wave will look like.

After summing the A_n 's in Equation (71) it is found that the correction factor has a magnitude of about 0.05 at $z = 0$ and a phase of 180° relative to $\omega t - \beta_e z$. Since this correction decreases with distance, it is to be expected that the total velocity wave given by Equation (67) is as shown by the solid curve in Figure 14. This curve shows that the higher-rank waves cause the second velocity maxima to be greater than the first and that succeeding maxima decrease with distance. It must be noted, however, that the initial increase in the maxima is larger than that found experimentally. The percentage decrease in the succeeding maxima is predicted to be about 8 per cent by Equation (67) and is found to be closer 10 per cent in the experimental results. The ratio of the minimum to the

maximum velocity is predicted to be 0.14 and this is the same as the average of the small-signal experimental results. The major difference between the predicted and actual minima is that those shown in Figure 14 are not all at the same level whereas the minima resulting from the small-signal measurements are all at the same level.

At large-signal levels, Figure 11 shows that there is no initial increase in the velocity maxima. Also, the percentage decrease in the maxima is nearly 20 per cent as compared to 10 per cent at small-signal levels. Since the shape of the standing-wave pattern is no longer a series of half sinusoids at high-signal levels, it is to be expected that at least a second-order theory would be required to analyze these results.

In making computations for the curves shown in Figure 14, the reduced plasma wavelength used was taken from the curves in Figure 11. An experimental value for the plasma reduction factor can be obtained by comparing this reduced plasma wavelength with the plasma wavelength, which is the same as the d-c scallop wavelength of the Brillouin beam. If the scallop wavelength is taken directly from Figure 3-9 in Research Report EE 495, the value of F is found to be 0.42. If the cyclotron wavelength is multiplied by $\sqrt{2}$ to obtain the scallop wavelength, then the value of F is 0.453. The theoretical value of F from Figure 4a is .475, so that the discrepancies between this and the experimental results are 12 per cent and 5 per cent. It is probable that the experimental value of F that is valid is 0.42, since the error arising from the use of $\lambda_s = \sqrt{2} \lambda_c$ (see Research Report EE 495) is avoided. This agrees favorably with the value of .413, which can be computed by using the equation for the plasma reduction factor on a Brillouin beam as given by Beck¹⁶ (page 118).

Also of interest in the data in Figure 11 is the very small ripple that appears on the small-signal curves. The ratio of the wavelength of this ripple to the reduced plasma half wavelength is about 1 to 8, and this turns out to be the ratio of β_q to β_e ; therefore the small ripple appears to be a standing-wave varying as

$$\sin \beta_e z e^{j\omega t} .$$

One possible explanation for this is that the part of the beam which is reflected by the beam collector varies as $e^{j(\omega t + \gamma z)}$. This velocity wave interferes with the forward traveling waves to produce a component varying as

$$e^{j(\omega t + \gamma z)} + e^{j(\omega t - \gamma z)} = 2 \cos \gamma z e^{j\omega t} .$$

C. SCALLOPING BEAM RESULTS

This section deals with the measurements of the peak electron velocities in a scalloping d-c beam, which was velocity modulated. Plots of the beam velocity as a function of axial position and of drive power for a magnetic field 25 per cent greater than the Brillouin value are shown in Figure 15. With the exception of the decrease in wavelength, these curves are not much different from those shown in Figure 11 for the Brillouin flow case. There is an increase in the d-c level as a function of distance which was not present in Figure 15. The reason for this increase is not known yet, but the reason for the decreased wavelength is due to the equilibrium diameter being inversely proportional to the magnetic field level. The decrease in beam diameter has two effects: First, the

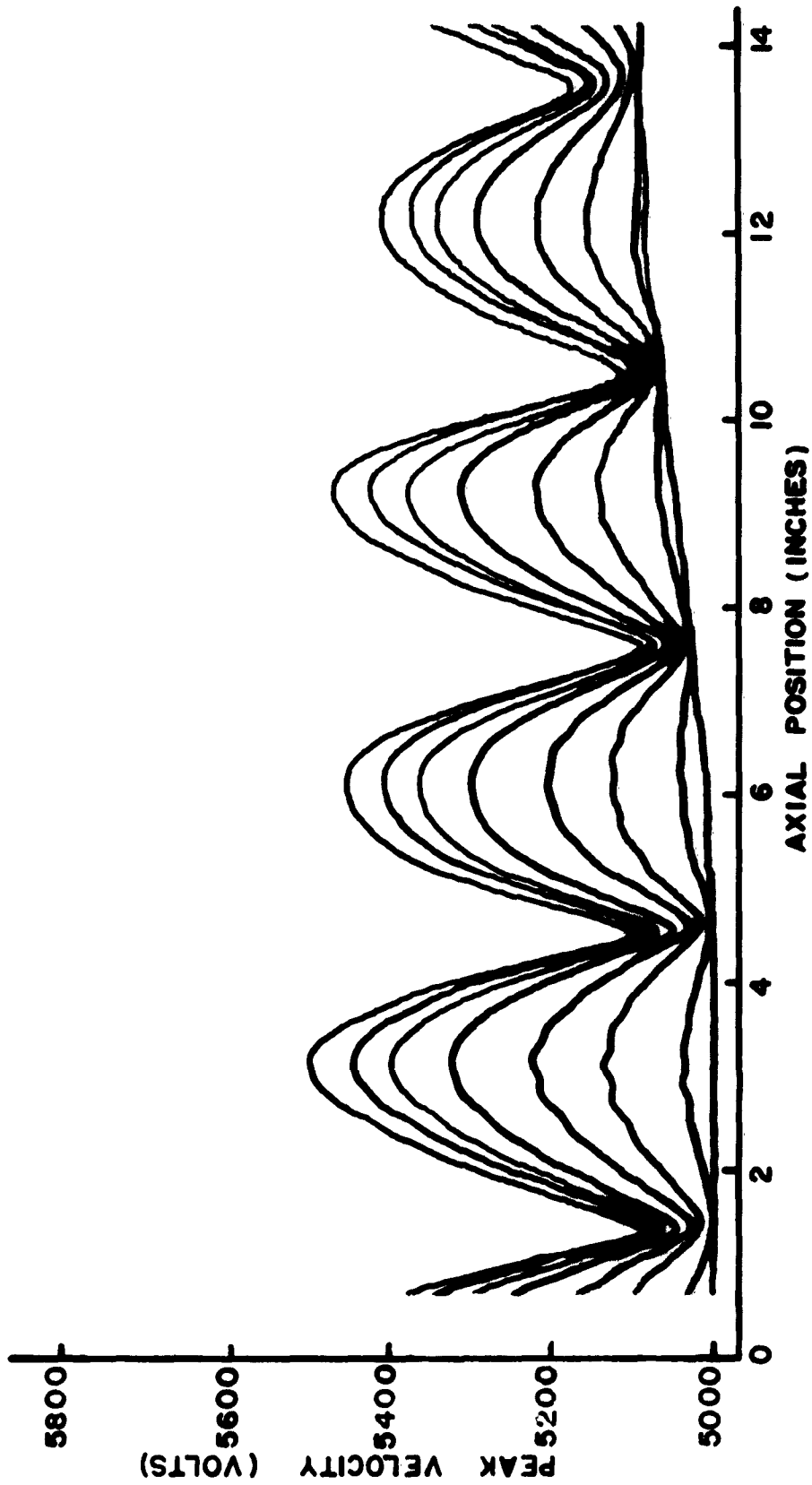


Figure 15. Peak Beam Velocity as Function of Axial Position and of R-F Drive Level for a Magnetic Field 25 Per Cent Greater than Brillouin Value. (Forward powers into input cavity same as for curves in Figure 11.)

charge density increases as the square of the beam diameter, and this in turn causes the plasma frequency to increase linearly with the magnetic field since

$$\omega_p^2 = \frac{\eta \rho_0}{\epsilon_0}$$

Second, the plasma reduction factor decreases as the beam diameter decreases, and this in turn causes the reduced plasma frequency to decrease. However, Figure 4a shows that this decrease varies as $(\gamma r_b)^a$, where $0 < a < 1$. The over-all result is that the reduced plasma wavelength decreases as the magnetic field increases.

A plot of reduced plasma half-wavelength as a function of the magnetic field is shown in Figure 16. The slope of the line fitting most of the data points is -0.45 . However, at 200 gauss, the slope changes to -1

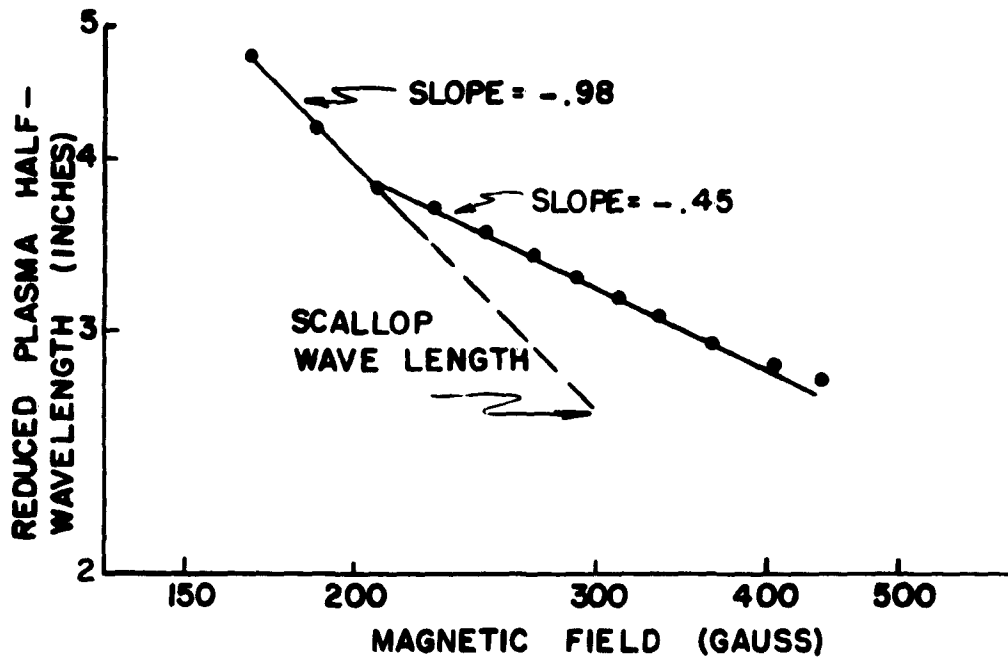


Figure 16. Plot Showing Locking of Plasma Oscillation onto D-C Scalloping of Beam.

and the reduced plasma half-wavelength becomes equal to the scallop wavelength. The explanation for this must be that the periodic d-c electric field, which is caused by the d-c scalloping of the beam, forces the regions of high electron density resulting from the velocity modulation to move into the regions of low density on the scalloping beam. This action is similar to the pulling of the frequency of an oscillator by a resonant circuit, where the reduced plasma frequency corresponds to the oscillator frequency and the d-c scalloping beam corresponds to the resonant circuit.

Plots of the beam velocity as a function of axial position and of drive power for magnetic fields 25 per cent and 35 per cent below the Brillouin value are shown in Figures 17 and 18. The effect of the d-c beam minima on the velocity curves in Figure 17 is to depress the right-hand side of each half sinusoid. In Figure 18, where the reduced plasma half-wavelength is shown equal to the scallop wavelength, the right-hand sides of some of the half sinusoids are actually depressed to the minima of the velocity standing wave by the d-c beam minima.

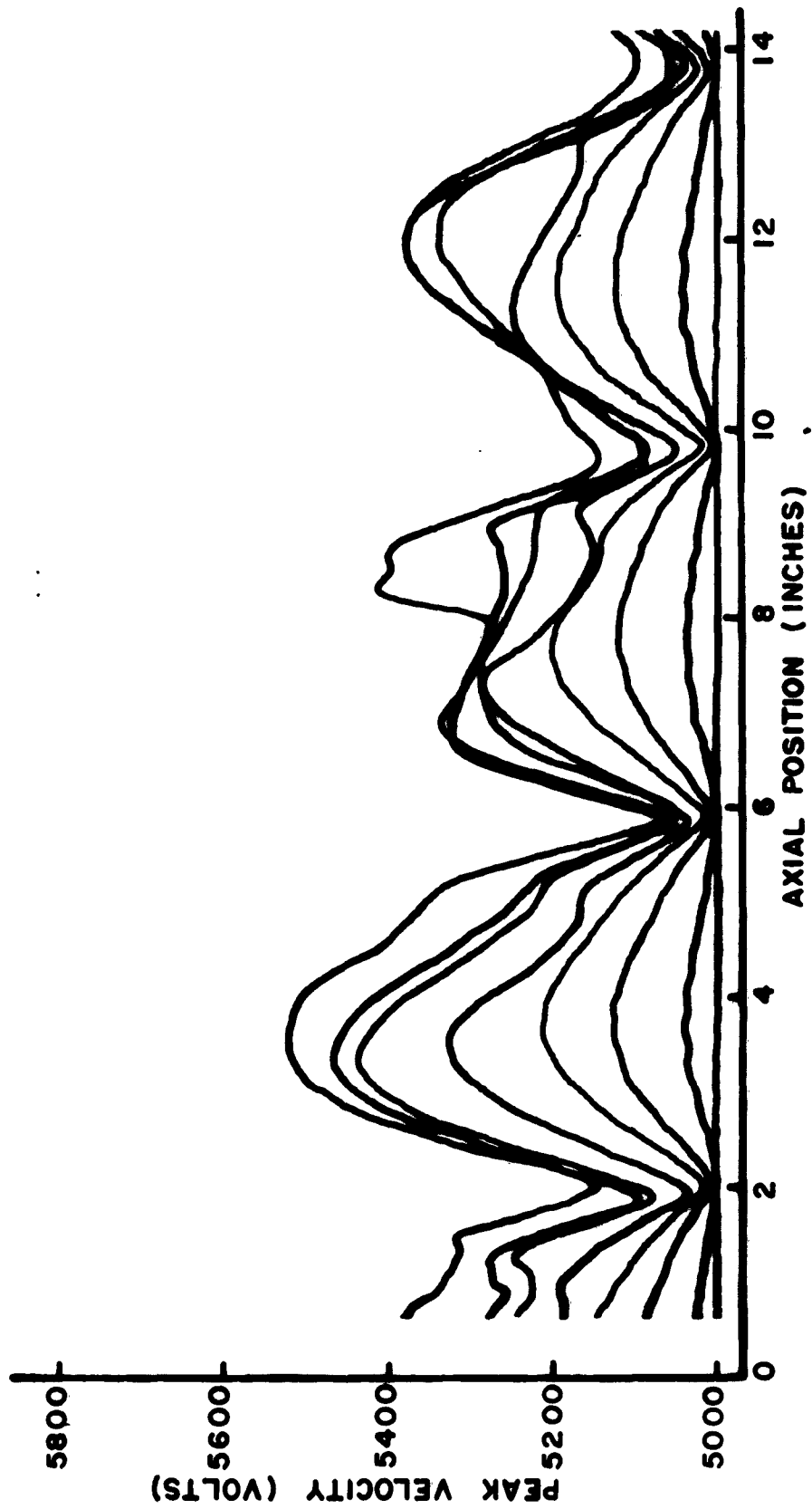


Figure 17. Peak Beam Velocity as Function of Axial Position and of R-F Drive Level for Magnetic Field 25 Per Cent Lower than the Brillouin Value. (Forward powers into input cavity same as for curves in Figure 11.)

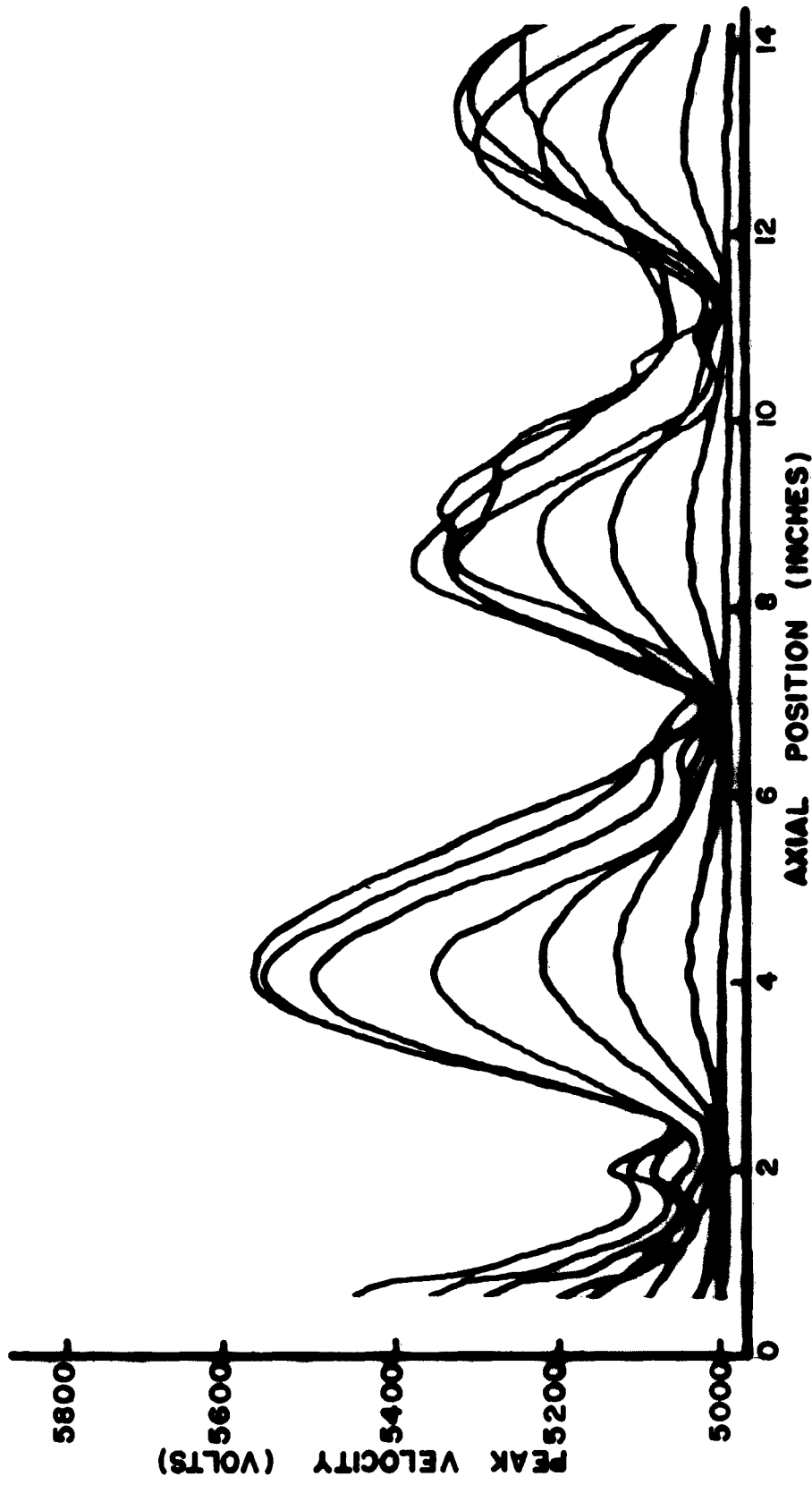


Figure 18. Peak Beam Velocity as Function of Axial Position and of R-F Drive Level for Magnetic Field 35 Per Cent Lower than the Brillouin Value. (Forward powers into input cavity same as for curves in Figure 11.)

IV. CONCLUSIONS AND RECOMMENDATIONS

In order to carry out the velocity modulation study described in this report, a gridless gap cavity was placed in the beam tester described in Research Report EE 495. Since the change in the beam diameter was only a few per cent at drive levels as high as $a = .30$, it was concluded that confined-flow theory should describe the behavior of the modulated beam. Indeed, after carefully accounting for the higher-ranking waves and the manner in which they were launched in the modulation region, it was found that the higher-ranking waves were responsible for the slight decrease in the maxima of small-signal velocity standing waves as a function of distance. It was also found that the presence of these waves was the reason for the minima of the velocity standing-wave pattern not reaching the d-c beam level. As the drive level was increased, it was found that the maxima of the velocity standing-wave pattern decreased more and more rapidly. It is recommended that at least a second-order theory be worked out using the method outlined at the beginning of Section II to find the explanation for this behavior.

Since linear beam tubes normally operate at a magnetic field level high enough that a considerable amount of scalloping is produced on the beam, velocity standing-wave data were taken under these conditions. The resulting small-signal standing-wave patterns were found to resemble the ones obtained under Brillouin flow conditions closely, the main difference being the shortening of the reduced plasma wavelength, which resulted from the reduction in beam diameter. The predictions of the confined-flow theory therefore apply in this case as long as the proper

beam diameter is used. At large-signal levels the maxima of the velocity standing waves were found to be much smaller than those for the Brillouin flow case and again, a second- or higher-order theory is needed to explain the results.

Velocity data were also taken for magnetic field below the Brillouin level, and these indicated a great deal of interference of the d-c beam scallops on the shape of the velocity standing-wave pattern. In fact, under certain conditions it was found that the reduced plasma oscillation locked onto the d-c scalloping of the beam. This phenomena should be thoroughly investigated since it is possible that, with the proper axial positioning of the cavity relative to the d-c scallops on the beam, this locking will occur at magnetic field levels above that for Brillouin flow. If the locking happened to be a function of the amplitude of the modulating signal, the reduced plasma wavelength could shift from λ_q to λ_s (scallop wavelength) at a particular input power level to a klystron and this would result in a shift in the output power level of the klystron.

APPENDIX : DESCRIPTION OF INPUT CAVITY

The input cavity used on the beam tester to modulate the velocity of the electron beam is shown in Figure A-1. The frequency of resonance of the cavity could be varied from 1928 Mc/s to 1958 Mc/s by moving the plunger shown at the left side of the cavity (the plunger was taken from a Varian VA-87 klystron which was designed to operate near 3000 Mc/s). The Q_0 of the cavity was 3000 and the input coupling could easily be varied by changing the size of the coupling loop which was held in place by two 0-80 screws.

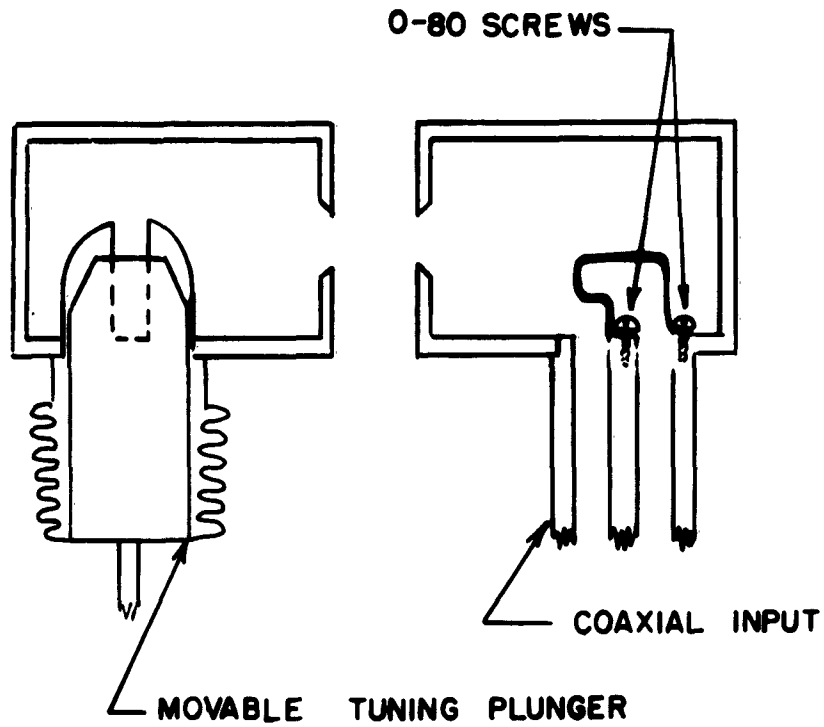


Figure A-1. Input Cavity.

Since the dimensions of the gap were small compared to the free-space wavelength of the signal in the cavity, it was decided that the electric field pattern in the cavity drift tube could be determined by electrolytic tank measurements. The results of these measurements are shown in Figure A-2. In addition, a dashed curve is shown which very nearly approximates the average of the axial electric field plots which were taken at four radii within the beam region. The equation of the dashed curve is

$$E_c = -a \frac{V_1}{d} \cos^2 17.56 z \quad ; \quad (\text{A. 1})$$

or, when the $z = 0$ position is considered to be at the first zero of the cosine squared function, the equation is

$$E_c = -\frac{aV_1}{2d} (1 - \cos \beta_c z) \quad , \quad (\text{A. 2})$$

where $\beta_c = 345$ in mks units. Since the integral of E_c from $\beta_c z = 0$ to $\beta_c z = \pi$ must be the peak voltage V_1 , it must be true that

$$a = \frac{\beta_c d}{\pi} \quad ,$$

so

$$E_c = -\frac{\beta_c V_1}{2\pi} (1 - \cos \beta_c z) \quad . \quad (\text{A. 3})$$

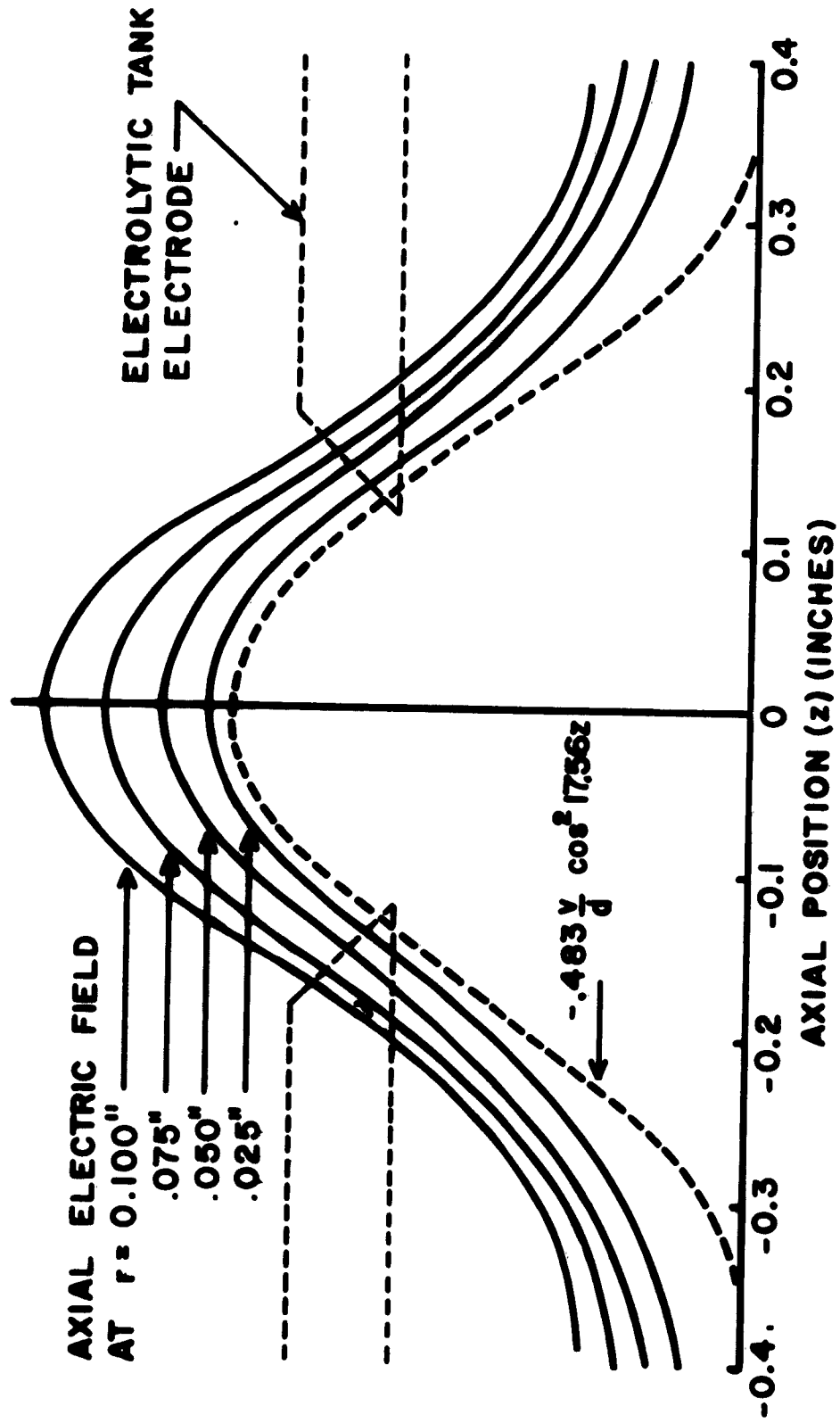


Figure A-2. Axial Electric Fields at Four Radii in Cavity Drift Tube Region as Determined by Electrolytic Tank Measurements.

REFERENCES

1. T. G. Mihran, "The Effect of Space Charge on Bunching in a Two-Cavity Klystron," Proc. I. R. E., ED-6 (1959), pp. 54-64.
2. A. L. Cullen and I. M. Stephenson, "An Experimental Investigation of Velocity-Modulated Electron Beams," I. E. E., 105 (May 1958), Part B Supplement International Convention on Microwave Valves.
3. D. K. Winslow, "The Current Distribution in Magnetically Focused Modulated Electron Beams," Rep. No. 380, Stanford University Microwave Laboratory, Stanford, Calif., April 1957.
4. C. C. Wang, "Electron Beams in Axially Symmetrical Electric and Magnetic Fields," Proc. I. R. E., 38 (1950), pp. 135-147.
5. W. J. Kleen, Electronics of Microwave Tubes, New York: Academic Press, 1958.
6. T. W. Johnson, "Nonlaminar-Flow in Magnetically Focused Electron Beams from Magnetically Shielded Guns," (Letter) J. Appl. Phys., 30 (1959), pp. 1456-1457.
7. S. Ramo, "The Electronic-Wave Theory of Velocity-Modulation Tubes," Proc. I. R. E., 27 (1939), pp. 757-763.
8. P. M. Morse and H. Feshbach, "Methods of Theoretical Physics," New York: McGraw-Hill (1953), p. 206.
9. R. P. Agnew, Differential Equations, 2nd ed., New York: McGraw-Hill, (1960), p. 284.
10. D. A. Watkins, "Traveling-Wave Tube Noise Figure," Proc. I. R. E., 40 (1952), p. 65.

11. G. M. Branch and T. G. Mihran, "Plasma Frequency Reduction Factors in Electron Beams," Proc. I.R.E., ED-2 (1955), p. 3.
12. W. C. Hahn, "Small Signal Theory of Velocity-Modulated Electron Beams," Gen. Elec. Rev., 42 (1939), p. 258.
13. C. C. Wang and P. R. McIsaac, "A Fundamental Formulation of Interaction Equations in Electronic Waveguides," MRI Symposium Proceedings, 8 (1958), New York: Polytechnic Press, p. 295.
14. I. S. and E. S. Sokolnikoff, "Higher Mathematics for Engineers and Physicists," New York: McGraw-Hill, (1941), p. 295.
15. Eugene Jahnke and Fritz Emde, "Table of Functions," New York: Dover Publications, (1945), p. 143.
16. A. H. W. Beck, "Space-Charge Waves and Slow Electromagnetic Waves," New York: Pergamon, (1958),

NONLINEAR SPACE-CHARGE-WAVE ANALYSIS

P. R. McIsaac

School of Electrical Engineering
CORNELL UNIVERSITY
Ithaca, New York

RESEARCH REPORT EE 513

NONLINEAR SPACE CHARGE WAVE ANALYSIS

P. R. Molsaas

LINEAR BEAM MICROWAVE TUBES

Technical Report No. 17

15 September 1961

Published under Contract No. AF30(602)-1696
Rome Air Development Center, Griffiss Air Force Base New York

CONTENTS

	Page
ABSTRACT	v
I. INTRODUCTION	1
1.1 Objectives	1
1.2 Model	3
1.3 Summary of Problems to be Treated	5
II. FORMULATION OF THE GENERAL PROBLEM	6
2.1 Drift Region	6
2.2 Gap Region	10
III. SOLUTION OF THE GENERAL PROBLEM	16
3.1 Drift Region	16
3.2 Gap Region	17
3.3 Combined Input Gap and Drift Region	19
3.4 Ideal Gap and Drift Region	21
3.5 Multiple Gap and Drift Regions	24
3.6 Discussion	32
IV. POWER EXCHANGE	36
4.1 Poynting's Theorem	36
4.2 Formulation for the Gap	37
4.3 Power Exchange in an Ideal Gap	44
V. INPUT GAP AND DRIFT REGION WITH CONTINUOUS-WAVE DRIVE	46
5.1 Exact Solution	46

	Page
5.2 Ideal Gap, First-Order Approximation	48
5.3 Ideal Gap, Second-Order Approximation	57
5.4 Nonideal Gap	66
5.5 The Input Gap and Beam Loading	79
VI. MULTIPLE GAP AND DRIFT REGIONS WITH CONTINUOUS WAVE DRIVE	86
6.1 Exact Solution	86
6.2 Two-Gap Case	90
VII. CONCLUSIONS AND RECOMMENDATIONS	98
APPENDIX A: GLOSSARY	103
APPENDIX B: STRUCTURE TO PROVIDE MAGNETIC WALL	107
APPENDIX C: INVERSION OF CERTAIN TRIGONOMETRIC RELATIONS	111
REFERENCES	119

ABSTRACT

A theory based on an idealized model and including space charge explicitly is developed for the nonlinear behavior of an electron beam passing through alternate gap and drift regions, the gap regions having excitation fields. The model assumes a univelocity cylindrical electron beam confined by a strong axial magnetic field and neutralized by stationary positive ions. In the drift region, the beam is bounded by a magnetic wall, and the solutions of interest are those with no transverse variations. An exact solution, valid below the electron overtaking point, is found in the T_1, T_0 co-ordinates for arbitrary excitation signals. Approximate solutions suitable for numerical calculations, are found for a variety of special cases with continuous-wave excitation in the Z, T co-ordinates. Among the parameters varied are space charge, gap length, and drift length, as well as excitation level. The influence of these on the generation of harmonic frequencies in the beam current, on phase delay, gap transit angle, and beam loading are investigated. The interchange of power in the gap regions between the beam and external circuits is considered, and the power output for a two-gap klystron is obtained.

I. INTRODUCTION

1.1 Objectives

When the input drive level of microwave amplifier tubes is raised sufficiently high relative to the d-c beam power, the interaction process between the electron beam and the associated electromagnetic fields becomes nonlinear. This nonlinearity results in effects which may influence the performance of the tube or change the characteristics to an appreciable degree. For example, the saturation of the gain and power output is, of course, a direct consequence of the nonlinearity, and this determines the efficiency attainable. Among the other effects that may be of importance are the generation of harmonics, the variation of phase shift with drive level, and the influence of the drive level on the pulse response of the tube.

The object of this report is to present the results of a study of certain of the characteristics of a particular class of microwave tubes, velocity-modulated tubes of the klystron type, when operating in the nonlinear region. The study is not exhaustive and only a few of the many possible cases that might be considered have been treated here. The emphasis here will be placed primarily on obtaining an understanding of the physical basis for the phenomena studied. Although the basic problem is formulated and the solution obtained without any restriction placed on the frequency spectrum of the drive signal, most of the analysis and discussion is limited to the case of a continuous-wave (CW) drive signal. Understanding of this case is basic to the consideration of any more complicated drive frequency spectrum (the more complex frequency spectra may be considered in future reports). Particular attention is devoted here to the two main aspects of

the theory of velocity-modulated tubes, both of which are necessary for a complete picture of the operation under either linear or nonlinear conditions. These are, first, the state of the electron beam (i. e., the current density and velocity) at any location, and second, the exchange of power between the electron beam and its surrounding circuit structure in each gap region.

In order to investigate the nonlinear behavior of a velocity-modulated tube, an idealized model of a tube has been employed. The choice of a model for the analysis of nonlinear effects in microwave tubes must often be a compromise between one which represents an actual tube fairly closely but for which the mathematical analysis is formidable, and one which is highly idealized but for which the mathematical analysis can be formulated and carried to completion. Depending on the aims and scope of a particular investigation, one or the other extreme, or some choice in between, may be appropriate. Here, the choice is of an idealized model so that the desired analysis can be carried to completion. It is recognized at the outset that the results of this analysis cannot be expected to apply directly to an actual klystron. It is believed, however, that this analysis does provide insight into the nonlinear behavior of velocity-modulated tubes, and that one can draw conclusions from it that are valid for application to real klystrons.

There have been, of course, a number of theoretical investigations of the nonlinear behavior of klystrons, some of them based on a ballistic theory,¹⁻⁴ some on an extension of space-charge wave theory,⁵⁻¹¹ and a few using computer techniques to extend the ballistic theory to include space-charge effects.^{12, 13} The present investigation is essentially of the second group, taking into account explicitly the influence of space charge, but ignoring the discrete nature of the charges comprising the electron beam by considering it to be a fluid. This approach limits the

application of the analysis to conditions where electron overtaking has not occurred. This choice is made so that the influence of the space charge on the nonlinear behavior can be evaluated while keeping the mathematical analysis tractable. The theory applies, therefore, only to operation levels somewhat below saturated power output in conventional klystrons.

1.2 Model

The particular model chosen for the velocity-modulated tube is illustrated schematically in Figure 1.2-1. A uniform, univelocity electron beam is incident at the entrance plane, $z = 0$, moving in the $+z$ direction, and strong d-c magnetic field in the z direction constrains the motion of the electrons to be parallel to the z axis. A uniform distribution of stationary positive ions in the beam is assumed, such as to produce a zero net d-c charge density within the beam. This ensures that with no input drive the electrons will move with constant velocity through the tube, considerably simplifying the analysis. The beam has a circular cross-section and radius r_0 .

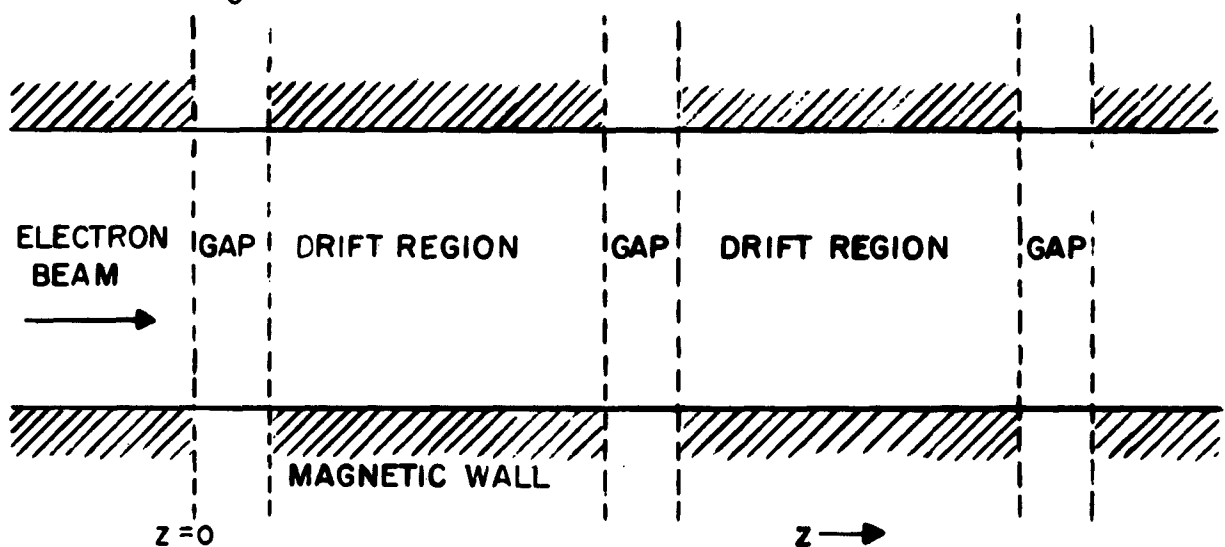


Figure 1.2-1. Schematic of Model for Velocity-modulated Tube.

The tube is divided into gap regions and drift regions by ideal grids transversely oriented to the beam. These ideal grids terminate all electric and magnetic fields while permitting the beam current to pass without interception. At the beam surface, in the drift regions, is located a surrounding "magnetic wall," i. e., a wall which is perfectly inducing ($\mu = \infty$) for a-c fields. In the gap regions there is no such wall, and therefore there is the possibility of energy interchange with the external world.

Only that mode of operation will be considered for which there is no variation of the electron current or longitudinal electric field in the transverse plane. This is commonly provided for by assuming the electron beam to be infinite in cross section, but such an assumption is not necessary and will not be used here. The magnetic wall surrounding the beam in the drift regions ensures a mode with no transverse variations. The impedance looking into a magnetic wall is infinite. Conceptually the magnetic wall may be imagined to be made of perfectly inducing material ($\mu = \infty$). Other circuits can be conceived for which the characteristics are similar. For example, a finned structure of the type discussed in Appendix B and shown in Figure B-1 can be made to approximate a magnetic wall at discrete frequencies.

As a consequence of the presence of the magnetic wall, with its infinite a-c impedance and the lack of variation of the electron current across the beam, there is no transverse a-c magnetic field in the drift regions. In the gap regions, however, where an applied or induced voltage may be present, there will be a transverse a-c magnetic field, and the a-c impedance at the beam edge will be finite.

In addition the higher-order modes or space-charge waves with transverse variations being neglected, the circuit waves that are related to

the wave-guide modes for a circular cylinder with perfectly inducing walls are also neglected. The diameter of the cylinder can always be taken as sufficiently small that all of these wave-guide modes would be evanescent, anyway.

It is recognized that the two assumptions of no transverse electron motion and no transverse electron current variation are severe limitations and that these are not met in any practical klystron. They are believed justified here because they allow the nonlinear analysis to be explored much more fully than would otherwise be the case. Furthermore, it is significant that an actual klystron presumably could be built using a finned structure, which would be operable in this mode with no transverse variations. Thus an experimental verification of the theory could be attempted if this seemed desirable.

1.3 Summary of Problems to be Treated

In Chapter II the general problem of the state of the electron beam for the model chosen is formulated with an arbitrary time variation of the drive signal assumed. In Chapter II, exact solutions are obtained for the general problem posed, and various combinations of gap and drift regions are treated explicitly. Then in Chapter IV the power interchange between the electron beam and the external circuits in the gap regions is discussed.

Although exact solutions are obtained in Chapter III, the form of these is such that they are not suitable for computational use; therefore, considerable attention is directed to obtaining approximate solutions, which are suitable for computation in the important case of a continuous-wave driving signal. Chapter V considers an input gap with a drift region following; Chapter VI considers the multiple gap and drift region case with continuous-wave drive.

II. FORMULATION OF THE GENERAL PROBLEM

2.1 Drift Region

The formulation for the electron charge density, current density, and velocity in the drift regions will be considered first. This is a non-relativistic formulation. Because of the restriction of the motion of the electrons to the longitudinal direction only, and because there is no transverse variation of the current or electric field in the beam, the lack of an induced or driving signal (in the drift regions) means that only the z-directed components of the current density and electric field will exist, all others being zero. The only magnetic field produced by the beam in the drift regions is a d-c azimuthal magnetic field resulting from the d-c electron current. It may be neglected because the confining magnetic field is assumed strong and longitudinal.

The total longitudinal current density, the electron charge density, and the electron velocity are defined as

$$J_T = -J_0 + J(z, t) \quad , \quad (2.1.1)$$

$$\rho_T = -\rho_0 + \rho(z, t) \quad , \quad (2.1.2)$$

$$u_T = u_0 + u(z, t) \quad , \quad (2.1.3)$$

where $-J_0$, $-\rho_0$, and u_0 are those d-c values which exist in the absence of any a-c excitation and are independent of z , the distance along the tube, and t , the time. In general the changes in current density J , charge density, ρ , and velocity resulting from a-c excitation, u , will be functions

of z and t , and may contain a d-c portion. These three parameters are interrelated by

$$J_T = \rho_T u_T \quad ,$$

$$J_0 = \rho_0 u_0 \quad . \quad (2.1.4)$$

The longitudinal electric field is $E(z, t)$ and has no d-c component for zero a-c excitation because of the presence of the stationary positive ions.

For this case of no transverse variations, the relevant Maxwell's equations reduce to

$$J(z, t) + \epsilon \frac{\partial E(z, t)}{\partial t} = 0 \quad , \quad (2.1.5)$$

$$-\rho(z, t) + \epsilon \frac{\partial E}{\partial z}(z, t) = 0 \quad . \quad (2.1.6)$$

The force equation is

$$\frac{du(z, t)}{dt} = -\frac{e}{m} E(z, t) \quad . \quad (2.1.7)$$

Equation (2.1.5) is obtained from the equation relating the curl of the magnetic field to the current density and the time derivative of the current density to the time derivative of the electric field. Only the parameters with excitation present appear, because the original d-c terms are independent of the excitation and may be dropped.

It is convenient to introduce a parameter, z_1 , termed the polarization, which measures the displacement of an electron at a position z, t

in the presence of a-c excitation from the position z_0 , t_0 that it would have with zero a-c excitation. If t_0 is the time that the electron passes the location $z = 0$ with no excitation, then

$$z_1(z, t) = z - z_0 \quad , \quad (2.1.8)$$

$$z_0 = (t - t_0) u_0 \quad . \quad (2.1.9)$$

It is easy to show that¹⁴

$$\frac{J(z, t)}{J_0} = -\frac{1}{u_0} \frac{\partial z_1(z, t)}{\partial t} \quad , \quad (2.1.10)$$

$$\frac{\rho(z, t)}{\rho_0} = \frac{\partial z_1(z, t)}{\partial z} \quad , \quad (2.1.11)$$

$$u(z, t) = \frac{dz_1(z, t)}{dt} \quad . \quad (2.1.12)$$

The total time derivative in Equation (2.1.12) is taken following one particular electron, or at constant t_0 . The electric field can also be expressed in terms of z_1 by using Equations (2.1.5) and (2.1.6):

$$E(z, t) = \frac{\rho_0}{\epsilon} z_1(z, t) \quad . \quad (2.1.13)$$

In order to simplify the form of the equations for later use, all the quantities of interest will be normalized through the introduction of the plasma frequency, ω_p , and its associated phase constant, β_e :

$$\omega_p = \sqrt{\frac{e}{m} \frac{\rho_0}{\epsilon}} \quad , \quad (2.1.14)$$

$$\beta_p = \frac{\omega}{u_0} \quad (2.1.15)$$

The normalized quantities are defined by

$$\begin{aligned} T &= \omega_p t \quad , & Z &= \beta_p z \quad , \\ T_0 &= \omega_p t_0 \quad , & Z_0 &= \beta_p z_0 = T_1 \quad , \\ T_1 &= T - T_0 \quad , & Z_1 &= Z - Z_0 = \beta_p z_1 \quad . \end{aligned} \quad (2.1.16)$$

The electron beam has been assumed to be unmodulated at $Z = 0$.

The basic differential equation for the state of the beam in a drift region, Equation (2.1.7), becomes

$$\frac{d^2 Z_1(Z, T)}{dT^2} + Z_1(Z, T) = 0 \quad , \quad (2.1.17)$$

where the total differentiation is performed at constant T_0 . Implicit in this equation is the assumption that $Z_1(Z, T)$ is a single-valued function. This will be the case if electron overtaking has not occurred; but if electron overtaking has occurred, then $Z_1(Z, T)$ will be multivalued. Attention will be restricted in this report to the region of operation below electron overtaking in order to simplify the problem treated, and this restriction must be kept in mind when applying the results. This limits the theory to levels of operation somewhat below the saturated power output of conventional klystrons.

The general solution to this differential equation in its present

form is difficult to find because the total differentiation is performed with T_0 constant. When the equation is written in terms of partial derivatives with respect to Z and T , a lengthy nonlinear partial differential equation is obtained. Paschke⁵ has obtained an approximate solution to this equation for particular initial conditions by using a method of successive approximations. An exact solution, obtained by changing the variables, will be discussed in Chapter III. Once $Z_1(Z, T)$ is found, the other beam parameters follow directly:

$$\frac{J}{J_0} = - \frac{\partial Z_1(Z, T)}{\partial T} , \quad (2.1.18)$$

$$\frac{\rho}{\rho_0} = \frac{\partial Z_1(Z, T)}{\partial T} , \quad (2.1.19)$$

$$\frac{u}{u_0} = \frac{\partial Z_1(Z, T)}{\partial T} = \frac{\frac{\partial Z_1}{\partial T} + \frac{\partial Z_1}{\partial Z}}{1 - \frac{\partial Z_1}{\partial Z}} . \quad (2.1.20)$$

2.2 Gap Region

The electromagnetic fields in the gap region are somewhat different from those in a drift region because the possibility of power exchange with an external circuit is allowed. The restriction is retained, however, that the current density, charge density, and electron velocity do not vary across the cross section of the beam. Since Equations (2.1.10), (2.1.11) and (2.1.12) relating these quantities to the polarization are valid in the gap region, z_1 will not be a function of transverse position, either.

In addition to the longitudinal electric field, a radial electric field and an azimuthal magnetic field may be present (only the transverse-magnetic fields which do not vary azimuthally are considered). Although there is now no direct connection between the polarization and the longitudinal electric field [Equation (2.1.13) does not apply in a gap region], the longitudinal electric field is taken as independent of transverse position. The relevant Maxwell equations can be written as

$$\frac{\partial E_r}{\partial z} = -\mu \frac{\partial H_\theta}{\partial t} \quad , \quad (2.2.1)$$

$$\frac{\partial E_r}{\partial t} = -\frac{1}{\epsilon} \frac{\partial H_\theta}{\partial z} \quad , \quad (2.2.2)$$

$$J + \epsilon \frac{\partial E_z}{\partial t} = \frac{1}{r} \frac{\partial}{\partial r} (rH_\theta) \quad , \quad (2.2.3)$$

$$\frac{1}{r} \frac{\partial}{\partial r} (rE_r) + \frac{\partial E_z}{\partial z} = \frac{\rho}{\epsilon} \quad (2.2.4)$$

Here J and E_z are functions of z and t only, while E_r and H_θ are functions of r , z , and t . With this restriction, Equation (2.2.3) can be integrated to give

$$H_\theta = \left(J + \epsilon \frac{\partial E_z}{\partial t} \right) \frac{r}{2} + \frac{f(z, t)}{r} \quad . \quad (2.2.5)$$

For H_θ to remain bounded at $r = 0$, $f(z, t) = 0$,

$$H_\theta = \left(J + \epsilon \frac{\partial E_z}{\partial t} \right) \frac{r}{2} \quad . \quad (2.2.6)$$

By combining Equations (2.2.1) and (2.2.2) to eliminate E_r , the following wave equation for H_θ is obtained:

$$\frac{\partial^2 H_\theta}{\partial z^2} - \mu \epsilon \frac{\partial^2 H_\theta}{\partial t^2} = 0 \quad (2.2.7)$$

At this point it is convenient to divide E_z arbitrarily into two terms:

$$E_z = \frac{\rho_0}{\epsilon} z_1 + E_a \quad (2.2.8)$$

This defines the partial longitudinal electric field, E_a . Substituting this into Equation (2.2.6) and using Equation (2.2.10) gives

$$H_\theta = \frac{\epsilon r}{z} \frac{\partial E_a}{\partial t} \quad (2.2.9)$$

Since $\rho_0/\epsilon z_1$ is the electric field produced by the a-c space-charge density, Equation (2.2.9) states that the magnetic field is related to that portion of the electric field in the gap region that is not produced by space charge. Using this result in Equation (2.2.7) gives

$$\frac{\partial}{\partial t} \left(\frac{\partial^2 E_a}{\partial z^2} - \mu \epsilon \frac{\partial^2 E_a}{\partial t^2} \right) = 0 \quad (2.2.10)$$

This has solutions of the form,

$$E_a = f(t - \sqrt{\mu \epsilon} z) + g(t + \sqrt{\mu \epsilon} z) \quad (2.2.11)$$

Thus E_a is made up of waves moving in the plus and minus z direction through the gap region at the velocity of light, $c = 1/\sqrt{\mu \epsilon}$.

These traveling waves will combine to form standing waves. If the gap length is short compared to the free-space wavelength of the highest frequency component of the excitation, then at any one instant of time, the variation of E_a with z will be negligible. That is, for sufficiently short gaps, E_a will be independent of z and a function of t only. The usual d-c transit angle of a gap is appreciably less than π radians and this implies a ratio of gap length to free-space wavelength appreciably less than $\frac{1}{2}(u_0/c)$. Thus, for all klystrons except those of highest voltage, it will be a reasonable approximation to take E_a as independent of z (at least for the fundamental frequency and perhaps the lowest harmonics). From Equations (2.2.2) and (2.2.9), E_r is proportional to $\partial E_z / \partial z$; assuming E_a to be independent of z means that E_r will be zero in the gap region.

Although it is clear that $\rho_0 / \epsilon z_1$ is the electric field resulting from the space charge, the interpretation of E_a remains to be investigated. Introducing the scalar and vector potentials, ϕ and A , gives

$$E_z = -\frac{\partial \phi}{\partial z} - \frac{\partial A_z}{\partial t} \quad (2.2.12)$$

Note that ϕ and A_z can be functions of z and t only. A_z is related to the current by

$$\frac{\partial^2 A_z}{\partial z^2} - \mu \epsilon \frac{\partial^2 A_z}{\partial t^2} = -\mu J = \mu \rho_0 \frac{\partial z_1}{\partial t} \quad (2.2.13)$$

If the gap is so short that z_1 does not vary significantly across it at any one instant of time, then in the gap, both z_1 and A_z can be considered

functions of time only. For this circumstance,

$$\frac{\partial A_z}{\partial t} = -\frac{\rho_0}{\epsilon} z_1, \quad (2.2.14)$$

and

$$\frac{\partial \phi}{\partial z} = -E_z - \frac{\partial A_z}{\partial t} = -\frac{\rho_0}{\epsilon} z_1 - E_a + \frac{\rho_0}{\epsilon} z_1 = -E_a. \quad (2.2.15)$$

That is, E_a is related to a voltage applied between the grids and is equal to the ratio of this voltage to the gap length for the short gap. In any case, it is clear that E_a is related to the fields which are present in the gap region as a result of applied or induced fields in the external circuit coupled to the gap, and E_a measures the degree of coupling.

In the formulation of the equation of motion in the gap, the only difference from the drift region case is the additional electric field, E_a . It will be assumed that the gap is sufficiently short that E_a can be taken as a function of time only. If d is the gap length, and $V_0 = \frac{1}{2} m u_0^2 / e$ the d-c beam voltage, a normalized excitation parameter can be defined as

$$\theta(t) = \frac{E_a(t)}{V_0/d}. \quad (2.2.16)$$

The equation of motion, in normalized form, for the gap region is

$$\frac{d^2 Z_1(Z, T)}{dT^2} + Z_1(Z, T) = -\frac{\theta(T)}{2D}, \quad (2.2.17)$$

where $D = \beta_p d$. Again the restriction to regions of operation before electron overtaking occurs must be observed.

It is seen that if the excitation parameter, $\theta(T)$, is reduced to zero, the equation of motion becomes identical with that for the drift region. The excitation parameter, $\theta(T)$, used here does not have precisely the same definition as the conventional gap excitation parameter, often denoted by α , which is defined as the ratio of the a-c voltage across the gap to the d-c beam voltage. For short gaps $\alpha = \theta(T)$; for long gaps the concept of voltage becomes imprecise and the definition of α is consequently also imprecise.

A comment on the boundary conditions at the grids is in order. At the perfect grids assumed here, the beam quantities are continuous, i. e., the charge density, the current density, and velocity are all continuous (the ideal gap with a double-layer grid is a special case and is treated in Section 3.4). Thus $\partial Z_1/\partial Z$, $\partial Z_1/\partial T$, and dZ_1/dT must be continuous. Therefore Z_1 must also be continuous. Only two conditions are necessary at each grid, and usually the continuity of Z_1 and $\partial Z_1/\partial T$ will be used.

III. SOLUTION OF THE GENERAL PROBLEM

3.1 Drift Region

The general solution for Equation (2.1.17) is sought. As noted above, this equation leads to a lengthy nonlinear partial differential equation if the independent variables, Z , T , are retained. However, in view of the constancy of T_0 during the total differentiation, if new independent variables are chosen, one of them being T_0 , the equation reduces to a linear partial differential equation of particularly simple form. A convenient pair of independent variables is T , T_0 . The equation of motion for an electron passing the $Z = 0$ plane at $T = T_0$ is

$$\frac{\partial^2 Z_1(T, T_0)}{\partial T^2} + Z_1(T, T_0) = 0 \quad (3.1.1)$$

The solution is

$$Z_1(T, T_0) = F(T_0) \cos T + G(T_0) \sin T \quad , \quad (3.1.2)$$

where F and G are functions of T_0 only.

This change of independent variable has made the solution of the differential equation almost trivial, but the difficulty has been shifted elsewhere. Although the solution may be rewritten now in terms of any pair of relevant independent variables, it is, in fact, difficult to express the solution explicitly and concisely in terms of the independent variables of most interest, Z and T . With the relations of Equation (2.2.16),

$$Z_1(Z, T) = F(T - Z + Z_1) \cos T + G(T - Z + Z_1) \sin T \quad , \quad (3.1.3)$$

Z_1 is implicit in functions on the right-hand side.

The interpretation of Equation (3.1.2) or (3.1.3) is clear. If one follows a particular electron (T_0 constant), it will execute a sinusoidal oscillation in the drift region at the plasma frequency, ω_p , about the position it would occupy in the absence of any excitation. This motion is sinusoidal and at the plasma frequency, regardless of the magnitude (at least below electron overtaking) or frequency spectrum of the excitation signal applied to previous gap regions. Changing the excitation can affect only the amplitude or phase of the oscillation, not its frequency. On the other hand, if one observes the combined effects of all the electrons passing a fixed plane as a function of time, then the resultant motion is, in general, nonsinusoidal and rather complex. The excitation in the previous gap regions (which determined F and G) controls the resulting motion.

Because of the implicit nature of Equation (3.1.3), it is not suitable for computation. In Chapters V and VI approximate solutions will be sought which are of more use in computation.

3.2 Gap Region

A general solution is now sought for Equation (2.2.17). This is conveniently done by using Laplace transformation techniques. The first grid of the gap is taken as the $Z = 0$ plane and, as before, T_0 is the time at which a particular electron passes this plane. In general, $Z_1(0, T)$ and $\partial Z_1(0, T)/\partial T$ will not be zero because of possible excitation in prior gaps. For convenience, the gap is assumed to be followed by a long drift region. This allows the easy application of the Laplace transform, but does not actually influence the state of the beam in the gap.

Again, the introduction of new independent variables will transform the differential equation into a linear partial differential equation. The most convenient variables are T_1, T_0 , where $T_1 = T - T_0$. Note that for constant T_0 , differentiation with respect to T_1 is equivalent to differentiation with respect to T . The differential equation and initial conditions are

$$\frac{\partial^2 Z_1(T_1, T_0)}{\partial T_1^2} + Z_1(T_1, T_0) = - \frac{\theta(T_1 + T_0)}{2D} H(T_1) \quad , \quad (3.2.1)$$

$$Z_1(0, T_0) = F(T_0) \quad , \quad (3.2.2)$$

$$\frac{\partial Z_1}{\partial T_1}(0, T_0) = G(T_0) \quad , \quad (3.2.3)$$

$$H(T_1) = \begin{cases} 1 & 0 < T_1 < \Gamma \\ 0 & T_1 < 0, \quad T_1 > \Gamma \end{cases} ; \quad (3.2.4)$$

where Γ is the value of T_1 at which the electron which entered the gap at $T_1 = 0$ (i. e., $T = T_0$), reaches $Z = D$, the end of the gap; $H(T_1)$ ensures that the equation of motion reflects the fact that an electron experiences the excitation $\theta(T_1 + T_0)$ only during the time it is in the gap and not in the drift region.

Let the Laplace transform of $Z_1(T_1, T_0)$ be $Z(s, T_0)$ and that of $\theta(T_1 + T_0)$ be $\Theta(s, T_0)$. Taking the Laplace transform of Equation (3.2.1) and solving for $Z(s, T_0)$ give

$$Z(s, T_0) = - \frac{1}{2D(s^2 + 1)} \left[\Theta(s, T_0) - e^{-s\Gamma} \Theta(s, T_0 + \Gamma) \right] + \frac{sF(T_0) + G(T_0)}{s^2 + 1} \quad (3.2.4)$$

In the gap region, $0 < T_1 < \Gamma$, the inverse transform is

$$Z_1(T_1, T_0) = - \frac{1}{2D} \int_0^{T_1} \theta(\tau + T_0) \sin(T_1 - \tau) d\tau + F(T_0) \cos T_1 + G(T_0) \sin T_1 \quad (3.2.5)$$

The interpretation of this equation is that the first term, the integral, represents the forced motion of the electron resulting from the applied or induced electric field in the gap. The last two terms are a sinusoidal oscillation at the plasma frequency excited by any modulation on the beam as it enters the gap region. It should be kept in mind that if power is not applied to the gap region externally, $\theta(T)$ will, in general, not be zero. The fields induced in the gap region by the modulation present on the beam as it enters the gap will produce a $\theta(T)$.

3.3 Combined Input Gap and Drift Region

The Laplace transform method applied to the gap solution in the previous section is a convenient method to use in obtaining solutions for combinations of gap and drift regions. This section will apply this method to an input gap followed by a drift region. In this case, $Z = 0$ is the plane of the first grid of the input gap, and the beam enters unmodulated at this point; thus $F(T_0) = G(T_0) = 0$.

The expression for the state of the beam in the gap can now be

written directly from Equation (3.2.5). For $0 < T_1 < \Gamma$,

$$Z_1(T_1, T_0) = -\frac{1}{2D} \int_0^{T_1} \theta(\tau + T_0) \sin(T_1 - \tau) d\tau \quad , \quad (3.3.1)$$

where Γ is the value of T_1 at which the electron reaches the end of the gap, $Z = D$; Γ may be determined from the fact that at $Z = D$, the quantity $T_1 = \Gamma$. Since $Z = Z_0 + Z_1$ and $Z_0 = T_1$ [see Equations (2.1.16)],

$$D = Z_0 + Z_1(\Gamma, T_0) \quad ,$$

$$D = \Gamma - \frac{1}{2D} \int_0^{\Gamma} \theta(\tau + T_0) \sin(\Gamma - \tau) d\tau \quad . \quad (3.3.2)$$

The solution of this integral equation will give Γ as a function of T_0 for any excitation function $\theta(T)$. Physically, Γ is the normalized transit time in the gap.

The expression for the state of the beam in the drift region is obtained by writing the inverse Laplace transform of Equation (3.2.4) (with $F = G = 0$) for $T_1 > \Gamma$:

$$Z_1(T_1, T_0) = \frac{1}{2D} \int_0^{\Gamma} \theta(\tau + T_0) \sin(T_1 - \tau) d\tau \quad . \quad (3.3.3)$$

Although quite different in form, this must be equivalent to an expression of the type given in Equation (3.1.2).

Equation (3.3.1) for the state of the beam, the equation for the input gap, and Equation (3.3.3) for the drift region together with the auxiliary relation (3.3.2), are given in terms of the T_1 , T_0 variables. These relations can be expressed in terms of the Z , T variables by replacing T_0 by $T - Z + Z_1$ and T_1 by $Z - Z_1$. The expressions will not be rewritten here in this form because they are clearly implicit relations, with Z_1 appearing on the right-hand side and cannot be easily exploited further with $\theta(T)$ allowed a general time variation. In Chapters V and VI, where sinusoidal excitation functions are considered, the analysis is extended much further, and useful expressions are obtained with Z and T as the variables.

3.4 Ideal Gap and Drift Region

There is a limiting case of the input gap and drift region combination treated in the previous section which permits a significant simplification. This is the case of an "ideal" gap, where D approaches zero so that $\theta(T)$ does not vary during an electron's transit through the gap. Now only the region $T_1 > \Gamma$ is of interest as Γ approaches zero. For small D (and hence small Γ), Equation (3.3.3) is

$$Z_1(T_1, T_0) \cong - \frac{\Gamma}{2D} \theta(T_0) \sin T_1 \quad (3.4.1)$$

The limit of Γ/D as D approaches zero must be determined. Equation (3.3.2) becomes

$$D \cong \Gamma - \frac{\Gamma^2}{4D} \theta(T_0) \quad (3.4.2)$$

to second order in Γ . Solving for Γ gives

$$\Gamma = \frac{2D}{\theta(T_0)} [1 \pm \sqrt{1 - \theta(T_0)}] \quad (3.4.3)$$

The negative sign must be chosen since Γ must approach D as $\theta(T_0)$ approaches zero; therefore

$$\Gamma = \frac{2D}{\theta(T_0)} [1 - \sqrt{1 - \theta(T_0)}] \quad (3.4.4)$$

The polarization, Z_1 , for the drift region following an ideal input gap is then,

$$Z_1(T_1, T_0) = -[1 - \sqrt{1 - \theta(T_0)}] \sin T_1 \quad ; \quad (3.4.2)$$

in terms of the Z, T variables,

$$Z_1(Z, T) = -[1 - \sqrt{1 - \theta(T - Z + Z_1)}] \sin(Z - Z_1) \quad . \quad (3.4.6)$$

The condition under which a real gap will approximate an ideal gap is that the electrons' time of transit in the gap is small compared to the characteristic time of variation of the excitation signal associated with the gap. For this condition, the electrons experience an impulse force as they pass through the gap. If the a-c velocity change is not too large compared to the d-c velocity, the criterion is that d/u_0 be small compared to the characteristic time of variation of the gap excitation.

Examination of Equation (3.4.6) shows that Z_1 and $\partial Z_1 / \partial T$ are both zero at $Z = 0$, but that in general $\partial Z_1 / \partial Z$ and dZ_1 / dT are not

zero at $Z = 0$. This means that for an ideal gap with a double-layer grid and while the polarization and current density are continuous through the gap, the charge density and the velocity change discontinuously through the gap. An electron passing through an ideal gap experiences a force which is a delta function of time; this causes an immediate change in the velocity, but not in the position of the electron. The discontinuity in charge density is equal to

$$\frac{\Delta\rho}{\rho_0} = \frac{\partial Z_1(0, T)}{\partial Z} = -\frac{[1 - \sqrt{1 - \theta(T)}]}{\sqrt{1 - \theta(T)}} ; \quad (3.4.7)$$

the discontinuity in velocity is equal to

$$\frac{\Delta u}{u_0} = \frac{dZ_1(0, T)}{dT} = -[1 - \sqrt{1 - \theta(T)}] . \quad (3.4.8)$$

Although there is a discontinuity in velocity, because the a-c current density is zero at the ideal input gap, there can be no time-average power transferred to the beam by an a-c excitation signal. Thus the time-average velocity squared leaving the input gap must be u_0^2 even though the beam is velocity modulated. This is easily seen by considering

$$\frac{1}{T} \int_0^T \frac{u_T^2(T)}{u_0^2} dT = \frac{1}{T} \int_0^T \left(1 + \frac{\Delta u}{u_0}\right)^2 dT = \frac{1}{T} \int_0^T [1 - \theta(T)] dT = 1 - \frac{1}{T} \int_0^T \theta(T) dT . \quad (3.4.9)$$

For any excitation function which has no d-c component, the integral of $\theta(T)$ over a complete period will be zero; therefore the average kinetic

energy leaving the ideal input gap is the same as the d-c kinetic energy entering.

The application of a d-c excitation signal to a gap has been tacitly prohibited in the analysis developed here. In each region, the analysis has considered changes away from an initial d-c state. The application of a d-c field to a gap establishes a new set of d-c values in the following drift region and no provision has been made to take care of this case. In this report, therefore, no cases will be considered where a d-c excitation is applied to a gap.

3.5 Multiple Gap and Drift Regions

The technique for analyzing an input gap and drift region is readily extended to handle any combination of drift regions and gaps following an input gap. Figure 3.5-1 shows schematically a klystron with multiple gaps

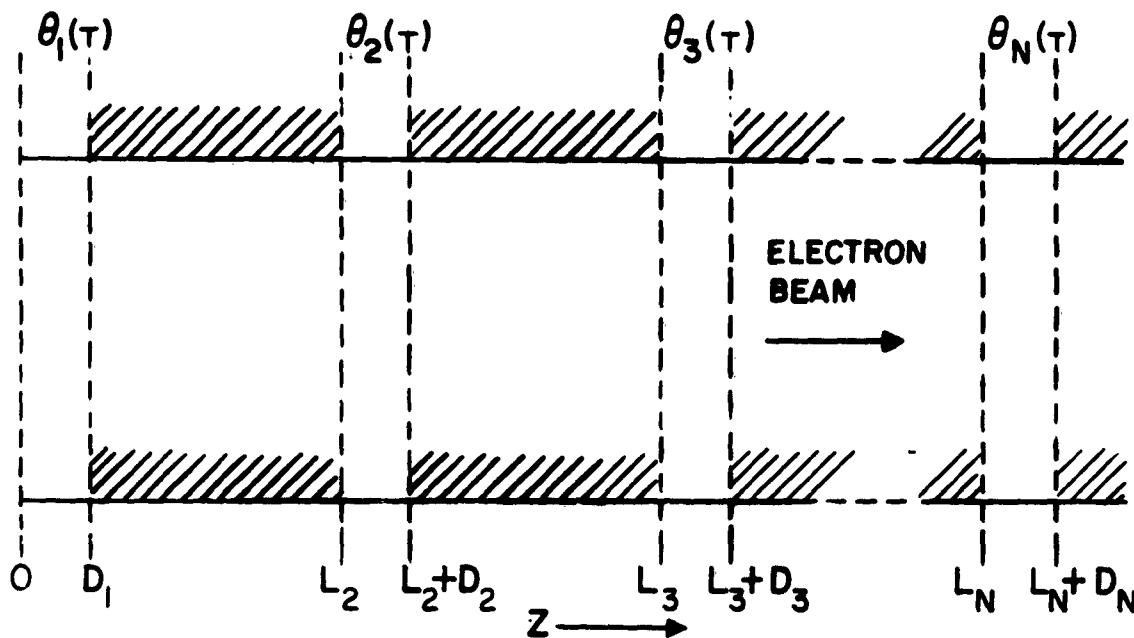


Figure 3.5-1. Schematic of N-Gap Klystron.

and drift regions. The beam enters the first gap at $Z = 0$ unmodulated and experiences a different applied or induced field in each of the gap regions. Again it is convenient to use the T_1, T_0 variables. Let $\lambda_n(T_0)$ equal the value of T_1 at $Z = L_n$, where L_n is the normalized distance from the first grid of the input gap to the first grid of the n^{th} gap. Let $\lambda_n(T_0) + \Gamma_n(T_0)$ equal the value of T_1 at $Z = L_n + D_n$, where D_n is the normalized length of the n^{th} gap. The applied or induced field in the n^{th} gap is $\theta_n(T) = \theta_n(T_1 + T_0)$. Then the equation of motion for an electron passing the $Z = 0$ plane at $T = T_0$ is

$$\frac{\partial^2 Z_1}{\partial T_1^2}(T_1, T_0) + Z_1(T_1, T_0) = -\frac{1}{2} \sum_{n=1}^N \frac{\theta_n(T_1 + T_0) H_n(T_1)}{D_n} \quad (3.5.1)$$

$$Z_1(0, T_0) = \frac{\partial Z_1}{\partial T_1}(0, T_0) = 0 \quad (3.5.2)$$

$$H_n(T_1) = \begin{cases} 1 & \lambda_n < T_1 < \lambda_n + \Gamma_n \\ 0 & T_1 < \lambda_n, \quad T_1 > \lambda_n + \Gamma_n \end{cases} \quad (3.5.3)$$

Again the Laplace transform is used to obtain a solution for a general time variation $\theta_n(T)$. The Laplace transform of Equation (3.5.1) is

$$Z_1(s, T_0) = -\frac{1}{2(s^2 + 1)} \sum_{n=1}^N \frac{\left[\Theta(s, \lambda_n + T_0) e^{-s\lambda_n} - \Theta(s, \lambda_n + \Gamma_n + T_0) e^{-s(\lambda_n + \Gamma_n)} \right]}{D_n} \quad (3.5.4)$$

The solution in the m^{th} gap, that is, $\lambda_m < T_1 < \lambda_m + \Gamma_m$ (or $L_m < Z < L_m + D_m$), is

$$Z_1(T_1, T_0) = -\frac{1}{Z} \sum_{n=1}^{m-1} \frac{1}{D_n} \int_{\lambda_n}^{\lambda_n + \Gamma_n} \theta_n(\tau + T_0) \sin(T_1 - \tau) d\tau$$

$$- \frac{1}{2D_m} \int_{\lambda_m}^{T_1} \theta_m(\tau + T_0) \sin(T_1 - \tau) d\tau \quad . \quad (3.5.5)$$

Within the m^{th} drift region, that is $\lambda_m + \Gamma_m < T_1 < \lambda_{m+1}$ (or $L_m + D_m < Z < L_{m+1}$),

$$Z_1(T_1, T_0) = -\frac{1}{Z} \sum_{n=1}^m \frac{1}{D_n} \int_{\lambda_n}^{\lambda_n + \Gamma_n} \theta_n(\tau + T_0) \sin(T_1 - \tau) d\tau \quad . \quad (3.5.6)$$

The parameters λ_n and Γ_n can be obtained by noting that $\lambda_n = T_1$ for $Z = L_n$, and $\lambda_n + \Gamma_n = T_1$ for $Z = L_n + D_n$. Thus, after recognizing that $\lambda_1 = 0$,

$$D_1 = \Gamma_1 - \frac{1}{2D_1} \int_0^{\Gamma_1} \theta_1(\tau + T_0) \sin(\Gamma_1 - \tau) d\tau \quad ,$$

$$L_2 = \lambda_2 - \frac{1}{2D_1} \int_0^{\Gamma_1} \theta_1(\tau + T_0) \sin(\lambda_2 - \tau) d\tau \quad ,$$

$$\begin{aligned}
L_2 + D_2 &= \lambda_2 + \Gamma_2 - \frac{1}{2D_1} \int_0^{\Gamma_1} \theta_1(\tau + T_0) \sin(\lambda_2 + \Gamma_2 - \tau) d\tau \\
&\quad - \frac{1}{2D_2} \int_{\lambda_2}^{\lambda_2 + \Gamma_2} \theta_2(\tau + T_0) \sin(\lambda_2 + \Gamma_2 - \tau) d\tau \quad , \\
L_m &= \lambda_m - \frac{1}{2} \sum_{n=1}^{m-1} \frac{1}{D_n} \int_{\lambda_n}^{\lambda_n + \Gamma_n} \theta(\tau + T_0) \sin(\lambda_m - \tau) d\tau \quad , \\
L_m + D_m &= \lambda_m + \Gamma_m - \frac{1}{2} \sum_{n=1}^m \frac{1}{D_n} \int_{\lambda_n}^{\lambda_n + \Gamma_n} \theta_n(\tau + T_0) \sin(\lambda_m + \Gamma_m - \tau) d\tau \quad .
\end{aligned}
\tag{3.5.7}$$

By evaluating λ_n and Γ_n for successive gaps, starting from the input gap and proceeding toward the output gap, all these parameters can be obtained from the solutions to the integral equations listed above. The Γ_n are the normalized transit times in the various gaps.

It is clear from both Equations (3.5.5) and (3.5.6) that in any gap or drift region, the excitation in all of the previous gaps contributes toward the net motion. For a klystron amplifier, the state of the beam at any point is influenced by the excitation in the preceding gaps in two ways. First, there are the "feed-through" terms which give the contribution to the beam motion at the point under consideration from each of the preceding gaps. Second, the induced field in each gap has a contribution resulting from the modulation on the beam produced by each of the preceding gaps, so

that the excitation of a gap depends on all of the preceding gaps.

Again a considerable simplification can be achieved in the solutions by considering the limiting case of ideal gaps, for which the D_n approach zero. For this case of zero gap lengths, only the solutions in the drift regions are of interest, and Equation (3.5.6) for the polarization in the m^{th} drift region becomes

$$Z_1(T_1, T_0) = -\frac{1}{2} \sum_{n=1}^m \frac{\Gamma_n}{D_n} \theta_n(T_0 + \lambda_n) \sin(T_1 - \lambda_n) \quad (3.5.8)$$

for $\lambda_m < T_1 < \lambda_{m+1}$. To evaluate the λ_n and Γ_n/D_n , Equations (3.5.7) are investigated for D_n approaching zero:

$$D_1 = \Gamma_1 - \frac{\Gamma_1^2 \theta_1(T_0)}{4D_1}$$

$$L_2 = \lambda_2 - \frac{\Gamma_1}{2D_1} \theta_1(T_0) \sin \lambda_2$$

$$L_2 + D_2 = \lambda_2 + \Gamma_2 - \frac{\Gamma_1}{2D_1} \theta_1(T_0) \left[\sin \lambda_2 - \frac{(\Gamma_1 - 2\Gamma_2)}{2} \cos \lambda_2 - \frac{\Gamma_2^2}{4D_2} \theta_2(T_0 + \lambda_2) \right]$$

$$L_m = \lambda_m - \frac{1}{2} \sum_{n=1}^{m-1} \frac{\Gamma_n}{D_n} \theta_n(T_0 + \lambda_n) \sin(\lambda_m - \lambda_n)$$

$$L_m + D_m = \lambda_m + \Gamma_m - \frac{1}{2} \sum_{n=1}^m \frac{\Gamma_n}{D_n} \theta_n(T_0 + \lambda_n) \left[\sin(\lambda_m - \lambda_n) - \frac{1}{2} (\Gamma_n - 2\Gamma_m) \cos(\lambda_m - \lambda_n) \right] \quad (3.5.9)$$

The formal solutions to these equations are

$$\Gamma_1 = \frac{2D_1}{\theta_1(T_0)} \left[1 - \sqrt{1 - \theta_1(T_0)} \right]$$

$$\lambda_2 = \left[1 - \sqrt{1 - \theta_1(T_0)} \right] \sin \lambda_2 = L_2$$

$$\Gamma_2 = \frac{2D_2}{\theta_2(T_0)} \left\{ 1 - \left[1 - \sqrt{1 - \theta_1(T_0)} \right] \cos \lambda_2 \right.$$

$$\left. - \sqrt{\left\{ 1 - \left[1 - \sqrt{1 - \theta_1(T_0)} \right] \cos \lambda_2 \right\}^2 - \theta_2(T_0 + \lambda_2) + \frac{D_1}{D_2} \frac{\theta_2(T_0 + \lambda_2)}{\theta_1(T_0 + \lambda_2)} \left[1 - \sqrt{1 - \theta_1(T_0)} \right]^2} \right\} \cos \lambda_2$$

$$\lambda_m = \frac{1}{2} \sum_{n=1}^{m-1} \frac{\Gamma_n}{D_n} \theta_n(T_0 + \lambda_n) \sin(\lambda_m - \lambda_n) = L_m$$

$$\Gamma_m = \frac{2D_m}{\theta_m(T_0)} \left\{ 1 - \frac{1}{2} \sum_{n=1}^{m-1} \frac{\Gamma_n}{D_n} \theta_n(T_0 + \lambda_n) \cos(\lambda_m - \lambda_n) \right.$$

$$\left. - \sqrt{\left[1 - \frac{1}{2} \sum_{n=1}^{m-1} \frac{\Gamma_n}{D_n} \theta_n(T_0 + \lambda_n) \cos(\lambda_m - \lambda_n) \right]^2 - \theta_m(T_0 + \lambda_m) + \sum_{n=1}^{m-1} \frac{D_n}{D_m} \frac{\theta_n(T_0 + \lambda_n)}{\theta_n(T_0 + \lambda_n)} - \frac{\Gamma_n^2 \theta_n^2(T_0 + \lambda_n)}{4D_n^2} \cos(\lambda_m - \lambda_n)} \right\}$$

By starting at the input gap and working along the tube, the various parameters can be determined and substituted into the succeeding equations. It is seen that in order to obtain the λ_m , a transcendental equation must be solved. Since Γ_m is proportional to D_m , then Γ_m will approach zero as D_m approaches zero. The ratio of Γ_m to D_m will remain finite, however, and this is the quantity of interest for determining the state of the beam. In the expression for Γ_m , the ratio D_n/D_m occurs. Although each term by itself approaches zero, the ratio will remain finite. If one is considering multicavity klystrons with all gap lengths equal, then D_n/D_m is unity. If some of the gaps have different lengths, then as the gap lengths approach zero, the effect of the different lengths can be evaluated by using the proper ratios for D_n/D_m .

The equation for the polarization in the m^{th} drift region can now be written as

$$\begin{aligned}
 Z_1(T_1, T_0) = & - \sum_{n=1}^m \left(1 - \frac{1}{2} \sum_{l=1}^{n-1} \frac{\Gamma_l}{D_l} \theta_l(T_0 + \lambda_l) \cos(\lambda_n - \lambda_l) \right. \\
 & - \left. \left[1 - \frac{1}{2} \sum_{l=1}^{n-1} \frac{\Gamma_l}{D_l} \theta_l(T_0 + \lambda_l) \cos(\lambda_n - \lambda_l) \right]^2 - \theta_n(T_0 + \lambda_n) \right. \\
 & \left. + \sum_{l=1}^{n-1} \frac{D_l}{D_n} \frac{\theta_n(T_0 + \lambda_n)}{\theta_l(T_0 + \lambda_l)} \frac{\Gamma_l^2 \theta_l^2(T_0 + \lambda_l)}{4D_l^2} \cos(\lambda_n - \lambda_l) \right)^{\frac{1}{2}} \sin(T_1 - \lambda_n) .
 \end{aligned}$$

(3.5.11)

Again, the fact that each previous gap contributes to the polarization is evident, and also that a particular gap excitation is influenced by all the previous gap excitations. Examination of this expression shows that Z_1 and $\partial Z_1/\partial T$ are continuous at each gap, while $\partial Z_1/\partial Z$ and dZ_1/dT are discontinuous. Thus in the general case, the boundary conditions at an ideal gap are that the polarization and current density are continuous but that charge density and velocity change discontinuously. Since there will be a nonzero value of a-c current density at all the gaps except the input gap, energy can be transferred to or from the beam on the average in all gaps except the input gap; therefore, the average kinetic energy of the beam will change discontinuously at each gap, except the input gap.

In the multiple-gap klystron with ideal gaps, one limiting case is of particular interest. It is assumed that $\theta_n(T) \ll 1$. Although this precludes appreciable nonlinearity in the gap regions, there can still be an appreciable nonlinearity in the drift regions (see Section 5.2), if the plasma frequency is small compared to the frequency of the excitation signal. For this case, $\lambda_m \cong L_m$ and $\Gamma_m \cong D_m$. The equation for the polarization in the m^{th} drift region is now

$$Z_1(T_1, T_0) = - \sum_{n=1}^m \frac{\theta_n(T_0 + \lambda_n)}{2} \sin(T_1 - \lambda_n) \quad , \quad (3.5.12)$$

since $\Gamma_m = D_m$,

$$\lambda_m = L_m + \frac{1}{2} \sum_{n=1}^{m-1} \theta_n(T_0 + \lambda_n) \sin(L_m - L_n) \quad , \quad (3.5.13)$$

to the first order in $\theta_n(T_0)$. It is clear that this has produced a marked simplification in the equation for the polarization, and this expression will form the starting point for discussions of the ideal gap in Chapters V and VI.

3.6 Discussion

This chapter has presented the solutions for the polarization of an electron beam in a klystron under nonlinear conditions when the time variation of the driving signals in each gap is arbitrary. It is well to keep clearly in mind the conditions for which these solutions are valid. First, they apply to the model of a klystron described in Section 1.2. Second, it is assumed that the gaps are short compared to the free-space wavelength of any significant driving signal. And third, only operation before electron overtaking has occurred is considered. In addition, only those driving signals are considered which have no d-c component.

The results of this chapter are essentially summarized in Section 3.5, which gives the general results for multiple gaps and drift regions. Within any drift region, the electrons will oscillate at the plasma frequency about the position they would have had in the absence of excitation. The amplitude and phase associated with this oscillation of any particular electron is determined by the excitation it has received in each of the preceding gaps. Within a gap region, in addition to this oscillation at the plasma frequency, an electron undergoes a forced oscillation resulting from the excitation field in that gap.

It is seen that the solutions are somewhat simplified by considering the limiting case of zero gap lengths (ideal gaps). In this case, in each gap

the beam experiences a force in the form of a delta function. Although the current density, charge density, velocity, and polarization are all continuous at a single grid, this is not the case at an ideal gap (double layer grid). Here the polarization and current density are continuous, but the charge density and velocity change discontinuously. Therefore, in general, both the instantaneous and the time average kinetic energy of the beam will change discontinuously through an ideal gap. At an input gap, however, although the instantaneous kinetic energy may change discontinuously, the time-average kinetic energy must be continuous, since there is no a-c current density in the beam at this point. And finally for ideal gaps, the restriction to excitation signals such that $\theta_n(T) \ll 1$, is seen to lead to a very considerable simplification in the expression for the polarization.

All of the solutions which have been obtained in this chapter, for both long and short gaps, have resulted in implicit expressions for the polarization. While they are valuable for providing insight into the behavior of the beam in nonlinear operation, they cannot be used conveniently for computations. Therefore Chapters V and VI will develop approximate solutions (based on those obtained above) for the case of continuous sinusoidal excitation signals which are suitable for computational use.

For reference purposes it is desirable to state here the limiting condition for which electron overtaking occurs. In the T_1, T_0 system this is at

$$\frac{\partial Z_1}{\partial T_0} - \frac{\partial Z_1}{\partial T_1} = 1.0 \quad , \quad (3.6.1)$$

and under this condition the current and charge densities became infinite.

In terms of the general solutions presented in Section 3.5, the limiting condition in the m^{th} gap is

$$\begin{aligned}
& -\frac{1}{Z} \sum_{n=1}^{m-1} \frac{1}{D_n} \left\{ \int_{\lambda_n}^{\lambda_n + \Gamma_n} \left[\frac{\partial \theta_n(\tau + T_0)}{\partial T_0} \sin(T_1 - \tau) - \theta_n(\tau + T_0) \cos(T_1 - \tau) \right] d\tau \right. \\
& \left. + \theta_n(\lambda_n + \Gamma_n + T_0) \sin(T_1 - \lambda_n - \Gamma_n) \frac{\partial(\lambda_n + \Gamma_n)}{\partial T_0} - \theta_n(\lambda_n + T_0) \sin(T_1 - \lambda_n) \frac{\partial \lambda_n}{\partial T_0} \right\} \\
& - \frac{1}{2D_m} \left\{ \int_{\lambda_m}^{T_1} \left[\frac{\partial \theta_m(\tau + T_0)}{\partial T_0} \sin(T_1 - \tau) - \theta_m(\tau + T_0) \cos(T_1 - \tau) \right] d\tau \right. \\
& \left. - \theta_m(\lambda_m + T_0) \sin(T_1 - \lambda_m) \frac{\partial \lambda_m}{\partial T_0} \right\} = 1.0 \quad , \quad (3.6.2)
\end{aligned}$$

and in the m^{th} drift region is

$$\begin{aligned}
& -\frac{1}{Z} \sum_{n=1}^m \frac{1}{D_n} \left\{ \int_{\lambda_n}^{\lambda_n + \Gamma_n} \left[\frac{\partial \theta_n(\tau + T_0)}{\partial T_0} \sin(T_1 - \tau) - \theta_n(\tau + T_0) \cos(T_1 - \tau) \right] d\tau \right. \\
& \left. + \theta_n(\lambda_n + \Gamma_n + T_0) \sin(T_1 - \lambda_n - \Gamma_n) \frac{\partial(\lambda_n + \Gamma_n)}{\partial T_0} - \theta_n(\lambda_n + T_0) \sin(T_1 - \lambda_n) \frac{\partial \lambda_n}{\partial T_0} \right\} = 1.0 \\
& \hspace{20em} (3.6.3)
\end{aligned}$$

For the ideal gap case, the limiting condition in the m^{th} drift region is

$$\begin{aligned}
 & -\frac{1}{2} \sum_{n=1}^m \frac{1}{D_n} \left[\frac{\partial \Gamma_n}{\partial T_0} \theta_n(T_0) \sin(T_1 - \lambda_n) + \Gamma_n \frac{\partial \theta_n(T_0)}{\partial T_0} \sin(T_1 - \lambda_n) \right. \\
 & \left. - \Gamma_n \theta_n(T_0) \frac{\partial \lambda_n}{\partial T_0} \cos(T_1 - \lambda_n) - \Gamma_n \theta_n(T_0) \cos(T_1 - \lambda_n) \right] = 1.0 \quad , \quad (3.6.4)
 \end{aligned}$$

and if $\theta_n(T) \ll 1$,

$$\begin{aligned}
 & -\frac{1}{2} \sum_{n=1}^m \left[\frac{\partial \theta_n(T_0)}{\partial T_0} \sin(T_1 - L_n) - \theta_n(T_0) \frac{\partial \lambda_n}{\partial T_0} \cos(T_1 - \lambda_n) - \theta_n(T_0) \cos(T_1 - \lambda_n) \right] = 1.0 \\
 & \hspace{25em} (3.6.5)
 \end{aligned}$$

IV. POWER EXCHANGE

4.1 Poynting's Theorem

The power exchanged in the gap region with a cavity field which has been induced by the beam current or produced by an externally applied field is of prime interest in the analysis of klystrons. The power exchange between the electron beam with its kinetic energy and the gap field with its electromagnetic power flow is described by Poynting's theorem;¹⁴ therefore, it will first be stated and put in a form convenient for the analysis of power exchange.

In terms of the electric and magnetic fields and the current density, Poynting's theorem states

$$\nabla \cdot (\underline{E} \times \underline{H}) + \frac{\partial}{\partial t} \left(\frac{\epsilon}{2} \underline{E}^2 + \frac{\mu}{2} \underline{H}^2 \right) + \underline{E} \cdot \underline{J}_T = 0 \quad (4.1.1)$$

It is often convenient to express the current density in terms of the velocity and charge density, $\underline{J}_T = \rho_T \underline{u}_T$. When this is done, it can be shown¹⁵ that Equation (4.1.1) can be written as

$$\nabla \cdot \left(\underline{E} \times \underline{H} + \frac{m}{2e} \rho_T \underline{u}_T^3 \right) + \frac{\partial}{\partial t} \left(\frac{\epsilon}{2} \underline{E}^2 + \frac{\mu}{2} \underline{H}^2 + \frac{m}{2e} \rho_T \underline{u}_T^2 \right) = 0 \quad (4.1.2)$$

Integrating over the volume of the gap occupied by the beam, and using Gauss' theorem, gives the two expressions:

$$\int_S (\underline{E} \times \underline{H}) \cdot \underline{n} ds + \int_V \left[\frac{\partial}{\partial t} \left(\frac{\epsilon}{2} \underline{E}^2 + \frac{\mu}{2} \underline{H}^2 \right) + \underline{E} \cdot \underline{J}_T \right] dv = 0 \quad (4.1.3)$$

$$\int_S \left(\underline{\mathbf{E}} \times \underline{\mathbf{H}} + \frac{m}{Ze} \rho_T u_T^3 \right) \cdot \underline{\mathbf{n}} ds + \int_V \frac{\partial}{\partial t} \left(\frac{\epsilon}{2} \underline{\mathbf{E}}^2 + \frac{\mu}{2} \underline{\mathbf{H}}^2 + \frac{m}{Ze} \rho_T u_T^2 \right) dv = 0 \quad (4.1.4)$$

The interpretation to be made then is that $\frac{m}{Ze} \rho_T u_T^2$ represents the kinetic energy density of the beam while $\frac{m}{Ze} \rho_T u_T^3$ represents the kinetic power density which flows through any cross section of the beam.

In many cases, the time average values are of most importance. For the class of excitations which are periodic in time (this class is of considerable practical importance), the time average value of the volume integral in Equation (4.1.4) is zero; thus

$$\overline{\int_S \left(\underline{\mathbf{E}} \times \underline{\mathbf{H}} + \frac{m}{Ze} \rho_T u_T^3 \right) \cdot \underline{\mathbf{n}} ds} = 0 \quad (4.1.5)$$

or

$$\overline{\int_S (\underline{\mathbf{E}} \times \underline{\mathbf{H}}) \cdot \underline{\mathbf{n}} ds} = - \overline{\int_V \underline{\mathbf{E}} \cdot \underline{\mathbf{J}}_T dv} \quad (4.1.6)$$

where the overbar indicates the time average.

4.2 Formulation for the Gap

The formulation of Poynting's theorem in terms of the particular model used in this report will be developed. For the gaps considered here, only \mathbf{E}_z and \mathbf{H}_θ will be present, since the gaps are assumed short compared to the free-space wavelength, and the electromagnetic power flow will be purely radial. When the azimuthal symmetry of the fields is con-

sidered, the radial power flow at any radius r is given by

$$P_r = -2\pi r \int_0^d E_z H_\theta dz \quad (4.2.1)$$

Using the expressions for E_z and H_θ obtained in Section 2.2, and introducing the normalized variables gives

$$\frac{P_r}{P_0} = -\frac{R^2}{R_0^2} \frac{1}{D} \int_0^D \left(Z_1 + \frac{\theta}{2D} \right) \frac{\partial \theta}{\partial T} dZ \quad (4.2.2)$$

Here, $R = \beta_p r$ is the normalized radius of the particular surface considered; $R_0 = \beta_p r_0$ is the normalized beam radius; and P_0 is the original d-c beam power. Usually one is concerned with the total power into or out of the beam and R is taken equal to R_0 . It is clear that Z_1 and θ must be expressed in the Z, T system to evaluate the integral over the gap surface.

The integral has two terms. The term which contains only θ and $\partial \theta / \partial T$ is associated with the stored electric energy in the gap considered as a capacitor and is independent of the state of the beam (except in so far as the state of the beam determines the magnitude of the induced field). Since $\theta(T)$ is independent of Z ,

$$-\frac{1}{D} \int_0^D \frac{\theta}{2D} \frac{\partial \theta}{\partial T} dZ = \frac{1}{4D} \frac{\partial \theta^2}{\partial T} \quad (4.2.3)$$

In terms of the unnormalized variables, this is

$$\frac{-\pi r_0^2}{P_0} \frac{\epsilon}{2} \frac{\partial E_a^2}{\partial t} \quad (4.2.4)$$

This is clearly the rate of change with time of the electric energy stored in the gap by the excitation field, E_a , divided by the original d-c beam power. The main interest therefore, will be directed toward the first term of Equation (4.2.2) for $R = R_0$:

$$- \frac{1}{D} \int_0^D Z_1 \frac{\partial \theta}{\partial T} dZ \quad , \quad (4.2.5)$$

which describes the power interchange with the electron beam. In terms of the normalized variables,

$$\begin{aligned} \frac{1}{P_0} \int_V \underline{E} \cdot \underline{J}_T dv &= 2 \int_0^D \left(Z_1 + \frac{\theta}{2D} \right) \left(1 + \frac{\partial Z_1}{\partial T} \right) dZ \\ &= \theta + 2 \int_0^D Z_1 dZ + \frac{\theta}{D} \int_0^D \frac{\partial Z_1}{\partial T} dZ + \int_0^D \frac{\partial (Z_1)^2}{\partial T} dZ \quad ; \end{aligned} \quad (4.2.6)$$

also,

$$\frac{1}{P_0} \int_s \frac{m}{Ze} \rho_T u_T^3 \cdot \underline{n} ds = \left(1 - \frac{\partial Z_1}{\partial Z} \right) \left(1 + \frac{dZ_1}{dT} \right)^3 \quad , \quad (4.2.7)$$

$$\frac{1}{P_0} \int_V \frac{\partial}{\partial t} \left(\frac{m}{Ze} \rho_T u_T^2 \right) dv = \int_0^D \frac{\partial}{\partial t} \left[\left(1 - \frac{\partial Z_1}{\partial Z} \right) \left(1 + \frac{dZ_1}{dT} \right)^2 \right] dZ \quad . \quad (4.2.8)$$

Since

$$\frac{u}{u_0} = \frac{dZ_1}{dT} = \frac{\frac{\partial Z_1}{\partial T} + \frac{\partial Z_1}{\partial Z}}{1 - \frac{\partial Z_1}{\partial Z}} \quad , \quad (4.2.9)$$

$$\frac{1}{P_0} \int_s \frac{m}{Ze} \rho_T u_T^3 \cdot \underline{n} ds = \frac{\left(1 + \frac{\partial Z_1}{\partial T}\right)^3}{\left(1 - \frac{\partial Z_1}{\partial Z}\right)^2} \quad (4.2.10)$$

$$\frac{1}{P_0} \int_V \frac{\partial}{\partial t} \left(\frac{m}{Ze} \rho_T u_T^2 \right) dv = \int_0^D \frac{\partial}{\partial T} \left[\frac{\left(1 + \frac{\partial Z_1}{\partial T}\right)^2}{\left(1 - \frac{\partial Z_1}{\partial Z}\right)^2} \right] dZ \quad (4.2.11)$$

Both E_z and H_θ must be continuous at the beam edge; thus for a given state of the beam, the values outside the beam are determined for a specific cavity geometry. For the model assumed here, H_θ is independent of z and the E_a portion of E_z is also independent of z . But the portion of E_z related to the space-charge field will in general be a function of z . Thus while the magnetic field in the gap external to the beam must be independent of z , the electric field must be a function of z . And the particular z variation observed will probably be a function of the excitation level. A rough estimate of the relative amplitudes of the two portions of the electric field can be made. It will be seen in Chapter V that within a gap, Z_1 is roughly of the order of $\theta/2D$ divided by the ratio of the excitation frequency to the plasma frequency, or less. Therefore the ratio of the space-charge field to the excitation field will be roughly of the order of the reciprocal of the ratio of excitation frequency to plasma frequency, or smaller. In this report, the greatest attention is directed toward situations where the ratio of excitation to plasma frequency is large (because of the simplification in mathematics that this provides), and therefore the portion of the electric field which varies with Z will be relatively small.

In order to circumvent the necessity of having to consider specific cavity geometries associated with the gaps, an equivalent circuit for the cavity will be developed with the edge of the beam ($r = r_0$) taken as the reference surface. The main requirement for the equivalent circuit is that it predict the same power interchange for a given beam state as the actual circuit. An equivalent current into the equivalent circuit, I_e , and an equivalent voltage across it, V_e , are chosen as

$$I_e = 2\pi r_0 H_\theta(r_0) = \frac{V_0}{D} \eta \frac{\pi R_0^2}{\sqrt{\frac{\mu}{\epsilon}}} \frac{\partial \theta}{\partial T} \quad (4.2.12)$$

$$V_e = -2V_0 \int_0^D \left(z_1 + \frac{\theta}{2D} \right) dz \quad (4.2.13)$$

The power flow into the equivalent circuit, normalized to the original d-c beam power is

$$\frac{P_{ro}}{P_0} = \frac{I_e V_e}{P_0} = -\frac{1}{D} \frac{\partial \theta}{\partial T} \int_0^D \left(z_1 + \frac{\theta}{2D} \right) dz \quad (4.2.14)$$

This is seen to be identical with Equation (4.2.2) for the electromagnetic power flow radially outward from the beam; therefore the equivalent circuit chosen provides the proper power flow.

When the excitation is periodic in time, V_e and I_e can be developed in a Fourier series based on the fundamental excitation and its harmonics. For each frequency, an equivalent circuit impedance can be defined as the ratio of V_e to I_e at the particular frequency:

$$\frac{V_e}{I_e} = -2\sqrt{\frac{\mu}{\epsilon}} \frac{D}{\eta\pi R_o^2} \frac{\int_0^D \left(z_1 + \frac{\theta}{2D}\right) dz}{\frac{\partial\theta}{\partial T}} = -\sqrt{\frac{\mu}{\epsilon}} \frac{D}{\eta\pi R_o^2} \left(\frac{\int_0^D 2z_1 dz}{\frac{\partial\theta}{\partial T}} + \frac{\theta}{\frac{\partial\theta}{\partial T}} \right) \quad (4.2.15)$$

The second term in the expression is clearly reactive in nature. Figure 4.2-1 shows the two equivalent circuits for a cavity that are of interest;

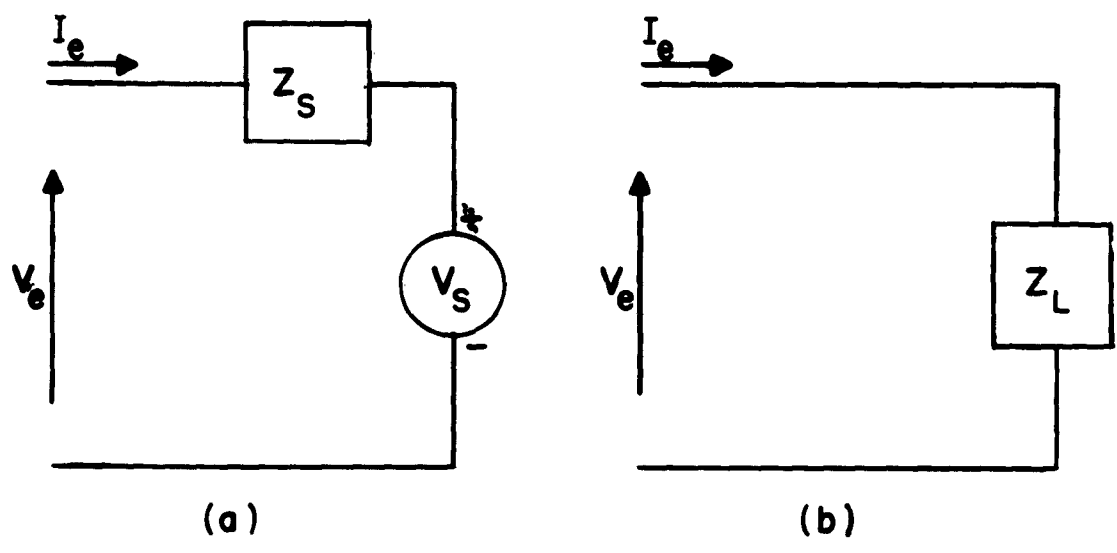


Figure 4.2-1. Equivalent Circuits for Cavities:
 (a) Input Cavity with Signal Source;
 (b) Intermediate or Output Cavity.

the first has a signal source and represents an input cavity, the second represents an intermediate or output cavity. In the first case, one may write

$$V_e = I_e Z_s + V_s \quad (4.2.16)$$

or

$$-2V_0 \int_0^D Z_1 dZ - V_0 \theta = \frac{V_0 \eta}{D} \frac{\pi R_0^2}{\sqrt{\frac{\mu}{\epsilon}}} Z_s \frac{\partial \theta}{\partial T} + V_s \quad (4.2.17)$$

If Z_1 can be expressed in terms of θ , then the second equation can be solved for θ , thus providing a means for determining the excitation parameter θ in terms of a source voltage, V_s . For an input gap, Z_1 is zero at $Z = 0$ and only the value of θ in the gap contributes to Z_1 .

For the case of an intermediate or output cavity,

$$V_e = I_e Z_L \quad , \quad (4.2.18)$$

$$-2V_0 \int_0^D Z_1 dZ - V_0 \theta = \frac{V_0 \eta}{D} \frac{\pi R_0^2}{\sqrt{\frac{\mu}{\epsilon}}} \frac{\partial \theta}{\partial T} Z_L \quad (4.2.19)$$

In this case, Z_1 at the input plane of the gap is nonzero due to modulation of the beam by previous gaps. By expressing Z_1 in terms of the excitation of the gap under consideration plus a contribution from previous gaps excitation, it is possible to solve for the gap excitation in terms of Z_L and the previous gap excitations. Thus this equivalent circuit approach enables a determination to be made of the excitation at each gap without determining in detail the electromagnetic fields in the cavities.

On the other hand, if one looks at the surface of the beam, the impedance seen is that resulting from the gap capacitance plus the beam loading. This impedance is

$$-\frac{V_e}{I_e} = \sqrt{\frac{\mu}{\epsilon}} \frac{D}{\eta\pi R_o^2} \left(\frac{\int_0^D 2Z_1 dz}{\frac{\partial\theta}{\partial T}} + \frac{\theta}{\frac{\partial\theta}{\partial T}} \right), \quad (4.2.20)$$

the first term being the beam loading and the second the gap capacitive reactance. In computing the beam loading, an excitation is applied only to the particular gap under consideration, so each gap is considered as an input gap in the calculation.

4.3 Power Exchange in an Ideal Gap

Again, some simplification is obtained in the expressions when an ideal gap is considered. For example, as D approaches zero, the radial electromagnetic power flow through the beam surface is

$$\frac{P_{ro}}{P_o} = -\frac{1}{4D} \frac{\partial(\theta)^2}{\partial T} - Z_1 \frac{\partial\theta}{\partial T}. \quad (4.3.1)$$

The first term, which is related to the stored electric energy in the gap, approaches infinity as D approaches zero, because the gap capacitance approaches infinity. The second term represents the power exchange with the beam. This second term is zero for an input gap, since the beam enters unmodulated and Z_1 is zero. For a periodic excitation, average power transfer to the beam in an intermediate or output gap will occur if Z_1 has a component in phase with $\partial\theta/\partial T$.

The gain in energy by the beam in the gap is

$$\frac{1}{P_o} \int_V \underline{E} \cdot \underline{J}_T dv = \theta \left(1 + \frac{\partial Z_1}{\partial T} \right) \quad (4.3.2)$$

Again, an input gap has no average beam energy increase since $\partial Z_1/\partial T = 0$. In intermediate or output gaps, there will be an average kinetic energy increase for a periodic excitation when θ and $\partial Z_1/\partial T$ have components which are in phase. For an ideal gap, the impedance looking into the beam is zero, from Equation (4.2.20). And finally, from Equations (4.2.7) and (4.2.10), the change in kinetic power in the beam, normalized to the d-c beam power, through an ideal gap is

$$\begin{aligned} & \left[\left(1 - \frac{\partial Z_1}{\partial Z} \right) \left(1 + \frac{dZ_1}{dT} \right)^3 \right]_{\text{out}} - \left[\left(1 - \frac{\partial Z_1}{\partial Z} \right) \left(1 + \frac{dZ_1}{dT} \right)^3 \right]_{\text{in}} \\ &= \left[\frac{\left(1 + \frac{\partial Z_1}{\partial T} \right)^3}{\left(1 - \frac{\partial Z_1}{\partial Z} \right)^2} \right]_{\text{out}} - \left[\frac{\left(1 + \frac{\partial Z_1}{\partial T} \right)^3}{\left(1 - \frac{\partial Z_1}{\partial Z} \right)^2} \right]_{\text{in}} \end{aligned} \quad (4.3.3)$$

For an input gap this becomes

$$\left[\left(1 - \frac{\partial Z_1}{\partial Z} \right) \left(1 + \frac{dZ_1}{dT} \right)^3 \right]_{\text{out}} - 1 = -\theta \quad , \quad (4.3.4)$$

using Equations (3.4.7) and (3.4.8).

V. INPUT GAP AND DRIFT REGION WITH CONTINUOUS-WAVE DRIVE

5.1 Exact Solution

In the remainder of this report, attention will be confined to the analysis of klystrons that have sinusoidal signals applied. In this chapter, the input gap and drift region are studied in some detail, since the results are basic to the analysis of the multigap klystron and also indicate some fruitful analysis techniques for the more general case. The general solutions obtained in Sections 3.3 and 3.4 form the basis of this discussion of the input gap and drift region.

The gap excitation in the input gap is taken as

$$\theta(T) = A \cos \sigma T \quad , \quad (5.1.1)$$

where $\sigma = \omega/\omega_p$ is the ratio of the excitation frequency to the plasma frequency. In most cases of practical interest σ is fairly large compared to unity. The polarization in the input gap is [see Equation (3.3.1)]

$$Z_1(T_1, T_0) = \frac{A}{2D(\sigma^2 - 1)} [\cos(\sigma T_0 + \sigma T_1) - \cos(\sigma T_0) \cos T_1 + \sigma \sin(\sigma T_0) \sin T_1] , \quad (5.1.2)$$

for $0 < T_1 < \Gamma$, and in the drift region that follows is [see Equation (3.3.3)]

$$Z_1(T_1, T_0) = \frac{A}{2D(\sigma^2 - 1)} [\cos(\sigma T_0 + \sigma \Gamma) \cos(T_1 - \Gamma) - \sigma \sin(\sigma T_0 + \sigma \Gamma) \sin(T_1 - \Gamma) - \cos(\sigma T_0) \cos T_1 + \sigma \sin(\sigma T_0) \sin T_1] , \quad (5.1.3)$$

for $T_1 > \Gamma$, where Γ is obtained from [see Equation (3.3.2)]

$$\Gamma + \frac{A}{2D(\sigma^2 - 1)} [\cos(\sigma T_0 + \sigma \Gamma) - \cos(\sigma T_0) \cos \Gamma + \sin(\sigma T_0) \sin \Gamma] = D \quad (5.1.4)$$

These are the exact solutions, within the limitations discussed in Section 3.6, for the polarization with a sinusoidal excitation.

For the ideal input gap, the polarization in the drift region following is [see Equation (3.4.5)]

$$Z_1(T_1, T_0) = - \left[1 - \sqrt{1 - A \cos(\sigma T_0)} \right] \sin T_1 \quad (5.1.5)$$

For $A \ll 1$, this becomes

$$Z_1(T_1, T_0) = - \frac{A}{2} \cos(\sigma T_0) \sin T_1 \quad (5.1.6)$$

Although the introduction of the T_1, T_0 variables has served admirably to make possible the exact solution of the differential equation and to obtain a qualitative picture of the state of the beam, in order to obtain a more quantitative picture of the state of the beam and evaluate the power exchange at the gaps, it is necessary to use Z and T , the laboratory variables. The exact solutions can be written in terms of the Z and T variables by replacing T_1 by $Z - Z_1$ and T_0 by $T - Z + Z_1$ [see Equations (2.1.16)]. When this is done it is seen that the exact solution for the polarization becomes an implicit relation, with the polarization, Z_1 , appearing on the right-hand side of the equation in the arguments of the various functions. This renders these exact solutions in-

convenient for computational use. It is the purpose of this and the next chapter to obtain from the exact solutions, approximate solutions that are suitable for computational use.

5.2 Ideal Gap, First-Order Approximation

As a starting point for the study of the ideal input gap, it is assumed that $\theta \ll 1$ and Equation (5.1.6) applies. This does not necessarily imply that linearity is approached. The point of electron overtaking is given by Equation (3.6.5); for sinusoidal excitation this becomes

$$\frac{A}{Z} [\sigma \sin(\sigma T_0) \sin T_1 + \cos(\sigma T_0) \cos T_1] = 1.0 \quad (5.2.1)$$

This means that the maximum allowable value of A is $\frac{1}{2}$ for $T_1 = 0$, but only $\frac{1}{2}\sigma$ for $T_1 = \pi/2$. But $T_1 = Z - Z_1 = \pi/2$, and $Z = \pi/2$ is a common drift-region length for practical klystrons. Thus if electron overtaking at any point in the drift region is to be avoided, A must be restricted to less than $2/\sigma$. For $\sigma \gg 1$ (a common situation), A will be small compared to unity. For large ratios of excitation frequency to plasma frequency, Equation (5.1.6) becomes increasingly accurate. For $\sigma = 5$ and $A = 0.4$ (the largest allowable value), the approximate expression (5.1.6) falls within 11.3 per cent of the exact expression (5.1.5), and for $\sigma = 10$, $A = 0.2$ (the largest allowable value), the approximate expression is within 5.3 per cent of the exact expression. The approximate expression essentially precludes nonlinearity within the gap but allows significant nonlinearity in the drift region.

Equation (5.1.6), expressed in the Z and T variables, is

$$Z_1(Z, T) = -\frac{A}{2} \cos(\sigma T - \sigma Z + \sigma Z_1) \sin(Z - Z_1) . \quad (5.2.2)$$

Since $A \ll 1$, then $Z_1 \ll 1$ for all values of Z and T, and the maximum value of Z_1 will occur in the immediate neighborhood of $Z = \pi/2$. Therefore Z_1 can be neglected relative to Z in the $\sin(Z - Z_1)$ term since Z_1 is at its maximum (though much less than unity) where $\sin(Z - Z_1)$ is varying only slowly relative to its argument, and approaches zero where $\sin(Z - Z_1)$ varies most rapidly relative to its argument. But σZ_1 cannot be neglected in the argument of the cosine. In the neighborhood of $Z = \pi/2$, and for $A = 2/\sigma$ (the limiting value), σZ_1 will be of the order of one radian and hence can appreciably affect the value of the cosine term. For $\sigma \gg 1$, then,

$$Z_1(Z, T) = -\frac{A}{2} \cos(\sigma T - \sigma Z + \sigma Z_1) \sin Z . \quad (5.2.3)$$

Equation (5.2.3) can be rearranged to give,

$$\sigma T - \sigma Z + \sigma Z_1 = \sigma T - \sigma Z - \frac{\sigma A}{2} \sin Z \cos(\sigma T - \sigma Z + \sigma Z_1) . \quad (5.2.4)$$

This has the form

$$y = x + C \cos y , \quad (5.2.5)$$

where

$$y = \sigma T - \sigma Z + \sigma Z_1 , \quad x = \sigma T - \sigma Z , \quad C = -\frac{\sigma A}{2} \sin Z .$$

It is shown in Appendix C that for an equation of this type, y can be

obtained explicitly as a Fourier series in x . The Fourier coefficients for this particular equation are obtained in Section C. 3 and the resulting Fourier series is

$$\begin{aligned}
 y &= \sum_{n=1}^{\infty} \frac{2}{n} J_n(nc) \left[\sin\left(\frac{n\pi}{2}\right) \cos(nx) + \cos\left(\frac{n\pi}{2}\right) \sin(nx) \right] , \\
 &= \sum_{n=1}^{\infty} \frac{2}{n} J_n(nc) \sin\left[n\left(x + \frac{\pi}{2}\right)\right] , \quad (5.2.6)
 \end{aligned}$$

where $J_n(nc)$ is a Bessel function of the first kind of order n and argument nc . The resultant expression for the polarization is

$$Z_1(Z, T) = \sum_{n=1}^{\infty} \frac{2}{\sigma n} J_n\left(\frac{n\sigma A}{2} \sin Z\right) \sin\left[n\left(\sigma T - \sigma Z - \frac{\pi}{2}\right)\right] . \quad (5.2.7)$$

To obtain this, the relation $J_n(-x) = (-1)^n J_n(x)$ was used and the $(-1)^n$ absorbed by changing the sign of the $\pi/2$ in the sine term. The region of convergence of this series (see Appendix C) is $\frac{\sigma A \sin Z}{2} < 1$. This is essentially equivalent to the restriction to operate below electron overtaking.

Not only has this inversion process given an explicit relation for $Z_1(Z, T)$, but the relation obtained is in the form of a summation of the harmonics of the excitation signal since $n\sigma T = n\omega t$. This is convenient for computation. The electric field in the drift region is proportional to Z_1 [see Equation (2.1.13)] and with Equations (2.1.18), (2.1.19), and (2.1.20) the a-c current density, charge density, and velocity may be obtained:

$$\frac{J(Z, T)}{J_0} = -2 \sum_{n=1}^{\infty} J_n \left(\frac{n\sigma A}{Z} \sin Z \right) \cos \left[n \left(\sigma T - \sigma Z - \frac{\pi}{2} \right) \right], \quad (5.2.8)$$

$$\begin{aligned} \frac{\rho(Z, T)}{\rho_0} &= \sum_{n=1}^{\infty} A \cos Z J'_n \left(\frac{n\sigma A}{Z} \sin Z \right) \sin \left[n \left(\sigma T - \sigma Z - \frac{\pi}{2} \right) \right] \\ &\quad - 2 J_n \left(\frac{n\sigma A}{Z} \sin Z \right) \cos \left[n \left(\sigma T - \sigma Z - \frac{\pi}{2} \right) \right] \end{aligned} \quad (5.2.9)$$

$$\begin{aligned} \frac{u(Z, T)}{u_0} &= \left(\sum_{n=1}^{\infty} A \cos Z J'_n \left(\frac{n\sigma A}{Z} \sin Z \right) \sin \left[n \left(\sigma T - \sigma Z - \frac{\pi}{2} \right) \right] \right. \\ &\quad \left. 1 - \sum_{n=1}^{\infty} \left\{ A \cos Z J'_n \left(\frac{n\sigma A}{Z} \sin Z \right) \sin \left[n \left(\sigma T - \sigma Z - \frac{\pi}{2} \right) \right] \right. \right. \\ &\quad \left. \left. - 2 J_n \left(\frac{n\sigma A}{Z} \sin Z \right) \cos \left[n \left(\sigma T - \sigma Z - \frac{\pi}{2} \right) \right] \right\} \right)^{-1}. \end{aligned} \quad (5.2.10)$$

In these equations, $J'_n(x)$ denotes differentiation with respect to the argument of the Bessel function.

Several conclusions may be drawn from these results keeping in mind the model used, which included an ideal gap, the restriction to levels below electron overtaking, and the assumption that $\sigma \gg 1$. The most important relation is probably that for the current density, Equation (5.2.8). In this relation the amplitude parameter, A , appears in conjunction with

$\sigma/2$, so that in all cases for which $\sigma A/2$ is the same, the amplitude of the current density will be the same. The phase of any harmonic will be different, however, since σ appears without A in the cosine terms. This observation is not valid for the charge density and velocity relations since A appears without σ there. In all three expressions, the generation of harmonics is evident, and the start of the saturation effect for the fundamental term is also apparent since the amplitude parameter appears in the argument of a Bessel function.

Although the phase shift of any harmonic depends on σ , it is independent of the drive level. Therefore, any phase shift with drive must be a second-order effect and enter only if a more accurate expression than Equation (5.2.2) is used. Since Equation (5.2.2) becomes more accurate as σ is increased, one would surmise that any phase sensitivity to drive level should decrease with increasing σ . The location of the first maximum of the fundamental component of current density is seen to occur at $Z = \pi/2$ regardless of the drive level. Thus any shift in the location of the maximum in the fundamental component of current density can be, at most, a second-order effect, at least below electron overtaking.

Not only the fundamental component, but all the harmonics of the current density have their maxima at $Z = \pi/2$ for $A = 2/\sigma$ and $0 < Z < \pi/2$. Each component of the current density is zero at $Z = 0$. Only the fundamental component of charge density is non-zero at $Z = 0$ because $J_n(0) = 0$ for $n \geq 1$ and $J'_n(0) = 0$ for $n \geq 2$, but $J'_1(0) = 1/2$. The a-c charge density is not zero at $Z = \pi/2$, although the a-c velocity is zero there. Because the total velocity at $Z = \pi/2$ is just the original d-c velocity, the a-c charge density there is equal to the a-c current

density

$$\frac{\rho\left(\frac{\pi}{2}, T\right)}{\rho_0} = \frac{J\left(\frac{\pi}{2}, T\right)}{J_0}$$

Figure 5.2-1 presents curves of the amplitude of the normalized a-c current density (or normalized a-c charge density) versus the normalized drive parameter, $\sigma A/2$ at $Z = \pi/2$ for the first twelve harmonics of the excitation frequency. The curves are terminated at $\sigma A/2 = 1.0$, where electron overtaking occurs and the theory developed here ceases to be valid. The onset of saturation of the fundamental component is clearly evident, and at $\sigma A/2 = 1.0$, the amplitude is 1.1 db below what a linear theory would predict. In addition, the rapid growth of the amplitudes of a large number of harmonic components for $\sigma A/2$ approaching 1.0 is striking. At the electron overtaking condition, the beam current is rich in harmonic content.

The harmonic amplitudes of the current density at $Z = \pi/2$ and $\sigma A/2 = 1.0$ may be explored further. From Equation (5.2.8) the harmonic amplitudes are equal to $2J_n(n)$ for these conditions. Watson¹⁶ gives an approximate formula for $J_n(n)$ for large n . Using this, the harmonic amplitudes for large n are approximately equal to

$$\frac{2^{\frac{1}{3}} \Gamma\left(\frac{1}{3}\right)}{3^{\frac{1}{6}} \pi n^{\frac{1}{3}}} = \frac{0.895}{n^{\frac{1}{3}}} \quad (5.2.11)$$

The amplitudes are plotted as a function of n in Figure 5.2-2. They are seen to decrease very slowly with n inasmuch as they fall off only as $n^{-1/3}$.

If the abscissa of Figure 5.2-1 is taken as $\frac{\sigma A \sin Z}{2}$ rather than $\sigma A/2$, then the curves represent the amplitudes of the normalized current

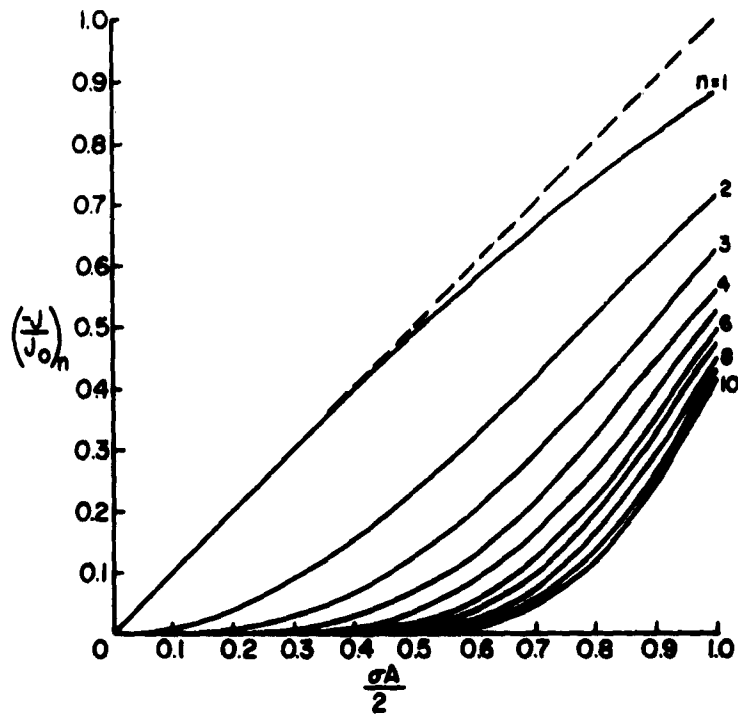


Figure 5.2-1. Normalized A-C Current Density Harmonic Amplitudes versus Normalized Excitation Level at $Z = \pi/2$.

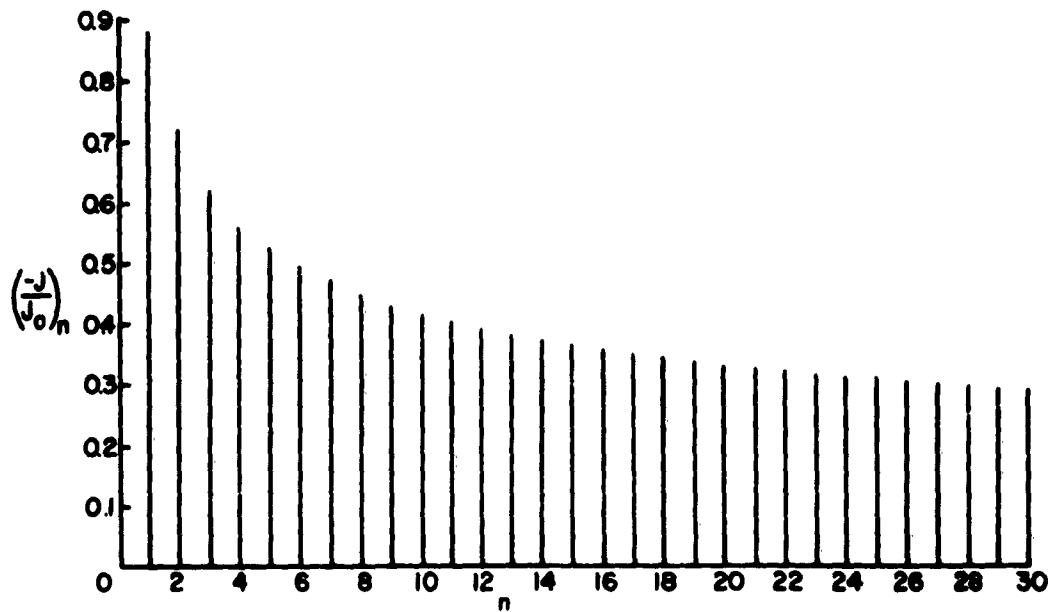


Figure 5.2-2. Normalized A-C Current Density Harmonic Amplitudes for $Z = \pi/2$ and $\sigma A / 2 = 1.0$.

density harmonics for arbitrary values of Z in the range $0 < Z < \pi/2$. If $\frac{\sigma A \sin Z}{2}$ is taken as the abscissa, the curve does not represent the charge density. The value of unity on the abscissa represents the overtaking point at the particular Z position chosen, and the theory is invalid for larger values of Z .

Figure 5.2-3 shows curves of the normalized current density harmonic amplitudes as a function of Z for $\sigma A/2 = 1.0$. It is seen that half way along the drift region the harmonic amplitudes are already significant, and, in fact, the growth of the lower harmonics in the last third of the drift region is relatively slower than in the middle third.

In contrast to the current density, the polarization has a much lower harmonic content since the harmonic components of the polarization fall off as $1/n$ relative to those of the current density. For comparison, Figure 5.2-4 presents the harmonic amplitudes of the polarization (multiplied by σ) versus $\sigma A/2$ for $Z = \pi/2$. This is to be compared with Figure 5.2-1 for the current density.

No curves of the harmonic amplitudes of the velocity will be given, since these are of less importance and cannot be readily obtained from Equation (5.2.10). It is clear, however, that except for the fundamental component, all the harmonic amplitudes are zero at $Z = 0$ and $Z = \pi/2$ and have a maximum at some intermediate position. The fundamental component is non-zero at $Z = 0$ and presumably decreases monotonically to zero at $Z = \pi/2$.

It should be kept in mind that the nonlinearity exhibited in this section is due solely to the nonlinear behavior in the drift region. The approximation made in Equation (5.1.6), in effect, discards the nonlinear

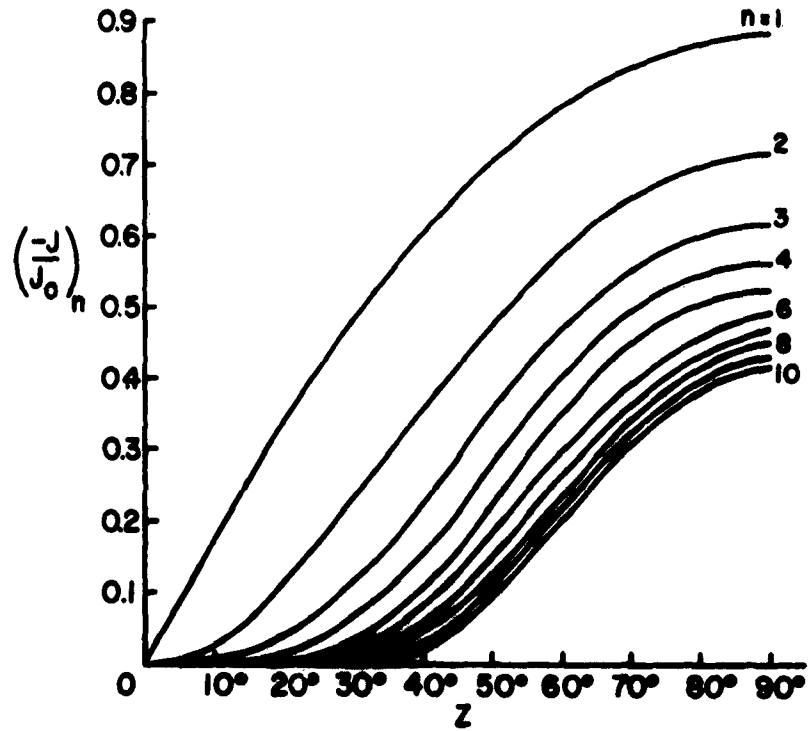


Figure 5.2-3. Normalized A-C Current Density Harmonic Amplitudes versus Normalized Distance with $\sigma A/2 = 1.0$.

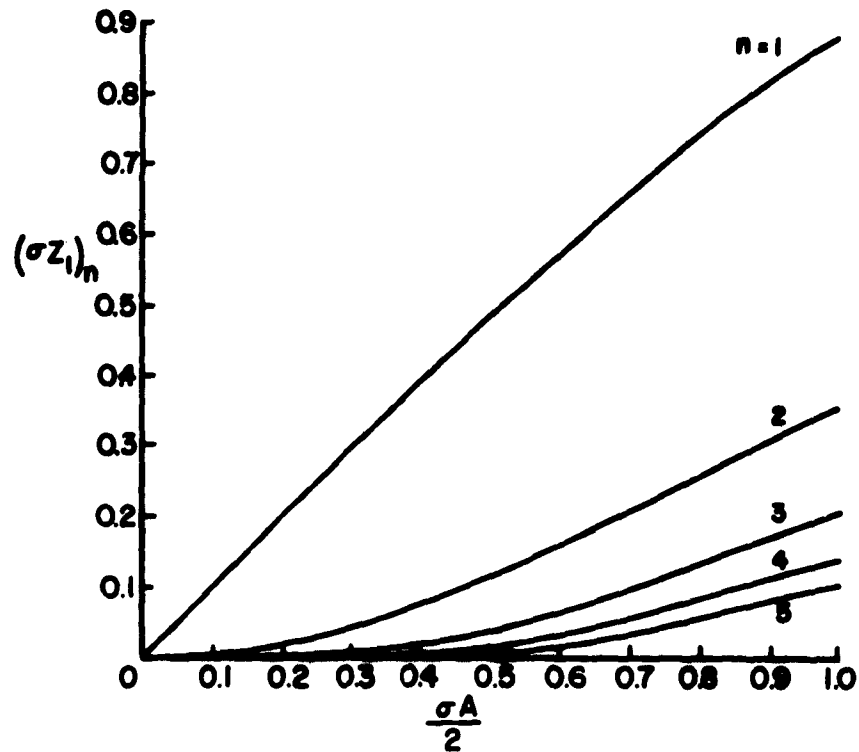


Figure 5.2-4. Normalized Polarization Harmonic Amplitudes versus Normalized Excitation Level at $z = \pi/2$.

terms in the gap region and retains only the first-order, linear term. Thus the velocity modulation imparted to the beam by the gap has only a fundamental component. To take account of the nonlinear behavior in the gap region additional terms must be used in the representation of the gap excitation.

5.3 Ideal Gap, Second-Order Approximation

The previous section considered a first approximation to the polarization in a drift region following an ideal input gap. In the approximation developed there, the space charge was so small ($\sigma = \omega/\omega_p \gg 1$), or the excitation so small ($\theta \ll 1$), that the gap modulation was linear and the only nonlinearity arose in the drift region. Thus, at the input gap only the fundamental component of the a-c velocity is non-zero.

In this section, the next order of approximation is made and a nonlinear gap modulation considered at the input gap. The basic equation is Equation (5.1.5); in the Z, T variables it is,

$$Z_1(Z, T) = - \left[1 \sqrt{1 - A \cos(\sigma T - \sigma Z + \sigma Z_1)} \right] \sin(Z - Z_1) . \quad (5.3.1)$$

The second-order approximation to the first term is obtained by expanding the square root and retaining the first three terms,

$$\begin{aligned} 1 - \sqrt{1 - A \cos(\sigma T - \sigma Z + \sigma Z_1)} \\ \cong 1 - \left[1 - \frac{A}{2} \cos(\sigma T - \sigma Z + \sigma Z_1) - \frac{A^2}{8} \cos^2(\sigma T - \sigma Z + \sigma Z_1) \right] \\ \cong \frac{A^2}{16} + \frac{A}{2} \cos(\sigma T - \sigma Z + \sigma Z_1) + \frac{A^2}{16} \cos(2\sigma T - 2\sigma Z + 2\sigma Z_1) . \end{aligned} \quad (5.3.2)$$

To be consistent, the second term of Equation (5.3.1) should also be approximated as

$$\sin(Z - Z_1) \cong \sin Z - Z_1 \cos Z \quad (5.3.3)$$

The equation for the polarization is now

$$Z_1(Z, T) = - \left[\frac{A^2}{16} + \frac{A}{2} \cos(\sigma T - \sigma Z + \sigma Z_1) + \frac{A^2}{16} \cos(2\sigma T - 2\sigma Z + 2\sigma Z_1) \right] \left[\sin(Z) - Z_1 \cos Z \right],$$

$$Z_1(Z, T) = \frac{- \left[\frac{A^2}{16} + \frac{A}{2} \cos(\sigma T - \sigma Z + \sigma Z_1) + \frac{A^2}{16} \cos(2\sigma T - 2\sigma Z + 2\sigma Z_1) \right] \sin Z}{1 - \left[\frac{A^2}{16} + \frac{A}{2} \cos(\sigma T - \sigma Z + \sigma Z_1) + \frac{A^2}{16} \cos(2\sigma T - 2\sigma Z + 2\sigma Z_1) \right] \cos Z}$$

The restriction to $A/2 < 1/\sigma$ (below electron overtaking) is still observed, and again σ is taken as large compared to unity. Then the denominator can be approximated and the whole expression rewritten as

$$\begin{aligned} Z_1(Z, T) = & - \frac{A^2}{16} (\sin Z + \sin 2Z) - \frac{A}{2} \sin Z \cos(\sigma T - \sigma Z + \sigma Z_1) \\ & - \frac{A^2}{16} (\sin Z + \sin 2Z) \cos(2\sigma T - 2\sigma Z + 2\sigma Z_1) \quad (5.3.4) \end{aligned}$$

Only terms to A^2 have been retained, consistent with the second-order approximation being developed. The accuracy of this approximation is within 2.4 per cent of the exact expression for $\sigma = 5$, $A = 0.4$ (the largest allowable value without overtaking) and with 0.6 per cent for $\sigma = 10$, $A = 0.2$ (the largest allowable value).

Equation (5. 3. 4) can be rewritten as

$$\begin{aligned} \sigma T - \sigma Z + \sigma Z_1 = & \left[\sigma T - \sigma Z - \frac{\sigma A^2}{16} (\sin Z + \sin 2Z) \right] - \frac{\sigma A}{2} \sin Z \cos (\sigma T - \sigma Z + \sigma Z_1) \\ & - \frac{\sigma A^2}{16} (\sin Z + \sin 2Z) \cos (2\sigma T - 2\sigma Z + 2\sigma Z_1) \quad . \quad (5. 3. 5) \end{aligned}$$

This has the form

$$y = x + C_1 \cos y + C_2 \cos 2y \quad , \quad (5. 3. 6)$$

where

$$y = \sigma T - \sigma Z + \sigma Z_1 \quad ,$$

$$x = \sigma T - \sigma Z - \frac{\sigma A^2}{16} (\sin Z + \sin 2Z) \quad ,$$

$$C_1 = - \frac{\sigma A}{2} \sin Z \quad ,$$

$$C_2 = - \frac{\sigma A^2}{16} (\sin Z + \sin 2Z) \quad . \quad (5. 3. 7)$$

In Appendix C, Section C. 4, an equation of this type is solved explicitly for y in terms of x . From the result obtained there, the polarization is

$$\begin{aligned} Z_1(Z, T) = & - \frac{A^2}{16} (\sin Z + \sin 2Z) + \frac{1}{\sigma} \sum_{n=1}^{\infty} \left\{ a_n \cos \left[n\sigma T - n\sigma Z - \frac{n\sigma A^2}{16} (\sin Z + \sin 2Z) \right] \right. \\ & \left. + b_n \sin \left[n\sigma T - n\sigma Z - \frac{n\sigma A^2}{16} (\sin Z + \sin 2Z) \right] \right\} \quad . \quad (5. 3. 8) \end{aligned}$$

The values for a_n and b_n are obtained from Equations (C. 4. 7) - (C. 4. 10) with C_1 and C_2 given in Equation (5. 3. 7). The a-c current density is

$$\frac{J(Z, T)}{J_0} = \sum_{n=1}^{\infty} n \left\{ a_n \sin \left[n\sigma T - n\sigma Z - \frac{n\sigma A^2}{16} (\sin Z + \sin 2Z) \right] - b_n \cos \left[n\sigma T - n\sigma Z - \frac{n\sigma A^2}{16} (\sin Z + \sin 2Z) \right] \right\} . \quad (5.3.9)$$

The a-c charge density and velocity are somewhat more complicated in appearance (recall that a_n and b_n are functions of Z) and will not be written here, although they may be obtained in a straightforward manner.

There are several points in which these solutions differ from those obtained in the previous section using the first-order approximation. These points are, (a) the polarization has a d-c term which is dependent on the excitation level, (b) the amplitude of the various harmonics will depend somewhat differently on the excitation, and the values at crossover are different, and (c) each of the harmonics has a phase shift which is dependent on the excitation level. These various points will be discussed in turn.

The d-c term in the polarization is

$$- \frac{A^2}{16} (\sin Z + \sin 2Z) . \quad (5.3.10)$$

Since the electric field in the drift region is proportional to the polarization [Equation (2.1.13)], the electric field will have a d-c component in the drift region. For the model used here, the appearance of this d-c electric field is somewhat awkward because it was initially assumed that the d-c space charge of the originally undisturbed electron beam was neutralized by stationary positive ions. No provision has been made to include any motion of these positive ions, their mass having been assumed to be so

large compared to the electron mass that such motion was negligible. However, with the appearance of a d-c electric field in the drift region, the positive ions would have to have an infinite mass to preclude their motion. If they do move, the solution obtained here becomes invalid, at least to some degree. In order to retain this solution one must assume either that the positive ion mass is infinite, or that the excitation is in the form of pulses of sufficiently short duration that the ions do not have time to move. Although the occurrence of this d-c electric field has cast doubt on the applicability of this second-order solution, it is believed to be still of considerable interest in providing an understanding of some of the other nonlinear effects, and therefore these will be explored.

The magnitude of this d-c electric field can be estimated from the relation,

$$E = 2\beta_p V_0 Z_1 = \frac{J_0}{\omega_p \epsilon} Z_1 \quad (5.3.11)$$

As a reference value with which this might be compared, one might take the d-c electric field, E'_0 , which the undisturbed electrons in the original beam would produce. Note that one would not observe E'_0 experimentally because of the presence of the positive ions and that E'_0 is not the field that would exist in the absence of positive ions:

$$E'_0 = \frac{-J_0 Z}{\omega_p \epsilon} + \text{constant} \quad (5.3.12)$$

Taking $E'_0 = 0$ at $Z = 0$, gives

$$\frac{E}{E'_0} = -\frac{Z_1}{Z} \quad ; \quad (5.3.13)$$

the ratio of the d-c part of E to E'_0 is then

$$\frac{A^2}{16Z} (\sin Z + \sin 2Z) \quad (5.3.14)$$

Since to preclude overtaking, the restriction on A will still be that it must be less than approximately $2/\sigma$, the magnitude of this ratio is of the order of $\frac{1}{4} \sigma^2$ at most. For σ large, this will be quite small.

It is of interest that this d-c component of the electric field is zero at $Z = 0$ and π radians and has a maximum value at $Z = 0.94$ radian. The value at $Z = \pi/2$ radians is about 57 per cent of the maximum value. Of course, there is no change in the d-c component of the current density with excitation since the source of the electrons is unaffected by the presence of excitation.

The Fourier component of the current density of most interest is the fundamental component. From Equation (5.3.9), this may be written as

$$\left[\frac{J(Z, T)}{J_0} \right]_1 = \sqrt{a_1^2 + b_1^2} \sin \left[\sigma T - \sigma Z - \frac{\sigma A^2}{16} (\sin Z + \sin 2Z) - \tan^{-1} \left(\frac{b_1}{a_1} \right) \right] \quad (5.3.15)$$

From Appendix C, Section C.4, a_1 and b_1 are

$$\begin{aligned} a_1 = & -2J_1 \left(\frac{\sigma A}{Z} \sin Z \right) J_0 \left[\frac{\sigma A^2}{16} (\sin Z + \sin 2Z) \right] \\ & + 2 \sum_{m=1}^{\infty} \left\{ \sin \left(\frac{3m}{2} \pi \right) J_{2m+1} \left(\frac{\sigma A}{Z} \sin Z \right) J_{m+1} \left[\frac{\sigma A^2}{16} (\sin Z + \sin 2Z) \right] \right. \\ & \left. - \cos \left(\frac{3m}{2} \pi \right) J_{2m+1} \left(\frac{\sigma A}{Z} \sin Z \right) J_m \left[\frac{\sigma A^2}{16} (\sin Z + \sin 2Z) \right] \right\}, \quad (5.3.16) \end{aligned}$$

$$b_1 = -2 \sum_{m=1}^{\infty} \left\{ \cos\left(\frac{3m\pi}{2}\right) J_{2m+1}\left(\frac{\sigma A}{2} \sin Z\right) J_{m+1}\left[\frac{\sigma A^2}{16} (\sin Z + \sin 2Z)\right] \right. \\ \left. + \sin\left(\frac{3m\pi}{2}\right) J_{2m+1}\left(\frac{\sigma A}{2} \sin Z\right) J_m\left[\frac{\sigma A^2}{16} (\sin Z + \sin 2Z)\right] \right\}. \quad (5.3.17)$$

However, for $\sigma \geq 5$ and $\sigma A/2 < 1$, the series converge very rapidly and the first term alone is sufficient:

$$a_1 = -2J_1\left(\frac{\sigma A}{2} \sin Z\right) J_0\left[\frac{\sigma A^2}{16} (\sin Z + \sin 2Z)\right], \\ b_1 = -2J_3\left(\frac{\sigma A}{2} \sin Z\right) J_1\left[\frac{\sigma A^2}{16} (\sin Z + \sin 2Z)\right]. \quad (5.3.18)$$

It is also clear that $|b_1| \ll |a_1|$ so that $\tan^{-1}(b_1/a_1)$ can be replaced by b_1/a_1 .

Evaluation of a_1 and b_1 in these expressions for the range of values of σ and σA of interest here leads to a value of the amplitude of the fundamental component which is essentially the same as that found in the previous section. Thus the amplitude of the fundamental component versus $\sigma A/2$ or Z is very closely given by the appropriate curves of Figures 5.2-1 and 5.2-3. There is no indication of any shift in the maximum value of the amplitude as a function of Z away from the $Z = \pi/2$ radian toward smaller values of Z .

The phase delay of the fundamental component at $Z = \pi/2$ can be approximated as

$$\phi_1 = + \frac{\sigma A^2}{16} \left(1 + \frac{\sigma^2 A^2}{32} \right). \quad (5.3.19)$$

This is the excitation-dependent part of the phase delay and is in addition to the spatial part $\sigma Z = \sigma \pi/2$. This portion of the phase delay is plotted in Figure 5.3-1 for $\sigma = 5$ and $\sigma = 10$. This phase delay is seen to be quite small and increases with increasing space charge (or is inversely proportional to σ).

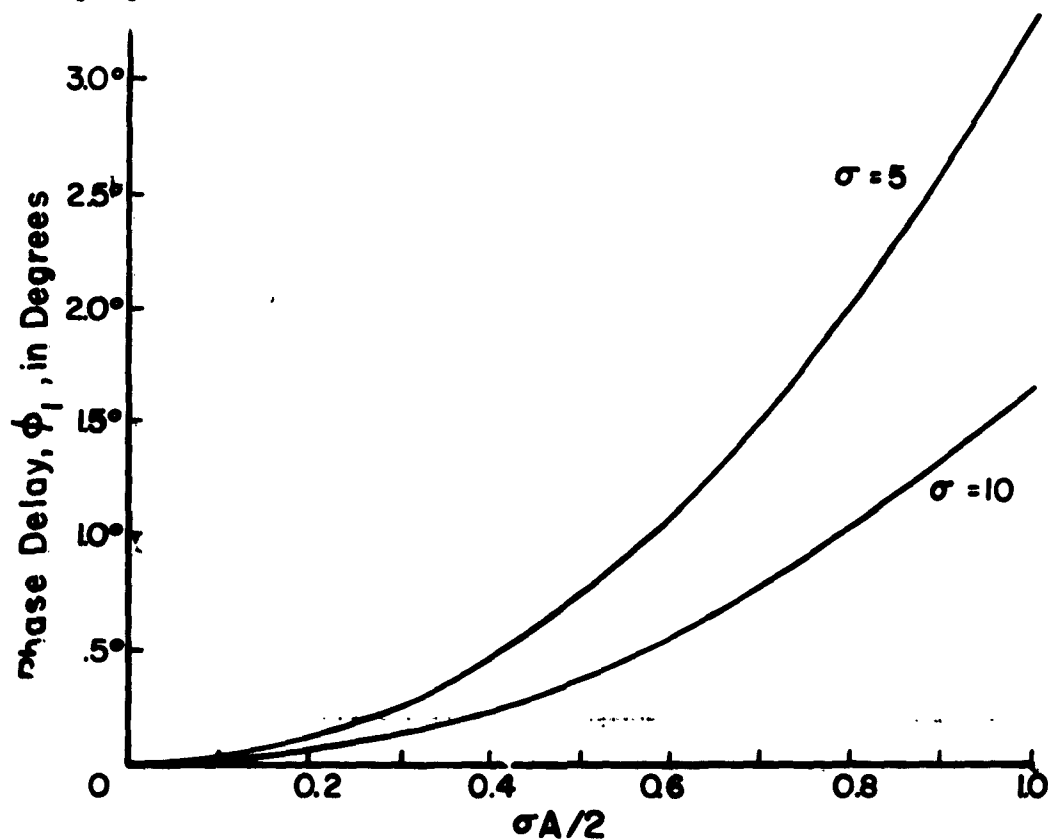


Figure 5.3-1. Excitation-Dependent Portion of the Phase Delay of the Fundamental Component of the Current Density.

To within the approximation used for the fundamental component amplitude, the second and third component amplitudes are:

$$a_2 = \left[J_0(\sigma A \sin Z) + J_4(\sigma A \sin Z) \right] J_1 \left[\frac{\sigma A^2}{8} (\sin Z + \sin 2Z) \right] ,$$

$$\begin{aligned}
b_2 &= -J_2(\sigma A \sin Z) \left\{ J_0 \left[\frac{\sigma A^2}{8} (\sin Z + \sin 2Z) \right] - J_2 \left[\frac{\sigma A^2}{8} (\sin Z + \sin 2Z) \right] \right\} , \\
a_3 &= -\frac{2}{3} \left\{ J_3 \left(\frac{3\sigma A}{2} \sin Z \right) J_0 \left[\frac{3\sigma A^2}{16} (\sin Z + \sin 2Z) \right] \right\} , \\
b_3 &= -\frac{2}{3} \left[J_1 \left(\frac{3\sigma A}{2} \sin Z \right) + J_5 \left(\frac{3\sigma A}{2} \sin Z \right) \right] J_1 \left[\frac{3\sigma A^2}{16} (\sin Z + \sin 2Z) \right] .
\end{aligned}$$

(5.3.20)

Substituting representative values in these expressions gives results which are very close to those of the previous section. Thus the second and third harmonic amplitudes are essentially as given in Figures 5.2-4 and 5.2-3. Each of these harmonics will, however, experience an excitation-dependent phase delay which was not predicted in the previous section. For somewhat higher-order harmonics, the amplitudes will be somewhat different than those obtained in the previous section, and the more accurate expressions of Appendix C would be needed to evaluate them.

The physical basis for the increase in phase delay of the fundamental component is clear. The ideal input gap does not increase or decrease the kinetic energy of the beam, but transforms some of the original d-c kinetic energy to a-c kinetic energy. For the time-average kinetic energy to remain constant, the time-average electron velocity must decrease. The average kinetic energy depends on the average of this square of the velocity. This slowing of the average velocity of the electron beam with increasing excitation produces the increasing phase delay, since the modulation is carried by the electron beam. In the previous section, the approximation used to evaluate the polarization essentially assumed that the decrease in

d-c velocity was negligible so that no excitation-dependent phase delay was obtained. In this section, the excitation-dependent phase delay was obtained because the second-order approximation did include the possibility of a d-c velocity change.

5.4 Nonideal Gap

The problem of the nonideal input gap is now examined. The exact solution for the polarization within the gap is given by Equation (5.1.2), and within the following drift region by Equation (5.1.3). The transit time within the gap, Γ , is given by the transcendental Equation (5.1.4).

First, the state of the beam in the gap region will be investigated. Rewriting the polarization in the gap, Equation (5.1.2), in terms of the Z, T variables gives

$$Z_1(Z, T) = \frac{A}{2D(\sigma^2 - 1)} \left[\cos \sigma T - \cos(\sigma T - \sigma Z + \sigma Z_1) \cos(Z - Z_1) \right. \\ \left. + \sigma \sin(\sigma T - \sigma Z + \sigma Z_1) \sin(Z - Z_1) \right] \quad (5.4.1)$$

When considering excitation levels at which no electron overtaking occurs even in the drift region following the gap, it is clear that Z_1 in the gap will be very small for large σ , although σZ_1 may be appreciable. If Z_1 is neglected relative to Z , Equation (5.4.1) may be rewritten as

$$\sigma T - \sigma Z + \sigma Z_1 = \left[\sigma T - \sigma Z + \frac{\sigma A}{2D(\sigma^2 - 1)} \cos \sigma T \right] - \frac{\sigma A}{2D(\sigma^2 - 1)} \cos Z \cos(\sigma T - \sigma Z + \sigma Z_1) \\ + \frac{\sigma^2 A}{2D(\sigma^2 - 1)} \sin Z \sin(\sigma T - \sigma Z + \sigma Z_1) \quad (5.4.2)$$

This equation has the form,

$$y = x + C_1 \cos y + C_2 \sin y \quad , \quad (5.4.3)$$

with

$$y = \sigma T - \sigma Z + \sigma Z_1 \quad ,$$

$$x = \sigma T - \sigma Z + \frac{\sigma A}{2D(\sigma^2 - 1)} \cos \sigma T \quad ,$$

$$C_1 = \frac{-\sigma A}{2D(\sigma^2 - 1)} \cos Z \quad ,$$

$$C_2 = \frac{\sigma^2 A}{2D(\sigma^2 - 1)} \sin Z \quad . \quad (5.4.4)$$

The results obtained in Appendix C, Section C. 5, show that $y - x$ can be expanded in a Fourier series in $x - \tan^{-1}(C_2/C_1)$:

$$\begin{aligned} x - \tan^{-1}\left(\frac{C_2}{C_1}\right) &= \sigma T - \sigma Z + \frac{\sigma A}{2D(\sigma^2 - 1)} \cos \sigma T - \tan^{-1}(-\sigma \tan Z) \\ &= \sigma T - \sigma Z + \tan^{-1}(\sigma \tan Z) + \frac{\sigma A}{2D(\sigma^2 - 1)} \cos \sigma T \quad . \quad (5.4.5) \end{aligned}$$

Using the results of Section C. 5, gives the polarization,

$$\begin{aligned} Z_1(Z, T) &= \frac{A}{2D(\sigma^2 - 1)} \cos \sigma T + \sum_{n=1}^{\infty} \frac{2(-1)^n}{\sigma n} J_n \left[\frac{n\sigma A}{2D(\sigma^2 - 1)} Q(Z) \right] \sin \left[n\sigma T \right. \\ &\quad \left. - n\sigma Z + n \tan^{-1}(\sigma \tan Z) + \frac{n\pi}{2} + \frac{n\sigma A}{2D(\sigma^2 - 1)} \cos \sigma T \right] \quad , \quad (5.4.6) \end{aligned}$$

with

$$Q(Z) = \sqrt{\cos^2 Z + \sigma^2 \sin^2 Z} \quad (5.4.7)$$

This expression for the polarization is not in as convenient a form as those obtained in previous sections. Here, because $\cos \sigma T$ appears in the argument of the sine term, the expression is not a sum of harmonics of the excitation frequency. But a transformation can be made to the more convenient form:

$$\sin(a + b \cos c) = \sin a \cos(b \cos c) + \cos a \sin(b \cos c)$$

$$\begin{aligned} &= 2 \sin a \sum_{m=0}^{\infty} (-1)^m \epsilon_m J_{2m}(b) \cos(2mc) \\ &\quad + 2 \cos a \sum_{m=0}^{\infty} (-1)^m J_{2m+1}(b) \cos[(2m+1)c] \\ &= \sum_{m=0}^{\infty} (-1)^m \left(\epsilon_m J_{2m}(b) [\sin(a + 2mc) + \sin(a - 2mc)] \right. \\ &\quad \left. + J_{2m+1}(b) \left\{ \cos[a + (2m+1)c] + \cos[a - (2m+1)c] \right\} \right) \end{aligned} \quad (5.4.8)$$

with $\epsilon_m = 1/2$, $m = 0$, and $\epsilon_m = 1$, $m \geq 1$. With these relations, after considerable algebra, the polarization can be written as a sum of harmonics of the excitation frequency:

$$Z_1(Z, T) = - \sum_{m=1}^{\infty} \frac{2}{\sigma m} J_m \left[\frac{m\sigma A}{2D(\sigma^2 - 1)} Q(Z) \right] J_m \left[\frac{m\sigma A}{2D(\sigma^2 - 1)} \right] \sin[m\sigma Z - m \tan^{-1}(\sigma \tan Z)] + \frac{A}{2D(\sigma^2 - 1)} \cos \sigma T$$

$$+ \sum_{n=1}^{\infty} \sum_{m=1}^{\infty} \frac{2(-1)^m}{\sigma m} J_m \left[\frac{m\sigma A}{2D(\sigma^2 - 1)} Q(Z) \right] \left\{ 2\epsilon_{n-m} J_{n-m} \left[\frac{m\sigma A}{2D(\sigma^2 - 1)} \right] \sin[n\sigma T - m\sigma Z + m \tan^{-1}(\sigma \tan Z) + \frac{n\pi}{2}] \right.$$

$$\left. - (-1)^m J_{n+m} \left[\frac{m\sigma A}{2D(\sigma^2 - 1)} \right] \sin[n\sigma T + m\sigma Z - m \tan^{-1}(\sigma \tan Z) - \frac{n\pi}{2}] \right\} \quad (5.4.9)$$

-69-

The current density in the gap is,

$$\frac{J}{J_0} = \frac{\sigma A}{2D(\sigma^2 - 1)} \sin \sigma T - \sum_{n=1}^{\infty} \sum_{m=1}^{\infty} \frac{2n(-1)^m}{m} J_m \left[\frac{m\sigma A}{2D(\sigma^2 - 1)} Q(Z) \right] \left\{ 2\epsilon_{n-m} J_{n-m} \left[\frac{m\sigma A}{2D(\sigma^2 - 1)} \right] \cos \left[n\sigma T - m\sigma Z \right. \right.$$

$$\left. \left. + m \tan^{-1}(\sigma \tan Z) + \frac{n\pi}{2} \right] - (-1)^m J_{n+m} \left[\frac{m\sigma A}{2D(\sigma^2 - 1)} \right] \cos \left[n\sigma T + m\sigma Z - m \tan^{-1}(\sigma \tan Z) - \frac{n\pi}{2} \right] \right\} \quad (5.4.10)$$

The range of validity of these expressions may be determined from Appendix C. This is a somewhat complicated function of the parameters, but roughly, for $Z \cong 0, \pi, 2\pi, \text{etc.}$,

$$\frac{\sigma A}{2D(\sigma^2 - 1)} < 1 \quad ; \quad (5.4.11a)$$

for Z in the neighborhood of $\pi/2, 3\pi/2, \text{etc.}$,

$$\frac{\sigma^2 A}{2D(\sigma^2 - 1)} < 1 \quad ; \quad (5.4.11b)$$

Z is, of course, restricted to be less than D .

It is of interest to determine what the polarization and current are for small values of Z , i.e., small compared to the plasma wavelength. In the following discussion, no restrictions are placed on D . For small Z , the expressions for the polarization and current density may be expanded in a Taylor series in Z . The first term which is not zero is the Z^2 term; thus the first two terms are

$$\begin{aligned} Z_1(Z, T) = & \frac{A}{2D} Z^2 \sum_{n=1}^{\infty} \sum_{m=1}^{\infty} (-1)^m J'_m \left[\frac{m\sigma A}{2D(\sigma^2 - 1)} \right] \left\{ 2\epsilon_{n-m} J_{n-m} \left[\frac{m\sigma A}{2D(\sigma^2 - 1)} \right] \sin\left(n\sigma T + \frac{n\pi}{2}\right) \right. \\ & \left. - (-1)^m J_{n+m} \left[\frac{m\sigma A}{2D(\sigma^2 - 1)} \right] \sin\left(n\sigma T - \frac{n\pi}{2}\right) \right\} - \frac{2}{3}(\sigma^2 - 1) Z^3 \left(\sum_{m=1}^{\infty} J_m^2 \left[\frac{m\sigma A}{2D(\sigma^2 - 1)} \right] \right. \\ & + \sum_{n=1}^{\infty} \sum_{m=1}^{\infty} (-1)^m J_m \left[\frac{m\sigma A}{2D(\sigma^2 - 1)} \right] \left\{ 2\epsilon_{n-m} J_{n-m} \left[\frac{m\sigma A}{2D(\sigma^2 - 1)} \right] \cos\left(n\sigma T + \frac{n\pi}{2}\right) \right. \\ & \left. \left. + (-1)^m J_{n+m} \left[\frac{m\sigma A}{2D(\sigma^2 - 1)} \right] \cos\left(n\sigma T - \frac{n\pi}{2}\right) \right\} \right) , \quad (5.4.12) \end{aligned}$$

$$\begin{aligned}
\frac{J}{J_0} \cong & -\frac{\sigma A}{2D} Z^2 \sum_{n=1}^{\infty} n \sum_{m=1}^{\infty} (-1)^m J'_m \left[\frac{m\sigma A}{2D(\sigma^2-1)} \right] \left\{ 2\epsilon_{n-m} J_{n-m} \left[\frac{m\sigma A}{2D(\sigma^2-1)} \right] \cos \left(n\sigma T + \frac{n\pi}{2} \right) \right. \\
& \left. - (-1)^m J_{n+m} \left[\frac{m\sigma A}{2D(\sigma^2-1)} \right] \cos \left(n\sigma T - \frac{n\pi}{2} \right) \right\} \\
& - \frac{2}{3} \sigma (\sigma^2-1) Z^3 \sum_{n=1}^{\infty} n \sum_{m=1}^{\infty} (-1)^m J'_m \left[\frac{m\sigma A}{2D(\sigma^2-1)} \right] \left\{ 2\epsilon_{n-m} \left[\frac{m\sigma A}{2D(\sigma^2-1)} \right] \sin \left(n\sigma T + \frac{n\pi}{2} \right) \right. \\
& \left. + (-1)^m J_{n+m} \left[\frac{m\sigma A}{2D(\sigma^2-1)} \right] \sin \left(n\sigma T - \frac{n\pi}{2} \right) \right\} \quad (5.4.13)
\end{aligned}$$

In these, $J'_m(x)$ is the derivative of the Bessel function with respect to the argument. The results obtained above will be utilized and discussed further in the next section which deals with beam loading in the gap.

In the drift region following the input gap, the exact solution for the polarization is given by Equation (5.1.3). In terms of the Z, T variables this is

$$\begin{aligned}
Z_1(Z, T) = & \frac{A}{2D(\sigma^2-1)} \left[\cos(\sigma T - \sigma Z + \sigma \Gamma + \sigma Z_1) \cos(Z - \Gamma - Z_1) \right. \\
& - \sigma \sin(\sigma T - \sigma Z + \sigma \Gamma + \sigma Z_1) \sin(Z - \Gamma - Z_1) \\
& \left. - \cos(\sigma T - \sigma Z + \sigma Z_1) \cos(Z - Z_1) + \sigma \sin(\sigma T - \sigma Z + \sigma Z_1) \sin(Z - Z_1) \right] \quad (5.4.14)
\end{aligned}$$

In order to obtain an approximate solution for Z_1 , the gap transit angle, Γ , must be evaluated.

The gap transit angle, Γ , is given by the transcendental equation (5.1.14). When this equation is expressed in the Z, T variables (with $Z = D$), then $Z_1(D, T)$ appears on the left-hand side. The nature of the equation makes it difficult to obtain an exact solution. It is possible, however, to develop Γ as a power series in the excitation parameter, $\sigma A/2$. The first three terms in the series are

$$\frac{\Gamma}{D} = 1 + \frac{M}{\sigma D^2(\sigma^2 - 1)} \frac{\sigma A}{2} \cos(\sigma T + \nu) + \frac{M \sin D}{2\sigma^3 D^3(\sigma^2 - 1)} \left(\frac{\sigma A}{2}\right)^2 [\cos(\nu + \sigma D) + \cos(2\sigma T + \nu - \sigma D)], \quad (5.4.15)$$

where

$$M = [1 + \cos^2 D + \sigma^2 \sin^2 D - 2 \cos D \cos \sigma D - 2 \sin D \sin \sigma D]^{\frac{1}{2}},$$

$$\nu = \tan^{-1} \left[\frac{\sin \sigma D \cos D - \sigma \cos \sigma D \sin D}{1 - \cos \sigma D \cos D - \sigma \sin \sigma D \sin D} \right] \quad (5.4.16)$$

The positive square root is taken for M and the principal value for ν . The first-order term in $\sigma A/2$ contributes an a-c portion to the gap transit angle at the fundamental excitation frequency. The second-order term contributes a correction to the average transit angle plus an a-c term at the second harmonic of the excitation frequency.

Figure 5.4-1a shows the variation of $M/\sigma D^2(\sigma^2 - 1)$ versus σD with σ as a parameter. The amplitude of the fundamental frequency

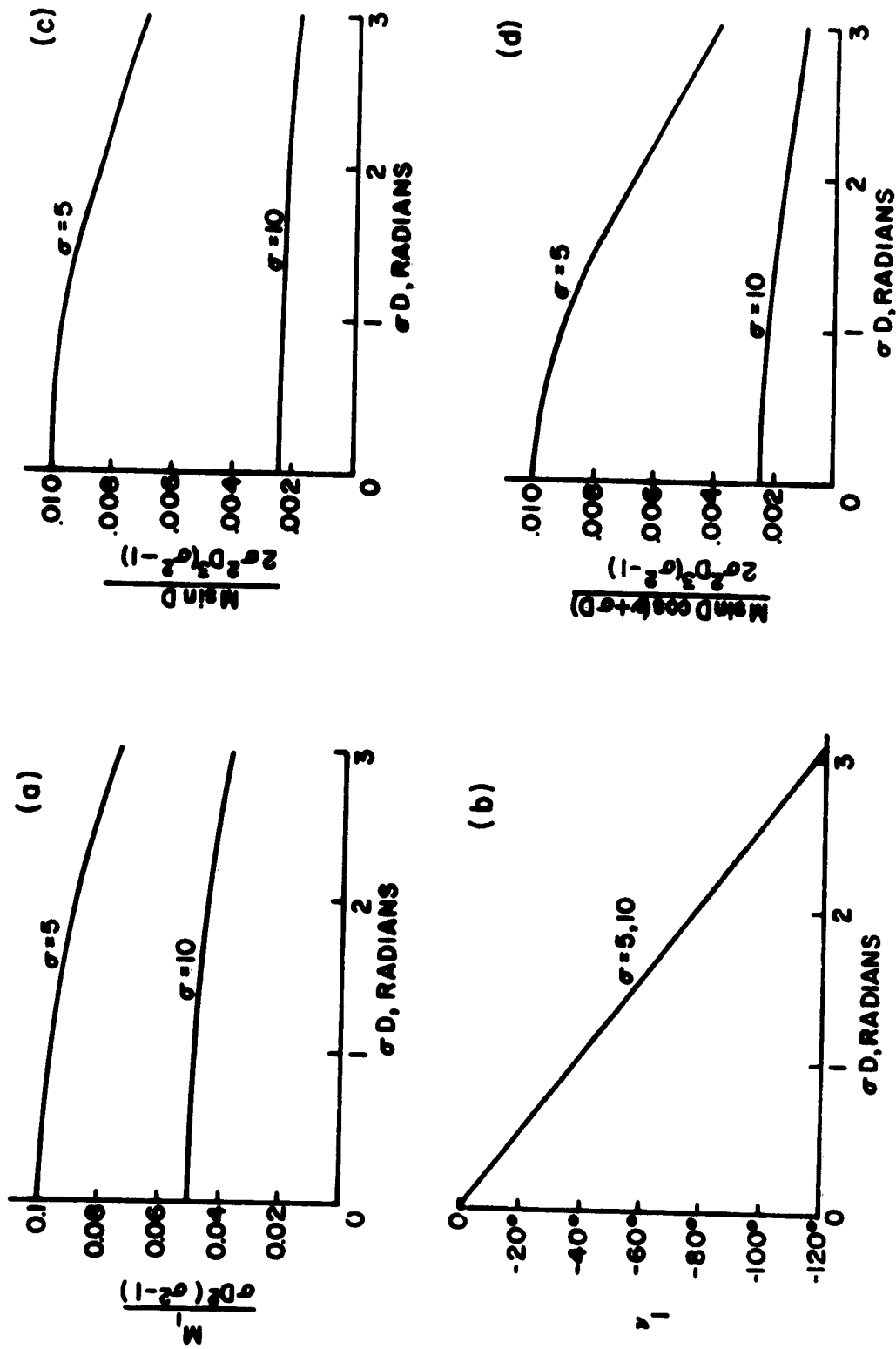


Figure 5.4-1. Gap Transit Angle Parameters as a Function of Normalized Gap Length.

component of the transit angle is given by the product of the ordinate and $(\sigma A/2)D$. Normal klystron gap lengths are such that σD lies between one and two radians. If $\sigma A/2 < 1$, it is seen that the maximum amplitude of the fundamental frequency component of Γ will be less than ten per cent of D for $\sigma = 5$ and less than five per cent of D for $\sigma = 10$. Figure 5.4-1b gives the phase angle associated with the fundamental frequency as a function of σD . Although the curves are not precisely identical for $\sigma = 5$ and 10 , they fall within a degree of each other for the range shown. For small σD , $M/\sigma D^2(\sigma^2 - 1)$ approaches $1/2\sigma$ and ν approaches $(-2/3)\sigma D$.

The coefficient for the second-order term, $\frac{M \sin D}{2\sigma^2 D^3(\sigma^2 - 1)}$, is given as a function of σD in Figure 5.4-1c. For small σD , this approaches $1/4\sigma^2$. Figure 5.4-1d shows the correction term for the average value of the normalized gap transit angle, Γ/D . Both of these, of course, are multiplied by $(\sigma A/2)^2$ to give the actual value. For $\sigma A/2 = 1$, the curves show that the contribution to Γ/D from the second-order terms will be less than one per cent for $\sigma = 5$ and less than one-quarter of one per cent for $\sigma = 10$.

In the expression for the polarization, Equation (5.4-14), again it is reasonable to neglect Z_1 compared to Z in all terms in which it is not multiplied by σ . As before, the larger σ is, the better this approximation is. Likewise, it is equally reasonable to replace Γ by D in those terms in which it is not multiplied by σ . One might then proceed by using the first two terms of Equation (5.4.15) to approximate Γ in Equation (5.4.14) and try to obtain an approximate solution for the polarization. For the purposes of this report, the complexity introduced by retaining an a-c term in the gap transit angle, Γ , is not justified.

Since the a-c term will always be small in the range of variables considered here, it will be neglected and Γ replaced by D everywhere. This will give a first approximation to the results of interest, but the restricted validity of the solution must be kept in mind.

If Γ is put equal to D in Equation (5.4.14), the equation can, after considerable algebra, be put in the form,

$$\begin{aligned} \sigma T - \sigma Z + \sigma Z_1 = \sigma T - \sigma Z - \frac{\sigma A}{2D(\sigma^2 - 1)} & \left\{ Q^2(Z-D) + Q^2(Z) - 2Q(Z-D)Q(Z) \cos[\sigma D \right. \\ & \left. + \tan^{-1}(\sigma \tan(Z-D) - \tan^{-1}(\sigma \tan Z))] \right\}^{\frac{1}{2}} \cos \left[\sigma T - \sigma Z + \sigma Z_1 \right. \\ & \left. + \tan^{-1} \left(\frac{\sin \sigma D \cos(Z-D) + \sigma \cos \sigma D \sin(Z-D) - \sigma \sin Z}{\cos \sigma D \cos(Z-D) - \sigma \sin \sigma D \sin(Z-D) - \cos Z} \right) \right], \end{aligned} \quad (5.4.17)$$

with

$$Q(Z) = \sqrt{\cos^2 Z + \sigma^2 \sin^2 Z}$$

as before. Setting $y = \sigma T - \sigma Z + \sigma Z_1$, $x = \sigma T - \sigma Z$, we find that the analysis of Section C.5, Appendix C, applies directly. The polarization is

$$\begin{aligned} Z_1(Z, T) = - \sum_{n=1}^{\infty} \frac{2}{\sigma n} J_n \left[\frac{n\sigma A}{2D(\sigma^2 - 1)} P \right] & \left[\sin \frac{n\pi}{2} \cos(n\sigma T - n\sigma Z + n \tan^{-1} N) \right. \\ & \left. - \cos \frac{n\pi}{2} \sin(n\sigma T - n\sigma Z + n \tan^{-1} N) \right], \end{aligned} \quad (5.4.18)$$

with

$$P = \left\{ Q^2(Z-D) + Q^2(Z) - 2Q(Z-D)Q(Z) \cos[\sigma D + \tan^{-1}[\sigma \tan(Z-D)] - \tan^{-1}(\sigma \tan Z)] \right\}^{\frac{1}{2}},$$

$$N = \frac{\sin \sigma D \cos(Z-D) + \sigma \cos \sigma D \sin(Z-D) - \sigma \sin Z}{\cos \sigma D \cos(Z-D) - \sigma \sin \sigma D \sin(Z-D) - \cos Z} \quad (5.4.19)$$

The positive square root is taken for P and the principal value is taken for $\tan^{-1} N$. The a-c current density is

$$\begin{aligned} \frac{-J}{J_0} = \sum_{n=1}^{\infty} 2J_n \left[\frac{n\sigma A}{2D(\sigma^2 - 1)} P \right] & \left[\sin\left(\frac{n\pi}{Z}\right) \sin(n\sigma T - n\sigma Z + n \tan^{-1} N) \right. \\ & \left. + \cos\left(\frac{n\pi}{Z}\right) \cos(n\sigma T - n\sigma Z + n \tan^{-1} N) \right] \quad (5.4.20) \end{aligned}$$

The polarization has no d-c component, nor is there an excitation-dependent phase shift in the polarization or current density. This is almost certainly due to the omission of the a-c term in the gap transit angle, Γ . By analogy with the ideal gap results, one might expect that while the phase shift terms are missing here, the amplitudes of the various harmonics should be fairly accurate.

Figure 5.4-2 shows the amplitude of the fundamental component of the current density as a function of distance from the gap, $Z-D$, for $\sigma A/2 = 1$. Curves are shown for $\sigma D = 1, 2$ and $\sigma = 5, 10$. For reference, the curve for $D = 0, \sigma \geq 5$ is repeated from Figure 5.2-3. It is seen that the amplitude of the fundamental component of current density leaving the gap depends primarily on the gap length measured in terms of plasma

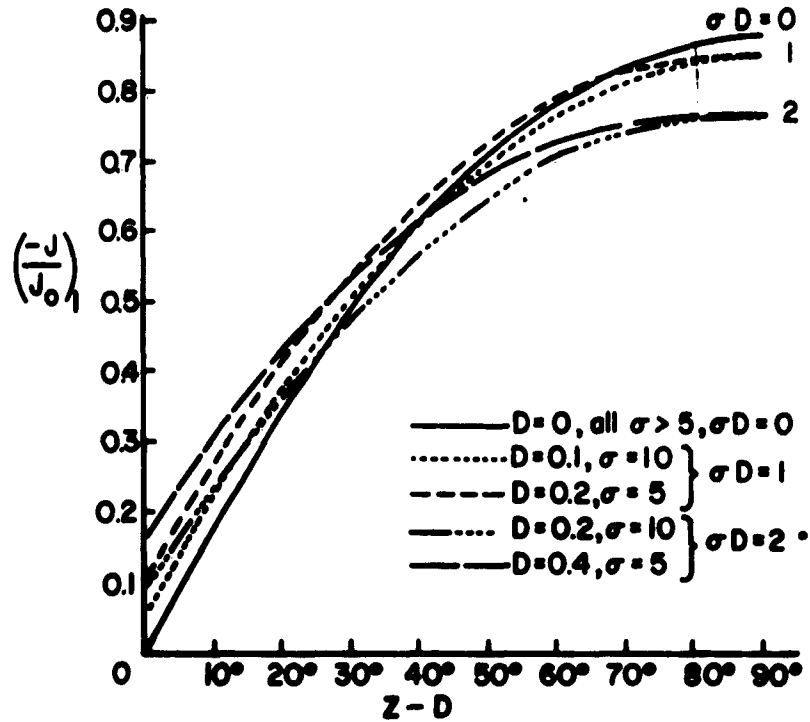


Figure 5.4-2. Fundamental Component of the Normalized Current Density versus Normalized Distance Along Drift Region.

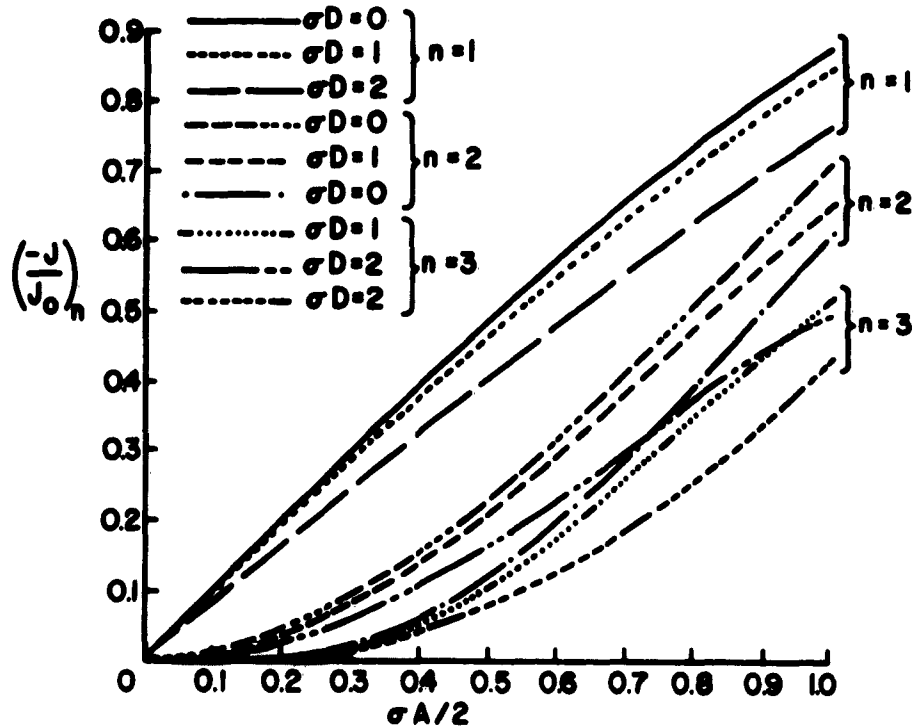


Figure 5.4-3. Normalized Current Density Harmonic Amplitudes versus Normalized Excitation Level at $Z - D = \pi/2$.

wavelength, i. e., the amplitude increases for increasing D , for the range of D considered. On the other hand, the limiting amplitude reached at $Z-D = 90^\circ$ depends on the gap length measured not in plasma wavelengths, but rather in free-space wavelengths. All gaps of the same length (i. e., same value of σD) have the same maximum amplitudes at $Z-D = 90^\circ$ regardless of the value of space charge, or σ , at least for $\sigma \geq 5$. As is known from small-signal theory, the amplitude of the fundamental current-density component is lower the longer the input gap. The degree of compression of the amplitude resulting from the nonlinearity, however, decreases with increasing gap length, σD . Thus at $Z-D = 90^\circ$, the amplitude has been decreased by 1.1 db for $\sigma D = 0$, by 1.0 db at $\sigma D = 1$, and by 0.76 db for $\sigma D = 2$ radians relative to the corresponding small-signal values (all for $\sigma A/2 = 1$).

Figure 5.4-3 shows the amplitudes of the first three harmonics of the current density versus $\sigma A/2$ at $Z-D = 90^\circ$. The three cases of $\sigma D = 0, 1$, and 2 radians are shown. At least for $\sigma \geq 5$, there is no dependence on space charge (σ) for fixed σD . It is seen that increasing the gap length, σD , decreases all of the harmonic amplitudes. In fact, the decrease in the third-harmonic amplitude at $\sigma D = 2$ compared to $\sigma D = 0$ is considerably greater than for the fundamental component, at least for $\sigma A/2 < 1$.

Figure 5.4-4 shows the behavior of the phase angle term, $\tan^{-1} N$, as a function of $Z-D$ for $\sigma D = 0, 1, 2$ and $\sigma = 5, 10$. For $\sigma D = 0$, $\tan^{-1} N = 0$. At $Z = D$, $\tan^{-1} N = \sigma D/3$.

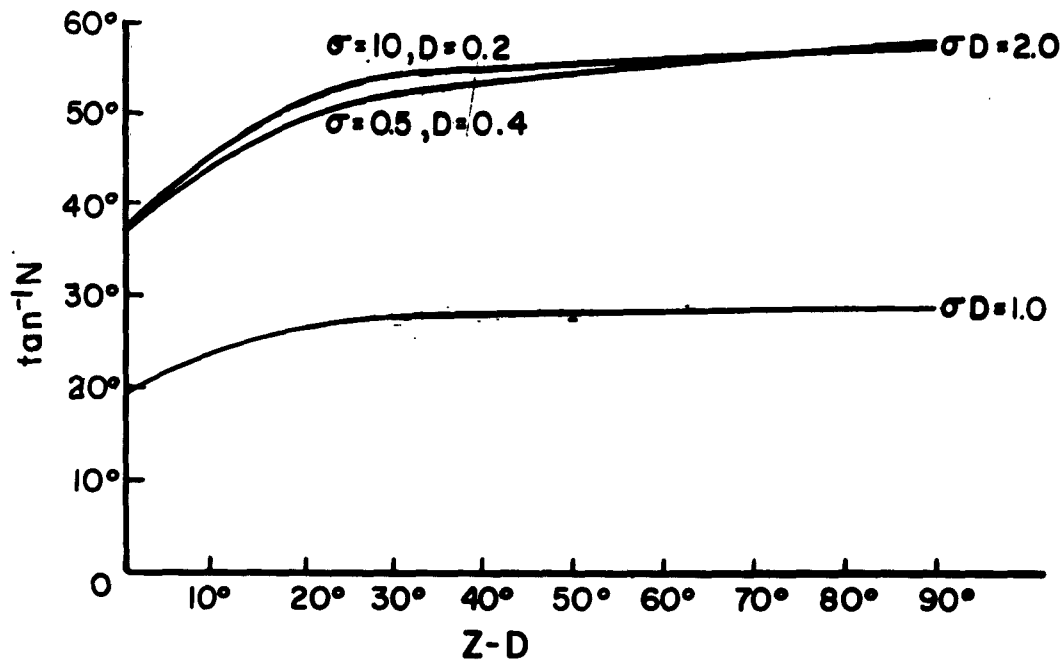


Figure 5.4-4. Finite Gap Phase Angle Term, $\tan^{-1}N$, versus Normalized Distance Along the Drift Region.

5.5 The Input Gap and Beam Loading

The basic equations to be used in discussing the input gap were obtained in the previous section. The polarization is given by Equation (5.4.9) and the a-c current density by Equation (5.4.10). Although each harmonic is made up of an infinite series of terms, the convergence of these series is rapid so that only a few terms are needed to give good results in the range of excitation levels for which the equations hold, [Equation (5.4.11)]. For the usual values of gap length, D , the restriction on the excitation level is considerably less stringent than that required to prevent electron crossover in the following drift region.

If attention is restricted to the fundamental frequency and the excitation level is restricted so that $\sigma A/2 \leq 1$, then the fundamental component of the polarization is

$$\left[Z_1(Z, T) \right]_1 = \frac{A}{2D(\sigma^2-1)} \cos \sigma T - \frac{2}{\sigma} J_1 \left[\frac{\sigma A}{2D(\sigma^2-1)} Q(Z) \right] J_0 \left[\frac{\sigma A}{2D(\sigma^2-1)} \right] \cos [\sigma T - \sigma Z + \tan^{-1}(\sigma \tan Z)], \quad (5.5.1)$$

and the fundamental component of the current density is

$$\left(\frac{J}{J_0} \right)_1 = \frac{\sigma A}{2D(\sigma^2-1)} \sin \sigma T - 2J_1 \left[\frac{\sigma A Q(Z)}{2D(\sigma^2-1)} \right] J_0 \left[\frac{\sigma A}{2D(\sigma^2-1)} \right] \sin [\sigma T - \sigma Z + \tan^{-1}(\sigma \tan Z)]. \quad (5.5.2)$$

These relations will be within a few per cent of the correct values for gap lengths in the normal range. They will become less accurate for very small values of D unless $\sigma A/2$ is restricted so that $\frac{\sigma A}{2D(\sigma^2-1)} \ll 1$.

The expression for the fundamental component of the current can also be written as

$$\left(\frac{J}{J_0} \right)_1 \cong \left\{ \left[\frac{\sigma A}{2D(\sigma^2-1)} \right]^2 + 4J_1^2 \left[\frac{\sigma A Q(Z)}{2D(\sigma^2-1)} \right] J_0^2 \left[\frac{\sigma A}{2D(\sigma^2-1)} \right] - 4 \frac{\sigma A}{2D(\sigma^2-1)} J_1 \left[\frac{\sigma A Q(Z)}{2D(\sigma^2-1)} \right] J_0 \left[\frac{\sigma A}{2D(\sigma^2-1)} \right] \cos [\sigma Z - \tan^{-1}(\sigma \tan Z)] \right\}^{\frac{1}{2}} \sin \left(\sigma T + \tan^{-1} \left\{ \frac{2J_1 \left[\frac{\sigma A Q(Z)}{2D(\sigma^2-1)} \right] J_0 \left[\frac{\sigma A}{2D(\sigma^2-1)} \right] \sin [\sigma Z - \tan^{-1}(\sigma \tan Z)]}{\frac{\sigma A}{2D(\sigma^2-1)} - 2J_1 \left[\frac{\sigma A Q(Z)}{2D(\sigma^2-1)} \right] J_0 \left[\frac{\sigma A}{2D(\sigma^2-1)} \right] \cos [\sigma Z - \tan^{-1}(\sigma \tan Z)]} \right\} \right) \quad (5.5.3)$$

In this equation the variation of the amplitude and the phase of the fundamental component of the current density with excitation level is evident.

To determine the loading of the cavity gap by the electron beam, it is necessary to find the ratio of the gap voltage to the current into the gap from the external circuit, Z_{gap} . This must be evaluated at the excitation frequency. Since in this report excitation is considered at only a single frequency, the implicit assumption is made that the cavity will respond only to the excitation frequency and not to the harmonics of the excitation frequency. From Chapter IV Z_{gap} is the negative of the ratio of the equivalent circuit voltage, V_e , to the equivalent circuit current, I_e . The impedance seen looking into the beam at the gap was given in Equation (4.2.20) and is repeated here:

$$Z_{\text{gap}} = -\frac{V_e}{I_e} = \sqrt{\frac{\mu}{\epsilon}} \frac{D}{\eta \pi R_o^2} \left(\frac{\int_0^D 2Z_1 dZ}{\frac{\partial \theta}{\partial T}} + \frac{\theta}{\frac{\partial \theta}{\partial T}} \right) \quad (5.5.4)$$

In this equation, Z_1 must be expressed in the Z, T system and only the fundamental component chosen. The second term in the parentheses is the capacitive reactance of the gap and is independent of the electron beam. This term will, therefore, be largely ignored hereafter. The first term is the beam-loading impedance,

$$Z_{\text{BL}} = \sqrt{\frac{\mu}{\epsilon}} \frac{2D}{\eta \pi R_o^2} \frac{\int_0^D Z_1 dZ}{\frac{\partial \theta}{\partial T}} \quad (5.5.5)$$

In order to evaluate the beam-loading impedance, it is necessary to integrate the fundamental component of $Z_1(Z, T)$ with respect to Z

over the length of the gap. That is, the $n = 1$ term of the expression (5.4.9) must be integrated over the length of the gap. If attention is restricted to $\sigma A/2 < 1$ and the usual values of D , then the approximate value given in Equation (5.5.1) may be used. It does not appear possible to integrate either of these two expressions directly; therefore some kind of approximation is required.

One method of approximation which may be used is valid for large σ . It is assumed that $\sigma \gg 1$, $D \ll 1$, and $\frac{\sigma A}{2D(\sigma^2-1)} < 1$; σD may have any value consistent with these requirements. Since $D \ll 1$, then $Z \ll 1$, and the approximate value for $Z_1(Z, T)$ given in Equation (5.4.12) may be used. Thus for the fundamental component,

$$\int_0^D Z_1 dZ =$$

$$\frac{AD^2}{6} \cos \sigma T \sum_{m=1}^{\infty} (-1)^m J_m \left[\frac{m\sigma A}{2D(\sigma^2-1)} \right] \left\{ 2\epsilon_{n-m} J_{n-m} \left[\frac{m\sigma A}{2D(\sigma^2-1)} \right] + (-1)^m J_{n+m} \left[\frac{m\sigma A}{2D(\sigma^2-1)} \right] \right\}$$

$$+ (\sigma^2-1) \frac{D^4}{6} \sin \sigma T \sum_{m=1}^{\infty} (-1)^m J_m \left[\frac{m\sigma A}{2D(\sigma^2-1)} \right] \left\{ 2\epsilon_{n-m} J_{n-m} \left[\frac{m\sigma A}{2D(\sigma^2-1)} \right] \right.$$

$$\left. - (-1)^m J_{n+m} \left[\frac{m\sigma A}{2D(\sigma^2-1)} \right] \right\} \quad (5.5.6)$$

If $\frac{\sigma A}{2D(\sigma^2-1)} \ll 1$ as well as $\sigma \gg 1$, $D \ll 1$, then the above relation

simplifies to

$$\int_0^D Z_1 dZ = -\frac{AD^2}{6} \cos \sigma T J_1' \left[\frac{\sigma A}{2D(\sigma^2-1)} \right] J_0 \left[\frac{\sigma A}{2D(\sigma^2-1)} \right] \\ - \frac{(\sigma^2-1)D^4}{6} \sin \sigma T J_1 \left[\frac{\sigma A}{2D(\sigma^2-1)} \right] J_0 \left[\frac{\sigma A}{2D(\sigma^2-1)} \right] \quad (5.5.7)$$

With these relations, the beam loading impedance relative to the d-c beam impedance, Z_{BO} , is

$$Z_{BO} = \frac{V_o}{I_o} = \frac{\sqrt{\frac{\mu}{\epsilon}}}{2\eta\pi R_o^2} \quad (5.5.8)$$

$$\frac{Z_{BL}}{Z_{BO}} \cong -\frac{2D^3}{3\sigma} \left(\frac{(\sigma^2-1)D^2}{A} \sum_{m=1}^{\infty} (-1)^m J_m \left[\frac{m\sigma A}{2D(\sigma^2-1)} \right] \left\{ 2\epsilon_{n-m} J_{n-m} \left[\frac{m\sigma A}{2D(\sigma^2-1)} \right] \right. \right. \\ \left. \left. - (-1)^m J_{n+m} \left[\frac{m\sigma A}{2D(\sigma^2-1)} \right] \right\} + j \sum_{m=1}^{\infty} (-1)^m J_m' \left[\frac{m\sigma A}{2D(\sigma^2-1)} \right] \left\{ 2\epsilon_{n-m} J_{n-m} \left[\frac{m\sigma A}{2D(\sigma^2-1)} \right] \right. \right. \\ \left. \left. + (-1)^m J_{n+m} \left[\frac{m\sigma A}{2D(\sigma^2-1)} \right] \right\} \right) \quad (5.5.9)$$

for $\frac{\sigma A}{2D(\sigma^2-1)} < 1$, and

$$\frac{Z_{BL}}{Z_{BO}} = + \frac{2D^3}{3\sigma} \left\{ \frac{(\sigma^2-1)D^2}{A} J_1 \left[\frac{\sigma A}{2D(\sigma^2-1)} \right] J_0 \left[\frac{\sigma A}{2D(\sigma^2-1)} \right] \right. \\ \left. + j J_1' \left[\frac{\sigma A}{2D(\sigma^2-1)} \right] J_0 \left[\frac{\sigma A}{2D(\sigma^2-1)} \right] \right\} \quad (5.5.10)$$

for $\frac{\sigma A}{2D(\sigma^2-1)} \ll 1$.

Figure 5.5-1 shows curves of the beam-loading impedance, normalized to the d-c beam impedance, Z_{BO} , versus the excitation parameter, $\sigma A/2$. These are for the case where $\sigma A/2D(\sigma^2-1) \ll 1$, with $\sigma \gg 1$ and $D \ll 1$. It is seen that the beam-loading impedance for this case is essentially insensitive to the drive level over the range shown. The only appreciable change with drive occurs for $\sigma = 5$, $D = 0.1$. For longer gap lengths, however, the sensitivity to excitation level might be considerably larger. This would require more detailed computation to investigate.

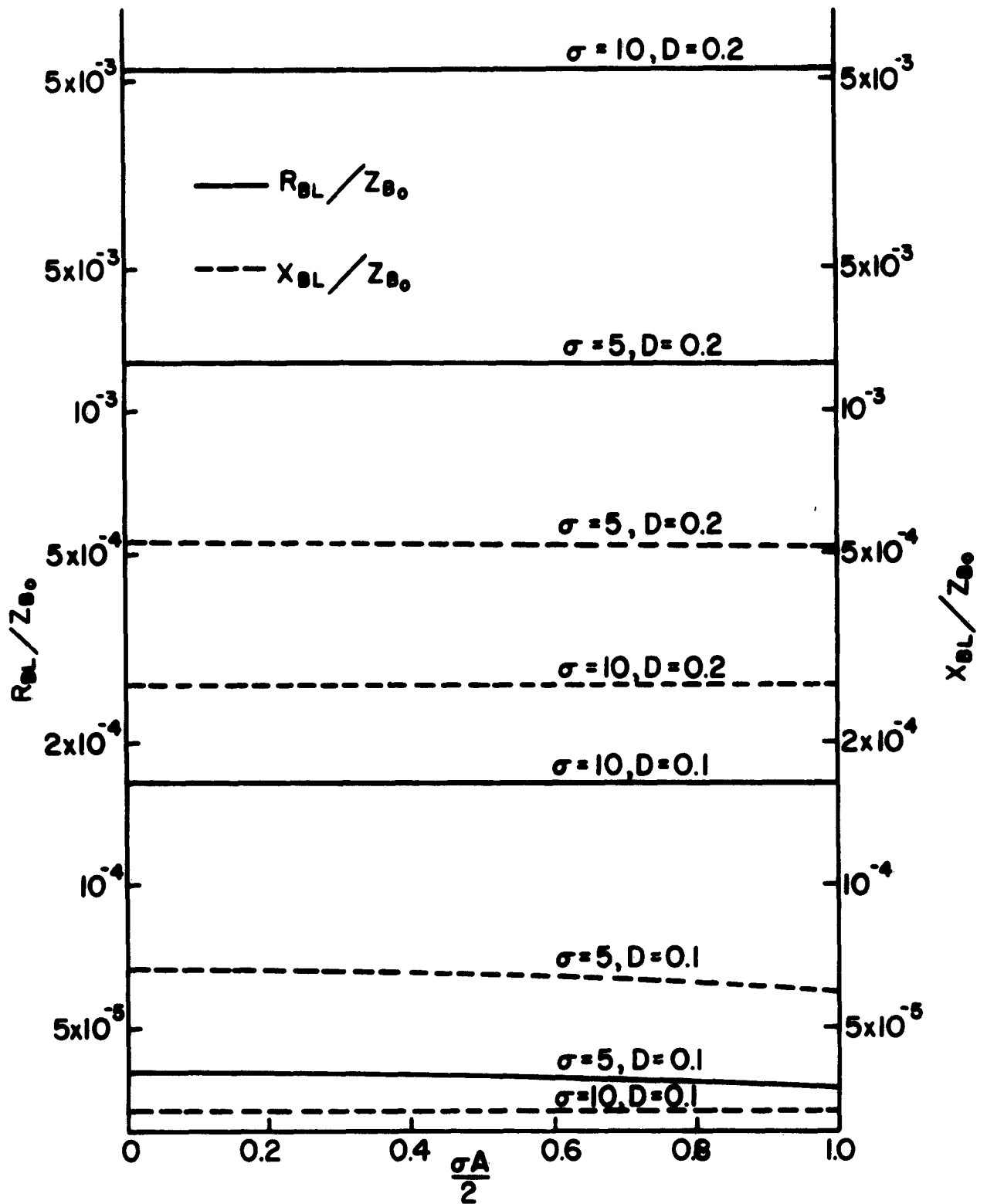


Figure 5.5-1. Normalized Beam Loading Resistance, R_{BL}/Z_{B0} , and Reactance, X_{BL}/Z_{B0} , versus Excitation Level for Short Gaps.

VI. MULTIPLE GAP AND DRIFT REGIONS WITH CONTINUOUS-WAVE DRIVE

6.1 Exact Solution

The exact solution for the case of multiple gap and drift regions with arbitrary gap excitations was developed in Section 3.5. Here the solution will be specialized to the case of continuous-wave excitation in each gap with the same frequency in each gap. This implies that any generator coupled to a gap has an output at only one frequency. Furthermore, any external load connected to any of the gaps presents zero admittance (or infinite impedance) to the beam at all frequencies that are harmonics of the excitation frequency, and a finite admittance at the excitation frequency. This must be true for single-frequency excitation, since from Section 4.2, the equivalent gap current generated by the beam has only the excitation frequency, while the equivalent gap voltage generated by the beam will have harmonics of the excitation frequency present. Figure 6.1-1 shows the case considered here schematically. The frequency of excitation is, as before, $\omega = \sigma\omega_p$.

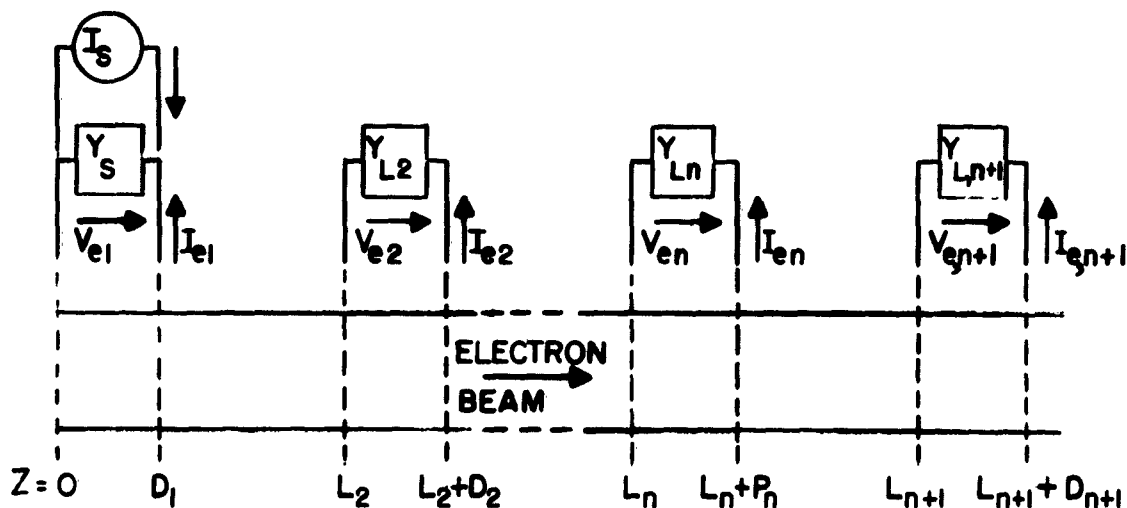


Figure 6.1-1. Schematic of Klystron with Multiple Gap and Drift Region (The load admittances, $Y_{L,n}$, are finite at $\omega = \sigma\omega_p$ and zero at all harmonics of this frequency.)

The basic equations for the exact solution in the T_1, T_0 variables are Equations (3.5.5) - (3.5.7). The excitation in the n^{th} gap is taken as

$$\theta_n(T) = A_n \cos(\sigma T + a_n) \quad (6.1.1)$$

Using this gives the polarization in the m^{th} gap as $\lambda_m < T_1 < \lambda_m + \Gamma_m$:

$$\begin{aligned} Z_1(T_1, T_0) = & \frac{1}{2(\sigma^2 - 1)} \sum_{n=1}^{m-1} \frac{A_n}{D_n} \left[-\cos(\sigma T_0 + a_n + \sigma \lambda_n + \sigma \Gamma_n) \cos(T_1 - \lambda_n - \Gamma_n) \right. \\ & + \sigma \sin(\sigma T_0 + a_n + \sigma \lambda_n + \sigma \Gamma_n) \sin(T_1 - \lambda_n - \Gamma_n) + \cos(\sigma T_0 + a_n + \sigma \lambda_n) \cos(T_1 - \lambda_n) \\ & \left. - \sigma \sin(\sigma T_0 + a_n + \sigma \lambda_n) \sin(T_1 - \lambda_n) \right] - \frac{1}{2(\sigma^2 - 1)} \frac{A_m}{D_m} \left[-\cos(\sigma T_0 + a_m + \sigma T_1) \right. \\ & \left. + \cos(\sigma T_0 + a_m + \sigma \lambda_m) \cos(T_1 - \lambda_m) - \sigma \sin(\sigma T_0 + a_m + \sigma \lambda_m) \sin(T_1 - \lambda_m) \right] . \end{aligned} \quad (6.1.2)$$

In the m^{th} drift region, $\lambda_m + \Gamma_m < T_1 < \lambda_{m+1}$, the polarization is

$$\begin{aligned} Z_1(T_1, T_0) = & -\frac{1}{2(\sigma^2 - 1)} \sum_{n=1}^m \frac{A_n}{D_n} \left[-\cos(\sigma T_0 + a_n + \sigma \lambda_n + \sigma \Gamma_n) \cos(T_1 - \lambda_n - \Gamma_n) \right. \\ & + \sigma \sin(\sigma T_0 + a_n + \sigma \lambda_n + \sigma \Gamma_n) \sin(T_1 - \lambda_n - \Gamma_n) \\ & \left. + \cos(\sigma T_0 + a_n + \sigma \lambda_n) \cos(T_1 - \lambda_n) - \sigma \sin(\sigma T_0 + a_n + \sigma \lambda_n) \sin(T_1 - \lambda_n) \right] . \end{aligned} \quad (6.1.3)$$

The parameters λ_n and Γ_n are given by

$$\begin{aligned}
L_m = \lambda_m - \frac{1}{2(\sigma^2 - 1)} \sum_{n=1}^{m-1} \frac{A_n}{D_n} & \left[-\cos(\sigma T_0 + a_n + \sigma \lambda_n + \sigma \Gamma_n) \cos(\lambda_m - \lambda_n - \Gamma_n) \right. \\
& + \sigma \sin(\sigma T_0 + a_n + \sigma \lambda_n + \sigma \Gamma_n) \sin(\lambda_m - \lambda_n - \Gamma_n) \\
& \left. + \cos(\sigma T_0 + a_n + \sigma \lambda_n) \cos(\lambda_m - \lambda_n) - \sigma \sin(\sigma T_0 + a_n + \sigma \lambda_n) \cos(\lambda_m - \lambda_n) \right] , \\
L_m + D_m = \lambda_m + \Gamma_m - \frac{1}{2(\sigma^2 - 1)} \sum_{n=1}^m \frac{A_n}{D_n} & \left[-\cos(\sigma T_0 + a_n + \sigma \lambda_n + \sigma \Gamma_n) \cos(\lambda_m + \Gamma_m - \lambda_n - \Gamma_n) \right. \\
& + \sigma \sin(\sigma T_0 + a_n + \sigma \lambda_n + \sigma \Gamma_n) \sin(\lambda_m + \Gamma_m - \lambda_n - \Gamma_n) \\
& \left. + \cos(\sigma T_0 + a_n + \sigma \lambda_n) \cos(\lambda_m + \Gamma_m - \lambda_n) - \sigma \sin(\sigma T_0 + a_n + \sigma \lambda_n) \sin(\lambda_m + \Gamma_m - \lambda_n) \right] .
\end{aligned}$$

(6.1.4)

For ideal gaps, where $D_n \rightarrow 0$, the equation for the polarization in the m^{th} drift region simplifies to

$$\begin{aligned}
Z_1(T_1, T_0) = - \sum_{n=1}^m & \left(1 - \frac{1}{2} \sum_{l=1}^{n-1} \frac{\Gamma_l}{D_l} A_l \cos(\sigma T_0 + a_l) \cos(\lambda_n - \lambda_l) \right. \\
& - \left\{ \left[1 - \frac{1}{2} \sum_{l=1}^{n-1} \frac{\Gamma_l}{D_l} A_l \cos(\sigma T_0 + a_l) \cos(\lambda_n - \lambda_l) \right]^2 - A_n \cos(\sigma T_0 + a_n) \right. \\
& \left. \left. + \sum_{l=1}^{n-1} \frac{D_l}{D_n} \frac{A_n \cos(\sigma T_0 + a_n)}{A_l \cos(\sigma T_0 + a_l)} \frac{\Gamma_l^2}{D_l^2} \frac{A_l^2}{4} \cos^2(\sigma T_0 + a_l) \cos(\lambda_n - \lambda_l) \right\}^{\frac{1}{2}} \right) \sin(T_1 - \lambda_n) .
\end{aligned}$$

(6.1.5)

$$\lambda_m - \frac{1}{2} \sum_{n=1}^{m-1} \frac{\Gamma_n}{D_n} A_n \cos(\sigma T_0 + a_n) \sin(\lambda_m - \lambda_n) = L_m \quad ,$$

$$\begin{aligned} \frac{\Gamma_m}{D_m} &= \frac{2}{A_m \cos(\sigma T_0 + a_m)} \left(1 - \frac{1}{2} \sum_{n=1}^{m-1} \frac{\Gamma_n}{D_n} A_n \cos(\sigma T_0 + a_n) \cos(\lambda_m - \lambda_n) \right. \\ &\quad - \left. \left[1 - \frac{1}{2} \sum_{n=1}^{m-1} \frac{\Gamma_n}{D_n} A_n \cos(\sigma T_0 + a_n) \cos(\lambda_m - \lambda_n) \right]^2 - A_m \cos(\sigma T_0 + a_m) \right. \\ &\quad \left. + \sum_{n=1}^{m-1} \frac{D_n}{D_m} \frac{A_m \cos(\sigma T_0 + a_m)}{A_n \cos(\sigma T_0 + a_n)} \frac{\Gamma_n^2}{D_n^2} \frac{A_n^2}{4} \cos^2(\sigma T_0 + a_n) \cos(\lambda_m - \lambda_n) \right)^{\frac{1}{2}} . \end{aligned} \quad (6.1.6)$$

If, in addition to ideal gaps, $\sigma \gg 1$, then the further simplification may be made for the polarization in the m^{th} drift region:

$$Z_1(T_1, T_0) = -\frac{1}{2} \sum_{n=1}^m A_n \cos(\sigma T_0 + a_n) \sin(T_1 - \lambda_n) \quad , \quad (6.1.7)$$

$$\lambda_m = L_m + \frac{1}{2} \sum_{n=1}^{m-1} A_n \cos(\sigma T_0 + a_n) \sin(L_m - L_n) \quad . \quad (6.1.8)$$

It is these last two equations that will be the basis for the discussions of this chapter. For reasons of simplicity, and to focus attention on the

basic nonlinear behavior, consideration will be restricted here to gap lengths which are short enough that the gaps may be considered to approach ideal gaps. This means that the gap must be short compared to the plasma wavelength, $2\pi/\beta_p = 2\pi U_o/\omega_p$. It should be recalled that throughout it has been assumed that the gaps are short compared to a free-space wavelength in order to simplify the excitation analysis. Starting from Equations (6.1.2) - (6.1.4), one could investigate the multiple-gap case for nonideal gaps at the expense of much greater complexity.

6.2 Two-Gap Case

This section discusses the approximate solution for the two-gap case when the gaps are short enough to be considered as ideal gaps. This means that the gaps are short compared to a plasma wavelength and that the polarization and beam current can be taken as constant through the gap as a function of Z . The beam velocity and charge density, may, however, change through the gap. The chief aim of this discussion will be to explore the interchange of power between the electron beam and the output gap.

The equivalent circuit for the two-gap case is shown in Figure 6.2-1. The equivalent current and voltage at the gaps are given in Equations (4.2.12) and (4.2.13). For the input gap, $\theta = A_1 \cos(\sigma T + \alpha_1)$, and $I_s = I_{s0} \cos \sigma T$. Since $Z_1 = 0$ in an ideal input gap, the equivalent current and voltage are

$$I_{e1} = - \frac{\sigma V_o \eta \pi R_o^2}{D_1 \sqrt{\frac{\mu}{\epsilon}}} A_1 \sin(\sigma T + \alpha_1) \quad , \quad (6.2.1)$$

$$V_{e1} = - V_o A_1 \cos(\sigma T + \alpha_1) \quad , \quad (6.2.2)$$

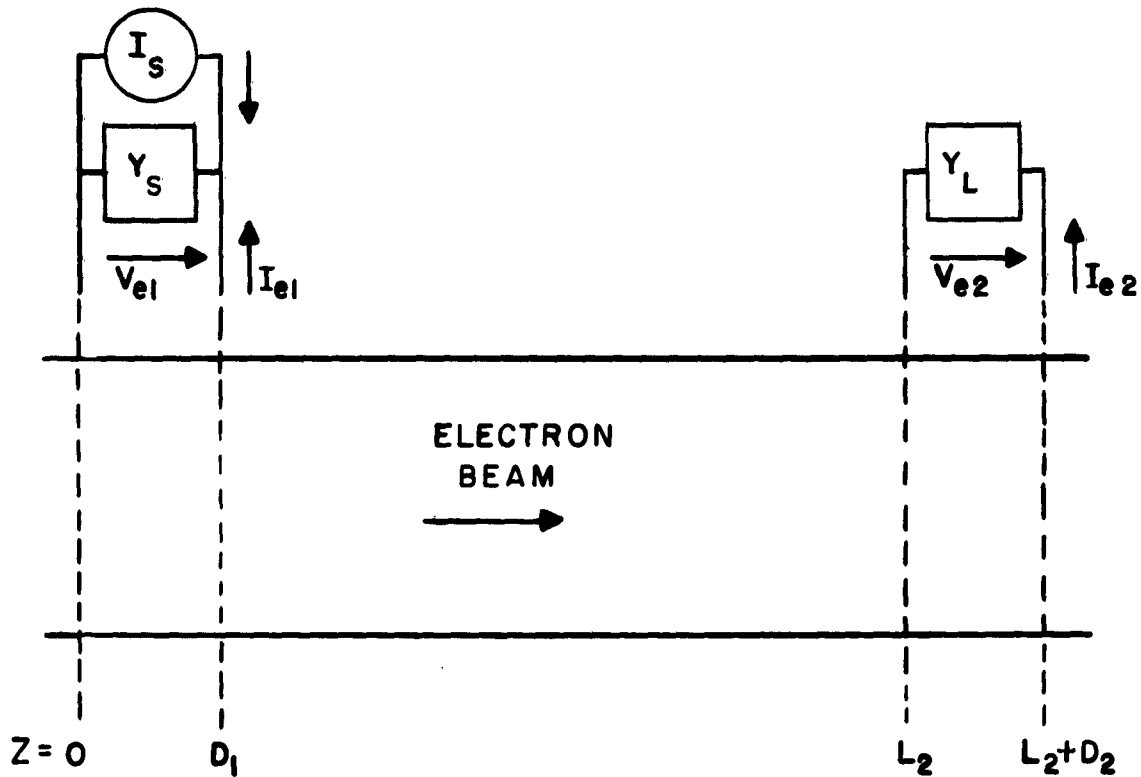


Figure 6.2-1. Schematic of Two-Gap Klystron.

where A_1 and a_1 may be determined from the equivalent circuit in terms of I_{s_0} and Y_s . Simplification can be achieved by recognizing that

$$\frac{\sigma \eta \pi R_o^2}{D_1 \sqrt{\frac{\mu}{\epsilon}}} = \frac{\omega \epsilon r_o^2}{d_1} = B_{g1} \quad (6.2.3)$$

where B_{g1} is the susceptance of the input gap when no electron beam is present. Then, from the equivalent circuit, with $Y_s = G_s + jB_s$,

$$A_1 = - \frac{I_{so}}{V_o \sqrt{G_s^2 + (B_{g1} + B_s)^2}} \quad (6.2.4)$$

$$\alpha_1 = - \tan^{-1} \frac{B_{g1} + B_s}{G_s} \quad (6.2.5)$$

At the entrance plane to the second gap, then, the polarization (in the T_1, T_o variables) is

$$Z_1(T_1, T_o) = - \frac{I_{so}}{2V_o \sqrt{G_s^2 + (B_{g1} + B_s)^2}} \cos \left[\sigma T_o - \tan^{-1} \left(\frac{B_{g1} + B_s}{G_s} \right) \right] \sin(T_1) \quad (6.2.6)$$

This may be put in the form of an explicit equation for Z_1 in terms of the Z, T variables using the method developed in Appendix C and previously employed. The result is

$$Z_1(Z, T) = \sum_{n=1}^{\infty} \frac{2}{\sigma n} J_n \left(\frac{\sigma I_{so} \sin Z}{2V_o \sqrt{G_s^2 + (B_{g1} + B_s)^2}} \right) \sin \left[n\sigma T - n\sigma Z - n \tan^{-1} \left(\frac{B_{g1} + B_s}{G_s} \right) - \frac{n\pi}{2} \right] \quad (6.2.7)$$

At the entrance to the second gap, $Z = L_2$.

The relation between the equivalent current and voltage at the second gap is given by

$$I_{e2} = Y_L V_{e2} \quad (6.2.8)$$

At the output gap, $\theta = A_2 \cos(\sigma T + \alpha_2)$, and Equations (4.2.12) and (4.2.13) yield

$$I_{e2} = -B_{gz} V_o A_2 \sin(\sigma T + \alpha_2) \quad , \quad (6.2.9)$$

$$V_{e2} = -2V_o D_2 Z_1(L_2, T) - V_o A_2 \cos(\sigma T + \alpha_2) \quad , \quad (6.2.10)$$

where B_{g2} is the susceptance of the output gap in the absence of the electron beam. In obtaining V_{e2} , the assumptions that D_2 is small and that Z_1 does not change appreciably through the gap were used. Recalling that $Y_L = G_L + jB_L$ is zero except at the fundamental excitation frequency, then using the fundamental term of Z_1 from Equation (6.2.7) in Equations (6.2.8)–(6.2.10) one can determine A_2 and α_2 :

$$A_2 =$$

$$\frac{4D_2}{\sigma} J_1 \left[\frac{\sigma I_{so} \sin Z}{2V_o \sqrt{G_s^2 + (B_{g1} + B_s)^2}} \right] \frac{G_L \cos \left\{ \sigma L_2 + \tan^{-1} \left(\frac{B_{g1} + B_s}{G_s} \right) + B_L \sin \left[\sigma L_2 + \tan^{-1} \left(\frac{B_{g1} + B_s}{G_s} \right) \right] \right\}}{[G_L \cos \alpha_2 - (B_{g2} + B_L) \sin \alpha_2]}$$

(6.2.11)

$$\tan \alpha_2 = \frac{G_L B_{g2} + (G_L^2 + B_L^2 + B_L B_g) \tan \left[\sigma L_2 + \tan^{-1} \left(\frac{B_{g1} + B_s}{G_s} \right) \right]}{G_L B_{g2} \tan \left[\sigma L_2 + \tan^{-1} \left(\frac{B_{g1} + B_s}{G_s} \right) \right] - (G_L^2 + B_L^2 + B_L B_{g2})}$$

(6.2.12)

The power delivered to the load is $I_{e2} V_{e2}$, and the useful power output is the time average of this value. The second term in the voltage expression (6.2.10) is always out of phase with I_{e2} (being related to the capacitance of the gap) and does not contribute to the average power output. The time average power delivered to the load conductance, G_L , relative to the d-c beam power, P_0 , is

$$\begin{aligned} \frac{P_L}{P_0} &= \sigma A_2 \overline{Z_1(L_2, T) \sin(\sigma T + \alpha_2)} \\ &= -A_2 J_1 \left[\frac{\sigma I_{s0} \sin L_2}{2V_0 \sqrt{G_s^2 + (B_{g1} + B_s)^2}} \right] \sin \left[\alpha_2 + \sigma L_2 + \tan^{-1} \left(\frac{B_{g1} + B_s}{G_s} \right) \right] \end{aligned} \quad (6.2.13)$$

This expression gives the output power in terms of the source and load admittances, the gap susceptance, the beam parameters, and the source level. From this, one could investigate the influence of any of these parameters on the output power.

As an example, consider the case when the input and output circuits are adjusted for resonance in the absence of the beam; thus

$$\begin{aligned} B_s + B_{g1} &= 0 \\ B_L + B_{g2} &= 0 \end{aligned} \quad (6.2.14)$$

Recognizing that the restriction to short gaps implies that B_{g1} and B_{g2} are very large, gives, in this case,

$$A_2 = \frac{4D_2}{\sigma} J_1 \left(\frac{\sigma I_{s0} \sin L_2}{2V_0 G_s} \right) \frac{G_L \cos \sigma L_2 + B_L \sin \sigma L_2}{G_L \cos a_2}$$

$$\approx \frac{4D_2}{\sigma} J_1 \left(\frac{\sigma I_{s0} \sin L_2}{2V_0 G_s} \right) \frac{B_L}{G_L} \frac{\sin \sigma L_2}{\cos a_2}$$

$$a_2 = \tan^{-1} \left(\frac{G_L B_{g2} + G_L^2 \tan \sigma L_2}{G_L B_{g2} \tan \sigma L_2 - G_L^2} \right) \approx \tan^{-1} (\cot \sigma L_2) = \frac{\pi}{2} - \sigma L_2 \quad (6.2.15)$$

The power is then

$$\frac{P_L}{P_0} \approx - \frac{4D_2}{\sigma} \frac{B_L}{G_L} J_1^2 \left(\frac{\sigma I_{s0} \sin L_2}{2V_0 G_s} \right) \quad ; \quad (6.2.16)$$

but $B_L = -B_{g2}$ and $Y_{B0} = 2D_2 B_{g2}/\sigma$, then

$$\frac{P_L}{P_0} \approx 2 \frac{Y_{B0}}{G_L} J_1^2 \left(\frac{\sigma I_{s0} \sin L_2}{2V_0 G_s} \right) \quad (6.2.17)$$

The restriction on the source level to keep the beam modulation below the electron overtaking point in the drift region must be observed. This limits the argument of the Bessel function to values less than unity.

This approximate expression for the power output exhibits the expected type of behavior. It reveals the onset of saturation effects as the input drive is increased and indicates the dependence of the output power on the drift length, space charge, and the source and load admittances. This expression should hold well for short gap lengths ($D \ll 1$); longer gap lengths would require a considerably more complex analysis and possible resort to computer techniques. Because of the assumption that the gaps approach

ideal gaps, the computed power gain would be infinite since no power is transferred to an ideal input gap. However, for a short, but nonideal, input gap the input power can be calculated from the discussion of beam loading for short gaps in Section 5.5. For example, using results of that section, the power input to the first gap is (for $B_s + B_{g1} = 0$),

$$\frac{P_{in}}{P_o} = \frac{\sigma(\sigma^2-1)}{6} D_1^3 \frac{I_{so}}{V_o G_s} J_1 \left[\frac{\sigma I_{so}}{2V_o G_s D_1(\sigma^2-1)} \right] J_0 \left[\frac{\sigma I_{so}}{2V_o G_s D_1(\sigma^2-1)} \right] \quad (6.2.18)$$

if $\frac{\sigma I_{so}}{2V_o G_s D_1(\sigma^2-1)} \ll 1$. This, together with the other restriction previously noted on the source level, implies that $D_1(\sigma^2-1) \gg 1$. The gain is then,

$$\frac{P_L}{P_{in}} = \frac{12}{\sigma(\sigma^2-1)} \frac{G_s}{G_L} \frac{I_o}{I_{so}} \frac{J_1^2 \left(\frac{\sigma I_{so} \sin L_2}{2V_o G_s} \right)}{D_1^3 J_1 \left[\frac{\sigma I_{so}}{2V_o G_s D_1(\sigma^2-1)} \right] J_0 \left[\frac{\sigma I_{so}}{2V_o G_s D_1(\sigma^2-1)} \right]} \quad (6.2.19)$$

The many approximations made in deriving this equation should be kept in mind.

There is another point of interest that requires discussion. Equation (6.2.17) indicated that the power output can be increased indefinitely by decreasing the load conductance, G_L . There are limitations, however, which are not apparent in this equation. Equation (6.2.15) for A_2 shows that as G_L is reduced, A_2 increases. However, A_2 must be restricted so that reflection of electrons at the output gap does not occur, let alone

electron crossover in the output gap. Thus as G_L is reduced, the output gap excitation will increase to a level where the theory developed in this section is not valid and other effects will occur to limit the maximum power extracted from the beam.

VII. CONCLUSIONS AND RECOMMENDATIONS

This report considers an electron beam of finite extent, confined by a strong axial magnetic field, which passes alternately through gap and drift regions. In the gap regions the electron beam interacts with an excitation field produced either by an externally applied signal or by an induced current resulting from the beam modulation. In the drift regions, assuming a magnetic wall at the beam boundary has allowed the solutions of interest to be those with no transverse variations. The theory developed here for nonlinear space-charge waves takes account of space-charge effects exactly, therefore consideration has been restricted to beam modulations below the level at which overtaking of the electrons occur. For convenience, throughout the report the gap lengths have been assumed to be short compared to the free-space wavelength.

An exact solution for the case of N gaps and drift regions with arbitrary excitation signals at each gap has been obtained in the T_1, T_0 co-ordinate system. Unfortunately, this co-ordinate system is not convenient for the numerical calculation of the operating characteristics of the model. However, these exact solutions are valuable for the insight they provide into the nonlinearity of the model and as a starting point to find approximate solutions in the Z, T system, which are suitable for numerical computation. It is found that for the case of ideal gaps, and especially for $\sigma = \omega/\omega_p \gg 1$, significant simplifications result in the exact solutions.

Most of the report is directed toward the case of continuous-wave excitation of an input gap with a drift region following it. Although the exact solution is developed in the T_1, T_0 system, the main emphasis is on

obtaining approximate solutions in the Z, T system suitable for computation.

The first-order solution for an ideal input gap with continuous-wave excitation followed by a drift region yields expressions for the polarization and current density in terms of the fundamental frequency and its harmonics. The harmonic amplitudes are obtained as a function of excitation level, position along the drift region, and σ . The compression of the fundamental current-density component with excitation level (compared to a linear theory) is obtained and equals 1.4 db at the electron overtaking point. The harmonic amplitudes are found to increase rapidly with excitation level, and at electron crossover the harmonic amplitudes fall off only as $n^{-1/3}$. Because the first-order solution neglects nonlinearity in the gap, only the nonlinearity in the drift region is accounted for. Therefore, no excitation-dependent phase shift is found nor any d-c term in the polarization.

The second-order solution for the ideal input gap does take account of nonlinearity in the gap, and as a consequence the polarization exhibits an excitation-dependent d-c term. This term, while small, may disrupt the assumed d-c beam behavior, but this possible effect has not been investigated. Also, an excitation-dependent phase delay is found. This term is small, of the order of a few degrees at electron crossover, and increases nearly linearly with excitation power at levels appreciably below electron crossover. Close to the crossover point, the phase delay increases more rapidly with drive power. The physical explanation for the drive-dependent phase delay is that in the ideal input gap some of the original d-c beam energy is converted into a-c kinetic energy and the beam slows down, causing a phase delay. At least for the first few harmonic amplitudes, the values given by the second-order solution are essentially the same as

those given by the first-order solution. This indicates that a first-order solution is adequate to compute harmonic amplitudes for the first few harmonics, but is inadequate to provide phase shift data. Excitation-dependent phase shift is clearly a second-order effect.

Approximate solutions are also obtained for the case of a nonideal input gap. In the course of this development, the dependence of the d-c gap transit angle on the excitation level is seen to be fairly small, at least for excitation levels low enough to preclude electron crossover in the following drift region. To obtain an approximate solution in the drift region, the a-c variation of the gap transit angle is neglected; this is somewhat akin to the first-order solution for the ideal gap. As a result, no excitation-dependent phase delay or d-c term is obtained in the polarization. By analogy with the case of the ideal input gap, however, it is expected that the harmonic amplitudes should be fairly accurate.

For the nonideal input gap, the fundamental current density component leaving the gap is found to depend primarily on the gap length measured in plasma wavelengths; i. e., the longer the gap in plasma wavelengths, the larger the current density. However, the limiting amplitude attained at a quarter plasma wavelength along the drift region depends on the gap length measured in terms of free-space wavelengths. The shorter the gap (in free-space wavelengths) the higher the peak value, and all input gaps with the same length have the same maximum amplitude. Also, the compression of the maximum amplitude of the current density relative to the linear theory is found to decrease for increasing input gap lengths (measured in free-space wavelengths). The harmonic amplitudes depend even more sensitively on the input gap length than does the fundamental. Increasing the gap length

decreases the harmonic amplitudes, at least for the lowest harmonics.

Numerical results for the beam loading of the input gap are obtained only for short input gap lengths. Longer gap lengths probably require computer methods to obtain numerical results. For the range of gap lengths for which computations are made, it is found that the beam loading impedance is virtually insensitive to the excitation level (below the electron overtaking level), although, of course, highly dependent on gap length and σ .

And finally, the approximate solution for the two-gap case is obtained for ideal gaps. The power delivered to the load in the output gap is believed to be reasonably accurate for short gaps. Inasmuch as nonlinearity in the gap regions is neglected, there is no drive-dependent phase shift evident. The results for the power output show the onset of saturation effects at the electron overtaking point where the output power is 1.1 db below the value that a linear theory would predict. This power compression is due to the saturation of the fundamental component of the current density. The theory predicts that the power output may be increased by decreasing the load conductance. This is somewhat illusory, however, since there are limits on the minimum value of the load conductance that can be used in practice. The load conductance must be large enough that electron overtaking does not occur in the output gap, or worse, that electrons are not reflected back into the drift region from the output gap. In either case the theory becomes invalid; therefore, the theory predicts the maximum power output for the smallest load conductance consistent with no electron overtaking and no electron reflection in the output gap.

The theory developed in this report appears to provide a useful approach for investigating some of the nonlinear properties of an idealized

model of a klystron and it is recommended that it be exploited in several directions. First, more attention should be directed toward obtaining tractable approximate solutions in the long-gap cases. Second, the theory for the multiple-gap and drift-region case should be pursued. This might provide valuable insight into the operation of multicavity klystrons. And third, excitation signals with more complex frequency spectra should be investigated. In particular, the application of two continuous-wave signals at different frequencies would allow investigation of the effect of electron beam capture. And the application of short pulses of RF would enable an investigation of the limiting pulse capabilities of klystrons to be investigated.

APPENDIX A: GLOSSARY

A	Amplitude of excitation signal in first gap
A_n	Amplitude of excitation signal in n^{th} gap
A_z	Vector potential
a_n	Fourier coefficient
B_g	Gap susceptance with no beam present
B_L	Load susceptance
B_s	Driving-source susceptance
b_n	Fourier coefficient
C_1, C_2, c	Constants
$c = \frac{1}{\sqrt{\mu\epsilon}}$	Velocity of light
$D = \beta_p d, D_n = \beta_p d_n$	Normalized gap lengths
d	First gap length
d_n	n^{th} gap length
$E(z, t)$	Total electric field
E_a	Electric field in gap produced by excitation only
e	Absolute magnitude of electronic charge
G_L	Load conductance
G_s	Driving-source conductance
$H(r, z, t)$	Magnetic field
$H_n(T_1) = 1$	where $\lambda_n < T_1 < \lambda_n + \Gamma_n$
$\quad = 0$	where $T_1 < \lambda_n$ or $T_1 > \Gamma_n + \lambda_n$
I_e	Equivalent gap current
I_o	D-c beam current

I_s	Driving-source current
$J(z, t)$	Change in beam current density resulting from excitation
$-J_o$	Original d-c beam-current density
$J_T = -J_o + J(z, t)$	Total beam-current density
$J_n(x)$	Bessel function of first kind and order n
L	Normalized length of first drift region
L_n	Normalized distance from origin to location of the entrance plane of the n^{th} gap
M	Constant
m	Electron mass, or integer
N	Constant
n	Integer
P	Constant
$P_o = I_o V_o$	D-c beam power
P_r	Electromagnetic power in radial direction
$Q(Z) = \sqrt{\cos^2 Z + \sigma^2 \sin^2 Z}$	
$R = \beta_p r$	
R_{BL}	Beam-loading resistance
$R_o = \beta_p r_o$	
r	Radial co-ordinate
r_o	Radius of beam edge
s	Laplace transform variable
$T = \omega_p t$	Normalized time
$T_o = \omega_p t_o$	
$T_1 = \omega_p t_1 = T - T_o$	

t	Time
t_0	Time that a particular electron passes $z = 0$
$t_1 = t - t_0$	
$u(z, t)$	Change in electron velocity due to excitation
u_0	Original d-c beam velocity
$u_T = u_0 + u(z, t)$	Total beam velocity
V_e	Equivalent gap voltage
V_0	D-c beam voltage
V_s	Driving-source voltage
X_{BL}	Beam-loading reactance
x	Variable
Y_{BL}	Beam-loading admittance
$Y_{Bo} = I_0/V_0$	D-c beam admittance
Y_L	Load admittance
Y_s	Driving-source admittance
y	Variable
$Z = \beta_p z$	Normalized position
$Z_0 = \beta_p z_0 = T_1$	
$Z_1 = \beta_p z_1 = Z - Z_0$	
Z_{BL}	Beam-loading impedance
$Z_{Bo} = V_0/I_0$	D-c beam impedance
Z_L	Load impedance
Z_s	Driving-source impedance
z	Longitudinal position with excitation
z_0	Longitudinal position in absence of excitation

$z_1 = z - z_0$	
$Z(s_1, T_0)$	Laplace transform of $Z_1(T_1, T_0)$
$\beta_p = \omega_p / u_0$	Plasma phase constant
$\eta = u_0 / c = u_0 \sqrt{\mu\epsilon}$	
Γ	Value of T_1 at $Z = D$
λ_n	Value of T_1 at $Z = L_n$
$\lambda_n + \Gamma_n$	Value of T_1 at $Z = L_n + D_n$
θ	Azimuthal direction
$\theta(t) = \frac{E_a(t)}{V_0/d}$	Normalized excitation
$\Theta(s, T_0)$	Laplace transform of $\theta(T_1 + T_0)$
ν	Angle
$\rho(z, t)$	Change in charge density resulting from excitation
$-\rho_0$	Original d-c charge density
$\rho_T = -\rho_0 + \rho(z, t)$	Total charge density
$\sigma = \omega / \omega_p$	
τ	Integration variable
ϕ	Scalar potential
ω	2π excitation frequency
$\omega_p = \sqrt{\frac{e\rho_0}{m\epsilon}}$	Plasma frequency

APPENDIX B: STRUCTURE TO PROVIDE MAGNETIC WALL

Consider the finned structure shown in Figure B-1. The fin spacing, h , is assumed to be small compared to the wavelength of any wave considered.

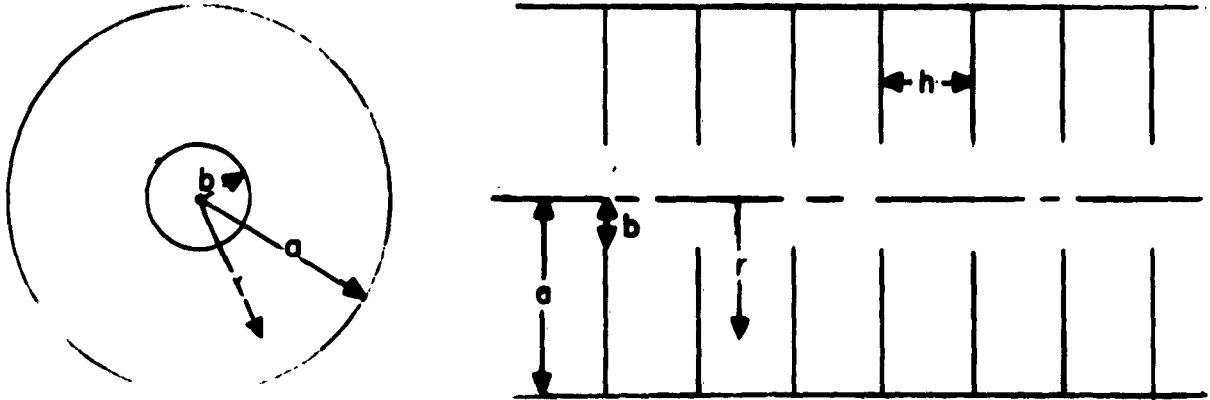


Figure B-1. Finned Structure to Provide a Magnetic Wall at $r = b$

Solutions will be sought in the region $b < r < a$, which have only radial (r) variation and no angular (θ) or longitudinal (z) variation. Since only the transverse-magnetic fields are of interest, $H_z = H_r = E_\theta = 0$. In addition, $E_r = 0$, since longitudinal variations are excluded. This leaves only E_z and H_θ as possible fields. Maxwell's equations yield

$$\frac{\partial E_z}{\partial r} = j\omega\mu H_\theta \quad ,$$

$$\frac{1}{r} \frac{\partial}{\partial r} (r H_\theta) = j\omega\epsilon E_z \quad . \quad (B. 1)$$

$$\frac{1}{r} \frac{\partial}{\partial r} \left(r \frac{\partial E_z}{\partial r} \right) + k^2 E_z = 0 \quad ,$$

$$k = \omega \sqrt{\mu \epsilon} \quad . \quad (B. 2)$$

The boundary condition is that $E_z = 0$ at $r = a$. The solution which satisfies the differential equation and boundary condition is

$$E_z = C \left[J_0(kr) - \frac{J_0(ka)}{N_0(ka)} N_0(kr) \right] \quad , \quad (B. 3)$$

$$H_\theta = -\frac{kC}{j\omega\mu} \left[J_1(kr) - \frac{J_1(ka)}{N_1(ka)} N_1(kr) \right] \quad , \quad (B. 4)$$

where $J_0(kr)$ and $N_0(kr)$ are Bessel functions of the first and second kind, and C is an arbitrary constant.

The question of the possible existence of a magnetic wall at $r = b$ is the prime motivation for considering this structure. At a magnetic wall, $H_\theta = 0$. This requires that

$$\frac{J_1(kb)}{N_1(kb)} = \frac{J_1(ka)}{N_1(ka)} \quad . \quad (B. 5)$$

There are an infinite number of values of kb which satisfy this equation for each ratio of b/a . The first six solutions (taken from the data in Jahnke and Emde,¹⁷ (pages 207-209), are shown in Figure B-2, where b/a is plotted versus kb . Thus for a particular b/a , there are an infinite number of frequencies at which the surface $r = b$ appears to be a magnetic wall. These frequencies are not harmonically related, although they do increase nearly as $n - 1/2$ for $n \geq 2$.

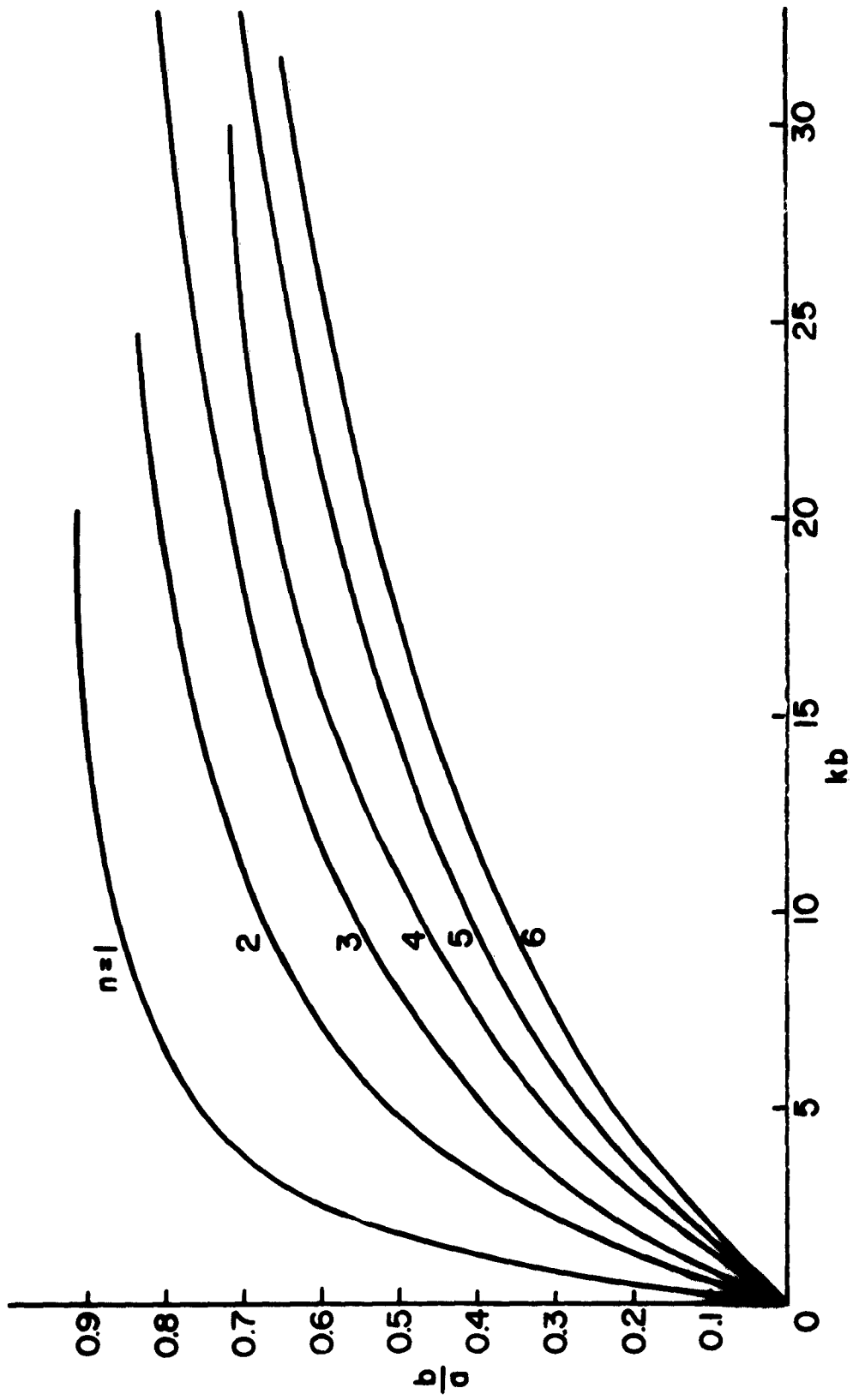


Figure B-2. First Six Solutions of $\frac{J_1(kb)}{N_1(kb)} = \frac{J_0(ka)}{N_0(ka)}$.

The reason for the close-spaced thin fins is as follows. The fields in the regions between the fins are taken to be independent of z . Since there is no coupling between regions for $b < r < a$, the phase between neighboring regions is arbitrary and determined by the fields inside the $r = b$ radius. Thus if h is small compared to the longitudinal wavelength of the fields for $r < b$, then the structure can provide an effective magnetic wall at $r = b$ regardless of the longitudinal variation of the fields.

APPENDIX C: INVERSION OF CERTAIN TRIGONOMETRIC RELATIONS

C.1 General Development

In the nonlinear theory of klystrons discussed in this report, relations of the form,

$$y = x + f(y) \quad , \quad (C. 1. 1)$$

have frequently arisen where $f(y)$ is a periodic function of y with period 2π , and it is desired to find y explicitly in terms of x . This appendix indicates how one might find a formal solution for a broad class of functions, $f(y)$, but since the solution cannot be expressed in a concise form, this development will not be explored in detail. Rather the solutions for the few special cases of interest for this study will be presented explicitly.

The development to be sketched here is a straightforward extension of the method used to solve Kepler's problem in celestial mechanics by Lagrange (see, for example, Watson¹⁸). In that problem, $f(y) = C \sin y$. Sackinger¹⁹ has applied the results for this case to the nonlinear ballistic theory of a klystron.

It is clear that since $f(y)$ is periodic in y with period 2π , that $y - x$ is also. Considering x as a function of y , then gives

$$y + 2\pi - x(y + 2\pi n) = f(y + 2\pi n) = f(y) = y - x(y) \quad , \quad (C. 1. 2)$$

$$x(y + 2\pi n) = x(y) + 2\pi n \quad . \quad (C. 1. 3)$$

Thus, whenever y changes by $2\pi n$, x must also change by $2\pi n$. The consequence of this is that $f(y)$ when considered as a function of x must

be periodic in x with period 2π . If $f(y)$ is single valued in x and satisfies the usual conditions, then $y - x = f(y)$ can be expanded in a Fourier series in x :

$$y - x = \sum_{n=0}^{\infty} (a_n \cos nx + b_n \sin nx) \quad . \quad (C. 1. 4)$$

Figure C-1 shows a typical example of $y - x$ considered as a function of y and of x .

The Fourier coefficients in Equation (C. 1. 4) may be evaluated in the following manner. Let λ equal the value of x when y is equal to π :

$$\begin{aligned} a_0 &= \frac{1}{2\pi} \int_{\lambda-2\pi}^{\lambda} (y-x) dx = \frac{1}{2\pi} \left[\int_{\lambda-2\pi}^{\lambda} y dx - \left(\frac{x^2}{2}\right)_{\lambda-2\pi}^{\lambda} \right] , \\ &= \frac{1}{2\pi} \left[(yx)_{x=\lambda-2\pi}^{x=\lambda} - \int_{y=-\pi}^{y=\pi} x dy - 2\pi(\lambda - \pi) \right] , \\ &= -\frac{1}{2\pi} \int_{y=-\pi}^{y=\pi} x dy = -\frac{1}{2\pi} \int_{-\pi}^{\pi} [y - f(y)] dy , \\ &= \frac{1}{2\pi} \int_{-\pi}^{\pi} f(y) dy \quad . \quad (C. 1. 5) \end{aligned}$$

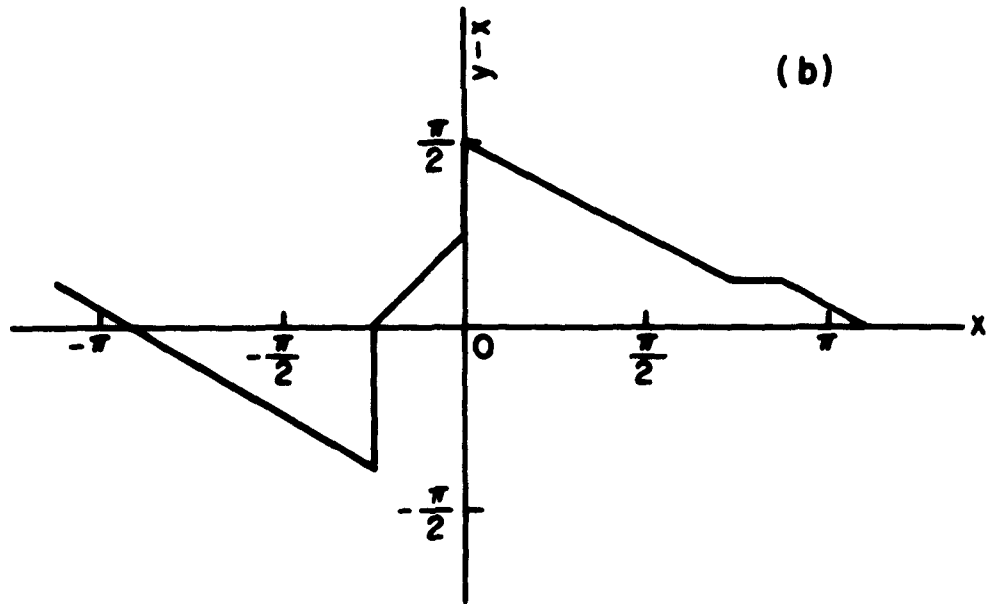
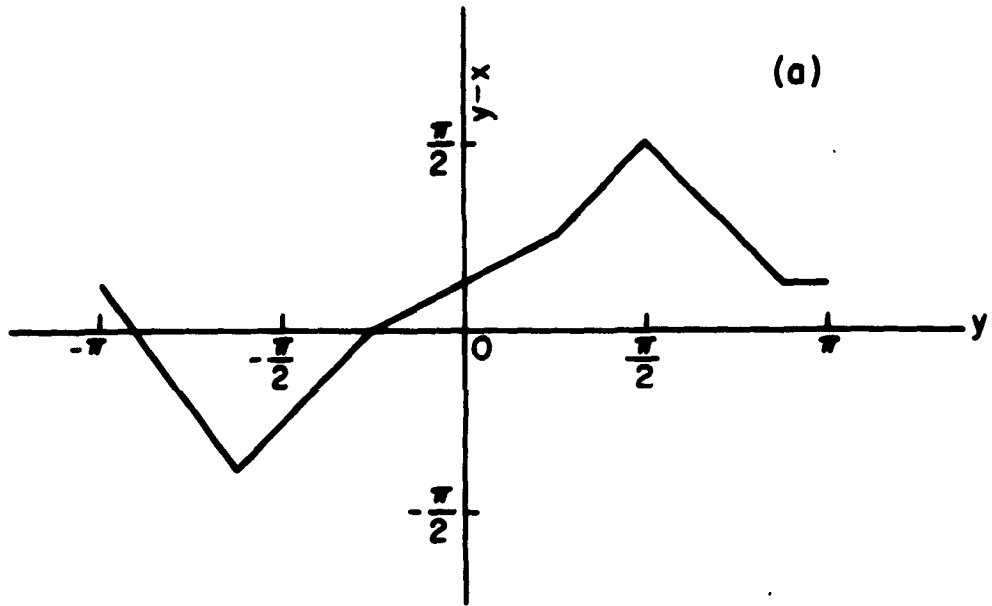


Figure C-1. $y-x$ as a Function of (a) x , and (b) y .

Thus a_0 is the average value of $f(y)$ in the interval $-\pi$ to π .

$$\begin{aligned}
 a_n &= \frac{1}{\pi} \int_{\lambda-2\pi}^{\lambda} (y-x) \cos nx \, dx = \frac{1}{\pi} \left(\int_{\lambda-2\pi}^{\lambda} y \cos nx \, dx - \int_{\lambda-2\pi}^{\lambda} x \cos nx \, dx \right) \\
 &= \frac{1}{\pi} \left[\left(\frac{y \sin nx}{n} \right)_{x=\lambda-2\pi}^{x=\lambda} - \frac{1}{n} \int_{y=-\pi}^{y=\pi} \sin nx \, dy - \frac{1}{n^2} \left(\cos nx + nx \sin nx \right)_{x=\lambda-2\pi}^{x=\lambda} \right] \\
 &= -\frac{1}{n\pi} \int_{-\pi}^{\pi} \sin nx \, dy = -\frac{1}{n\pi} \int_{-\pi}^{\pi} \sin [ny - nf(y)] \, dy \quad (C. 1.6)
 \end{aligned}$$

$$\begin{aligned}
 b_n &= \frac{1}{\pi} \int_{\lambda-2\pi}^{\lambda} (y-x) \sin nx \, dx = \frac{1}{\pi} \left(\int_{\lambda-2\pi}^{\lambda} y \sin nx \, dx - \int_{\lambda-2\pi}^{\lambda} x \sin nx \, dx \right) \\
 &= \frac{1}{\pi} \left[-\left(\frac{y \cos nx}{n} \right)_{x=\lambda-2\pi}^{x=\lambda} + \frac{1}{n} \int_{y=-\pi}^{y=\pi} \cos nx \, dy - \frac{1}{n^2} \left(\sin nx - nx \cos nx \right)_{x=\lambda-2\pi}^{x=\lambda} \right] \\
 &= \frac{1}{n\pi} \int_{-\pi}^{\pi} \cos nx \, dy = \frac{1}{n\pi} \int_{-\pi}^{\pi} \cos [ny - nf(y)] \, dy \quad (C. 1.7)
 \end{aligned}$$

At this point one could continue the general solution by inserting a Fourier series in y for $f(y)$ and expanding the integrands in products of

series of Bessel functions. However, attention is restricted here to a few special cases, which are of immediate interest.

Before these are examined, the range of convergence of the Fourier series in x will be investigated. The usual restrictions on $y - x$ as a function of x obtain; e. g., that it be of bounded variation and that $\int_{-\pi}^{\pi} f(y) dx$ exist. In addition, it must be a single-valued function of x . This fixes the range of convergence. Consideration of $y - x$ shows that it will be a single-valued function of x for $\frac{df(y)}{dy} < 1$ and multiple valued for $\frac{df(y)}{dy} > 1$.

C.2 Case of $f(y) = C \sin y$

The Fourier coefficients are,

$$a_0 = 0 \quad , \quad (C. 2. 1)$$

$$a_n = -\frac{1}{n\pi} \int_{-\pi}^{\pi} \sin(ny - nc \sin y) dy = 0 \quad , \quad (C. 2. 2)$$

$$b_n = \frac{1}{n\pi} \int_{-\pi}^{\pi} \cos(ny - nc \sin y) dy = \frac{2}{n} J_n(nc) \quad . \quad (C. 2. 3)$$

C.3 Case of $f(y) = C \cos y$

$$a_0 = 0 \quad , \quad (C. 3. 1)$$

$$a_n = \frac{1}{n\pi} \int_{-\pi}^{\pi} \sin(ny - nc \cos y) dy = \frac{2}{n} \sin\left(\frac{n\pi}{2}\right) J_n(nc) \quad , \quad (C. 3. 2)$$

$$b_n = \frac{1}{n\pi} \int_{-\pi}^{\pi} \cos(ny - nc \cos y) dy = \frac{2}{n} \cos\left(\frac{n\pi}{2}\right) J_n(nc) \quad (C. 3. 3)$$

C. 4 Case of $f(y) = C_1 \cos y + C_2 \cos 2y$

$$a_0 = 0 \quad (C. 4. 1)$$

$$a_n = -\frac{1}{n\pi} \int_{-\pi}^{\pi} \sin(ny - nC_1 \cos y - nC_2 \cos 2y) dy \quad (C. 4. 2)$$

$$b_n = \frac{1}{n\pi} \int_{-\pi}^{\pi} \cos(ny - nC_1 \cos y - nC_2 \cos 2y) dy \quad (C. 4. 3)$$

These integrals may be evaluated by using expansions of the type,

$$e^{jC \cos y} = \sum_{m=-\infty}^{+\infty} (j)^m J_m(C) e^{jm y} \quad (C. 4. 4)$$

The results are, for n odd,

$$\begin{aligned} a_n = \frac{2}{n} & \left(\sum_{m=\frac{n+1}{2}}^n \sin\left(\frac{m\pi}{2}\right) \epsilon_{n-m} J_{2m-n}(nC_1) J_{n-m}(nC_2) \right. \\ & + \sum_{m=0}^{\infty} \left\{ \sin\left[\left(\frac{n+3}{2} + 3m\right) \frac{\pi}{2}\right] J_{2m+1}(nC_1) J_{\frac{n+1}{2}+m}(nC_2) \right. \\ & \left. \left. + \sin\left[(n+3m) \frac{\pi}{2}\right] \epsilon_m J_{n+2m}(nC_1) J_m(nC_2) \right\} \right) \quad (C. 4. 5) \end{aligned}$$

$$\begin{aligned}
b_n = \frac{2}{n} & \left(\sum_{m=\frac{n+1}{2}}^n \cos\left(\frac{m\pi}{2}\right) \epsilon_{n-m} J_{2m-n}(nC_1) J_{n-m}(nC_2) \right. \\
& + \sum_{m=0}^{\infty} \left\{ \cos\left[\left(\frac{n+3}{2} + 3m\right) \frac{\pi}{2}\right] J_{2m+1}(nC_1) J_{\frac{n+1}{2}+m}(nC_2) \right. \\
& \left. \left. + \cos\left[(n+3m) \frac{\pi}{2}\right] \epsilon_m J_{n+3m}(nC_1) J_m(nC_2) \right\} \right) , \tag{C.4.6}
\end{aligned}$$

and for n even,

$$\begin{aligned}
a_n = \frac{2}{n} & \left(\sum_{m=\frac{n}{2}}^n \sin\left(\frac{m\pi}{2}\right) \epsilon_{2m-n} \epsilon_{n-m} J_{2m-n}(nC_1) J_{n-m}(nC_2) \right. \\
& + \sum_{m=0}^{\infty} \left\{ \sin\left[\left(\frac{n}{2} + 3m\right) \frac{\pi}{2}\right] \epsilon_{2m} J_{2m}(nC_1) J_{\frac{n}{2}+m}(nC_2) \right. \\
& \left. \left. + \sin\left[(n+3m) \frac{\pi}{2}\right] \epsilon_m J_{n+2m}(nC_1) J_m(nC_2) \right\} \right) , \tag{C.4.7}
\end{aligned}$$

$$\begin{aligned}
b_n = \frac{2}{n} & \left(\sum_{m=\frac{n}{2}}^n \cos\left(\frac{m\pi}{2}\right) \epsilon_{2m-n} \epsilon_{n-m} J_{2m-n}(nC_1) J_{n-m}(nC_2) \right. \\
& + \sum_{m=0}^{\infty} \left\{ \cos\left[\left(\frac{n}{2} + 3m\right) \frac{\pi}{2}\right] \epsilon_{2m} J_{2m}(nC_1) J_{\frac{n}{2}+m}(nC_2) \right. \\
& \left. \left. + \cos\left[(n+3m) \frac{\pi}{2}\right] \epsilon_m J_{n+2m}(nC_1) J_m(nC_2) \right\} \right) . \tag{C.4.8}
\end{aligned}$$

In these expressions,

$$\begin{aligned} \epsilon_m &= \frac{1}{2} \quad , \quad m = 0 \quad , \\ \epsilon_m &= 1 \quad , \quad m \geq 1 \quad , \end{aligned} \quad (C. 4. 9)$$

C. 5 Case of $f(y) = C_1 \cos y + C_2 \sin y$

This can be transformed into a form similar to that of Section C. 3:

$$f(y) = \sqrt{C_1^2 + C_2^2} \cos\left(y - \tan^{-1} \frac{C_2}{C_1}\right) \quad . \quad (C. 5. 1)$$

It is clear that this may be expanded in a Fourier series in $x - \tan^{-1}\left(\frac{C_2}{C_1}\right)$;

$$\begin{aligned} y - x &= y - \tan^{-1} \frac{C_2}{C_1} - \left(x - \tan^{-1} \frac{C_2}{C_1}\right) \\ &= \sum_{n=0}^{\infty} \left[a_n \cos\left(nx - n \tan^{-1} \frac{C_2}{C_1}\right) + b_n \sin\left(nx - n \tan^{-1} \frac{C_2}{C_1}\right) \right] \end{aligned} \quad (C. 5. 2)$$

From Section C. 3 the Fourier coefficients are

$$a_0 = 0 \quad , \quad (C. 5. 3)$$

$$a_n = \frac{2}{n} \sin\left(\frac{n\pi}{2}\right) J_n\left(n\sqrt{C_1^2 + C_2^2}\right) \quad , \quad (C. 5. 4)$$

$$b_n = \frac{2}{n} \cos\left(\frac{n\pi}{2}\right) J_n\left(n\sqrt{C_1^2 + C_2^2}\right) \quad . \quad (C. 5. 5)$$

REFERENCES

1. A. H. W. Beck, Thermionic Valves, Cambridge: Cambridge University Press, 1953.
2. R. Warnecke and P. Guénard, Les Tubes Électroniques à Commande Par Modulation de Vitesse, Paris: Gauthier-Villars, 1951.
3. W. J. Kleen, Electronics of Microwave Tubes, New York: Academic Press, 1958.
4. W. M. Sackinger, "Large-Signal Klystron Gap Theory," Res. Rep. EE 483, Cornell University, 1960.
5. F. Paschke, "On the Nonlinear Behavior of Electron-Beam Devices," RCA Rev., 18 (1951), 221.
6. F. Paschke, "Generation of Second Harmonic in a Velocity-Modulated Electron Beam of Finite Diameter," RCA Rev., 19 (1958), 617.
7. F. Paschke, "Nonlinear Theory of a Velocity-Modulated Electron Beam with Finite Diameter," RCA Rev., 21 (1960), 53.
8. F. Paschke, "New Results on Frequency Multiplication and Nonlinear Phase Distortion in Klystrons and Traveling Wave Tubes," RCA Rev., 22 (1961), 162
9. J. E. Romaine, "Harmonic Analysis of Klystron Beams," Res. Rep. EE 426, Cornell University, 1959.
10. W. E. Blair, "Harmonic Analysis of Electron Beams in Klystrons," Res. Rep. EE 458, Cornell University, 1960.

11. L. Solyman, "Exact Solution of the One-Dimensional Bunching Problem," Jour. Electronics and Control, 10 (1964), 165.
12. S. E. Webber, "Ballistic Analyses of a Two-Cavity Finite Beam Klystron," I.R.E. Trans., ED-5 (1958), 981.
13. C. C. Wang, "Large-Signal Linear-Beam Tube Theory," Proc. I.E.E., 105 B, Supplement No. 11 (1958), 624.